Fine-scale observations and modeling of friction at the base of glaciers

Juan Pedro Roldan Blasco

THÈSE

Pour obtenir le grade de

DOCTEUR DE L'UNIVERSITÉ GRENOBLE ALPES

École doctorale : I-MEP2 - Ingénierie - Matériaux, Mécanique, Environnement, Energétique, Procédés, Production
Spécialité : 2MGE : Matériaux, Mécanique, Génie civil, Electrochimie
Unité de recherche : Institut des Géosciences de lEnvironnement

Observations et modélisation aux fines échelles du frottement à la base des glaciers

Fine-scale observations and modeling of friction at the base of glaciers

Présentée par :

Juan ROLDAN BLASCO

Direction de thèse :

Olivier GAGLIARDINI Professeur des Universités, Université Grenoble Alpes	Directeur de thèse
Christian VINCENT Ingénieur de Recherche, Université Grenoble Alpes	Co-encadrant de thèse
Florent GIMBERT chercheur, CNRS	Co-encadrant de thèse

Rapporteurs :

Ian HEWITT
PROFESSEUR ASSOCIE, University of Oxford
Peter NIENOW
PROFESSEUR, University of Edinburgh

Thèse soutenue publiquement le , devant le jury composé de :

Olivier GAGLIARDINI PROFESSEUR DES UNIVERSITES, Université Grenoble Alpes	Directeur de thèse
Ian HEWITT PROFESSEUR ASSOCIE, University of Oxford	Rapporteur
Peter NIENOW PROFESSEUR, University of Edinburgh	Rapporteur
Anne MANGENEY PROFESSEUR DES UNIVERSITES, Université Paris Diderot, IPG	Examinatrice
David AMITRANO PROFESSEUR DES UNIVERSITES, Université Grenoble Alpes	Président
Christian VINCENT INGENIEUR DE RECHERCHE, CNRS	Co-directeur de thèse

Invités :

Florent Gimbert
CHARGE DE RECHERCHE, CNRS
Adrien Gilbert
CHARGE DE RECHERCHE, CNRS

Some dedication

Abstract

Glacier flow over rough hard beds is controlled by basal processes, such as friction, the opening of cavities behind obstacles and any interaction between the glacier bed and basal ice. In this PhD, we study a multitude of these processes. Current theories to describe drag of glaciers over hard beds are formulated on the basis that ice is free of debris and slides without friction over the glacier bed. However, debris at the basal layers and cold ice cause additional resistance to glacier flow. We provide an analytical model of glacier sliding that accounts for the effect of local shear stress at the ice-bed interface in the framework of Weertman (1957), and expand the solution to account for the opening of cavities. This additional drag slows glacier sliding but due to additional strain enhancement of the basal ice, the viscosity of the ice decreases and the basal speed is higher than expected. The inclusion of local shear stress makes the friction law implicit, complicating the identification of scaling parameters from the geometry alone. We further study this problem using a numerical finite element model of glacier sliding over a sinusoidal bed under steady-state conditions. We find that the law with non-zero local shear stress at the base retains the overall form of the friction law with zero local shear stress, such that an appropriate scaling can be obtained. The similarity between a friction law with zero and non-zero local shear stress is convenient for generalising empirical friction laws at the field scale, although it complicates the identification of the effect of local shear stress on glacier flow. Glacier internal deformation is controlled by the ice rheology which is described by the Glen's law through two material parameters, the creep factor A and the flow law exponent n. There is great uncertainty in the values of these parameters as a result of scarce observations at the natural scale. One of the techniques that has been used to study ice deformation and constrain material properties is borehole inclinometry. We present here the results of an inclinometry study carried out at the ablation zone of Glacier d'Argentière, a temperate glacier in the French Alps. We monitored glacier deformation during 2020 with borehole-installed tiltmeters that record tilt change every 30 minutes. We are able to reconstruct the deformation rates profile with depth and the deformation velocity. Complementing our dataset with a dense network of GPS stations we are able to indirectly observe the basal velocity during the studied period. We infer the rheological parameters by comparing our observations with the deformation rates retrieved with a three-dimensional model solving the Stokes equation. We demonstrate that the yearly-averaged deformation rates profile has limited sensitivity to the flow law exponent n and instead mainly reflects an increase in the creep factor A with depth which could be explained with depth-increasing interstitial water content. The depth-averaged creep factor is found to be 1.5 times higher than the recommended one for temperate ice. We further show that internal ice deformation exhibits seasonal variability, such that surface velocity changes cannot be attributed solely to changes in basal conditions. At longer timescales, surface velocity variability is better explained with changes in the deformation rates, while shorter velocity variability (weeks or days) is better explained with changes in basal velocity. Further work remains to be conducted in order to confirm if the observed creep enhancement is due to depth-increasing water content, and to determine the causes behind the seasonal changes in internal deformation and basal velocity. Our results will help future assessment of the state and evolution of the cryosphere.

Mots clés: Glacier flow, fluid dynamics, observations

Résumé

L'écoulement des glaciers sur des lits durs et rugueux est contrôlé par des processus basaux, tels que la friction, l'ouverture de cavités derrière des obstacles et toute interaction entre le lit du glacier et la glace basale. Dans cette thèse, nous étudions une multitude de ces processus. Les théories actuelles pour décrire la traînée des glaciers sur des lits durs sont formulées sur la base que la glace est exempte de débris et glisse sans friction sur le lit du glacier. Cependant, les débris dans les couches basales et la glace froide causent une résistance supplémentaire à l'écoulement. Nous fournissons un modèle analytique du glissement des glaciers qui tient compte de l'effet de la contrainte de cisaillement locale à l'interface glace-lit dans le cadre de Weertman (1957), et étendons la solution pour tenir compte de l'ouverture des cavités. Cette traînée supplémentaire ralentit le glissement du glacier, mais en raison de l'augmentation de la déformation de la glace basale, la viscosité diminue et la vitesse basale est plus élevée que prévu. L'inclusion de la contrainte de cisaillement locale rend la loi de friction implicite, ce qui complique l'identification des paramètres d'échelle à partir de la géométrie seule. Nous constatons que la loi avec une contrainte de cisaillement locale non nulle à la base conserve la forme générale de la loi de friction avec une contrainte de cisaillement locale nulle, de sorte qu'une mise à l'échelle appropriée peut être obtenue. La similitude entre une loi de friction avec une contrainte de cisaillement locale nulle et non nulle est pratique pour généraliser les lois de friction empiriques à l'échelle du champ, bien qu'elle complique l'identification de l'effet de la contrainte de cisaillement locale sur l'écoulement des glaciers. La déformation interne des glaciers est contrôlée par la rhéologie de la glace qui est décrite par la loi de Glen à travers deux paramètres matériels, le facteur de fluage A et l'exposant n de la loi d'écoulement. Il existe une grande incertitude quant aux valeurs de ces paramètres en raison de la rareté des observations à l'échelle naturelle. Nous présentons ici les résultats d'une étude d'inclinométrie réalisée dans Glacier d'Argentière, un glacier tempéré des Alpes françaises. Nous avons suivi la déformation du glacier au cours du 2020 grâce à des inclinomètres installés dans des forages qui enregistrent les changements d'inclinaison toutes les 30 minutes. Nous pouvons reconstruire le profil des taux de déformation avec la profondeur et la vitesse de déformation. Nous complétons notre ensemble de données par un réseau de stations GPS qui permet d'observer la vitesse basale pendant la période étudiée. Nous déduisons les paramètres rhéologiques en comparant nos observations avec les taux de déformation obtenus à l'aide d'un modèle tridimensionnel résolvant l'équation de Stokes. Le profil des taux de déformation en moyenne annuelle a une sensibilité limitée à l'exposant n de la loi d'écoulement et reflète principalement une augmentation de A avec la profondeur qui pourrait être expliquée par une augmentation de la teneur en eau interstitielle en profondeur. Nous montrons également que la déformation interne de la glace présente une variabilité saisonnière, de sorte que les changements de vitesse de surface ne peuvent être attribués uniquement aux changements des conditions basales. Sur des échelles de temps plus longues, la variabilité de la vitesse de surface est mieux expliquée par les changements dans les taux de déformation, tandis que la variabilité de la vitesse plus courte est mieux expliquée par les changements à la base. D'autres travaux restent à mener pour confirmer si l'augmentation du fluage observée est due à l'augmentation de la teneur en eau, et déterminer les causes des changements saisonniers de la déformation et de la vitesse basale. Nos résultats contribueront à l'évaluation future de l'état et de l'évolution de la cryosphère.

Mots clés: Écoulement des glaciers, dynamique des fluids, observations

Acknowledgements

Thanks to all my supervisors, without whom this would have never been possible.

Preface

Θάλλατα! Θάλλατα!
Xenophon, *Anabasis*, IV, 7.

Contents

Chapter 1

Context

Projections of more than 1 m of sea level rise are good for funding research.
Paraphrasing a well known glaciologist.

1.1 What are glaciers, and why do we care about them?

From the high peaks of mountains and other cold areas of the Earth, glaciers flow towards valleys and the oceans like frozen rivers, shaping the future and serving as witness of the past. At the highest part of a glacier, in the so called ablation zone, snowfall survives summer and slowly compresses into ice. Ice, which at ready can be considered a solid, deforms under the great pressures caused by the tens, hundreds or even thousands of meters of ice that form up the different glaciers, ice caps and ice shelves of the Earth, and thus the glaciers flow. As a result, ice is transported downwards, entering the ablation zone, i.e. the part of the glacier where mass loss due to melting and other processes is higher than snowfall accumulation, until ablation is so high that ice disappears and the glacier ends. If ice did not deform, ice would not be found on the accumulation zone and glaciers would just be still mountains of ice, not rivers of ice.

In their downward flow, glaciers erode mountains and shape them (see Figure 1.1), becoming part of the landscape. Likewise, they are also incised in the collective memory of those who live close to them, ranging from traditional communities who consider glaciers religious entities (Allison, 2015), to the inhabitants of the European Alps who have witnessed the progressive retreat of glaciers in the last century (Lob). By storing the past in their ice layers, glaciers have been used as witnesses of the past and studied to answer a wide variety of questions, ranging from the state of the climate in the last millenia **some paper, there must be hundreds out there**, the production of lead in Ancient Europe (McConnell et al., 2018; Preunkert et al., 2019), or even the location of accidents happening at the surface of glaciers (Jouvet and Funk, 2014; Compagno et al., 2019). While they flow, glaciers also play an important environmental role. They provide important natural resources, as they release sediments and meltwater, transporting nutrients, and feeding rivers, lakes and aquifers throughout summer, supporting agricultural activities. Other economical activities actively exploit glaciers, such as the hydroelectrical stations that generate power from subglacial runoff, or the different touristic businesses dedicated to skiing, hiking on glaciers, and other types of glacier-related activities. Last, but not least, glaciers are complex geophysical systems, and inspire researchers in their quest for answers and understanding of reality.

Unfortunately, climate change has given motives to be increasingly concerned about glaciers in the coming decades. A direct implication of warming is the imbalance of glacier mass, who have been, for the most part, retreating almost continuously since at least the 1950's (WGMS, 2022). We provide and example of mass loss of alpine glaciers in Figure **??**. The prospective future of mountain glaciers are particularly grim, and now glacier farewell parties have now become a relatively common event in some countries, i.e. Luckhurst (2019); Jaquet and l'afp (2019); Bouhassira (2020), as the glaciers seen by generations of still-living mountain dwellers are confined to photographs.

A comment on glacier names: Glacier names are usually written in the native language of the country where they are, and typically mean 'Something glacier', or 'The glacier by some town'. For instance, we have Engabreen (Norway), which could be directly translated as Glacier of the meadow, Glacier d'Argentière (France), which is sometimes written Argentière Glacier (in its english form), and means the glacier by (the town of) Argentière, Aletschgletscher (Switzerland) which literally means Aletsch Glacier, and is sometimes called so in the literature, and Hofsjökull (Iceland), "temple glacier" in icelandic, is sometimes referred as 'Hofsjökull Ice Cap' (therefore, the temple glacier ice cap). Choosing one option for the other has advantages and disadvantages, and while it could be understood that we refer to La Mer de Glace (France), meaning 'the sea of ice', by the 'Mer de Glace Glacier', it would make no sense to refer to Glacier d'Argentière as 'Glacier d'Argentière Glacier'. In this PhD we will avoid any type of confusion by always respecting, and referring to, the original name (Engabreen, Glacier d'Argentière, etc). This is a PhD on glaciers, after all, and context is strong enough to suggest that Storglaciarën (Sweden) is anything but a swedish glacier (and a fast flowing one, on a completely unrelated note).

The rapid warming and retreat of mountain glaciers put all those that depend on glaciers in jeopardy. For example, the patterns of water availability will be disrupted, increasing the severity of droughts and affecting agricultural yields (Oppenheimer and Sebesvari, 2019). Similarly, while glacier-related catastrophes are found in history (e.g. Vincent et al., 2010), climate change has paved the way for more recent glacier collapses (Kääb et al., 2018), and is expected to increase the likelihood of glacier-related catastrophes in the future (Oppenheimer and Sebesvari, 2019). On a global level, glacier mass loss is, and will continue to be, the main contributor to the increase in sea level (WGMS, 2022). Since the 1960's, the sea has being rising at increasing rates, due to a combined action of increase water volume due to heat expansion, valley glacier mass loss, and ice sheet mass loss (Greenland and Antarctica), with an estimated rise by 2050 between 0.24 m and 0.32 m, affecting hundreds of million of people living in coastal areas (Oppenheimer and Sebesvari, 2019).

There are still many unknowns and poorly understood processes that govern glacier dynamics (e.g. Pattyn, 2010), and thus, there is still plenty of room to improve our understanding of how glaciers flow and how they will affect us. In the rest of this introduction we will do an overview on how we model glaciers and some of the open questions that still stay opened. We will continue with a description of the history of Glacier d'Argentière. Finally, we will provide the objectives set up for this PhD and lay out the structure of the document.

Figure 1.1: View of Glacier d'Argentière from the moraine on the west side, the perspective is against the flow. The glacier lies on a valley carved through the granite and gneiss of the Mont Blanc range. The ablation zone can be seen on the lower and right side of the picture. The lateral crevasses, typical of glacier margins, can be well seen in the lower left. The central dark lines are made of rocks, that fall from the surrounding mountains and are transported with the flow and rest uncovered, as all snow has already melted. The accumulation zone is behind the turn on the left side of the picture. Photographed by Bruno Jourdain in September 2019, and used with permission.

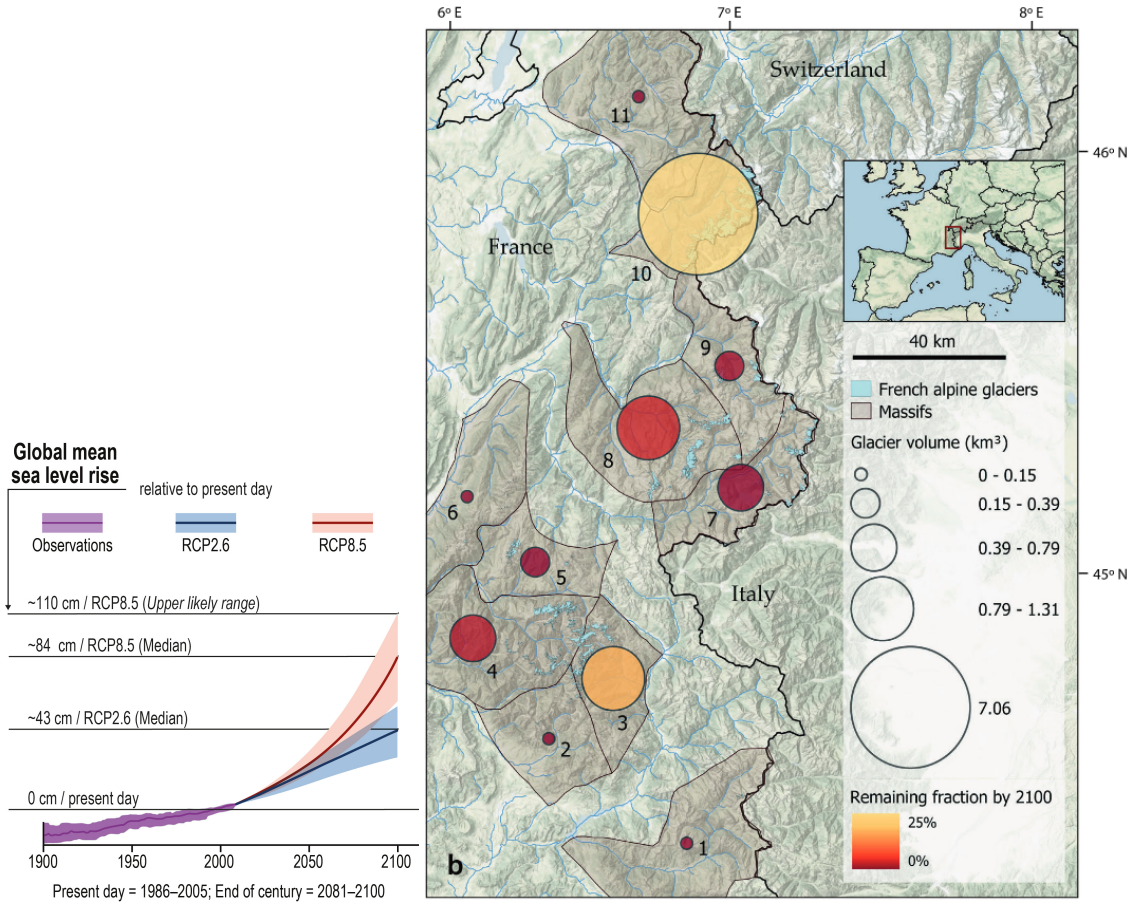

Figure 1.2: Projections of sea level rise under different climatic scenarios and expected ice mass loss in the French Alps by 2100. Panel (a) is adapted from the *Special Report on the Ocean and Cryosphere in a Changing Climate*, Oppenheimer and Sebesvari (2019). Panel (b) is extracted from Bolibar et al. (2022)

1.2 How do glaciers flow?

1.2.1 Early glaciology

Between the XIVth and the end of the XIXth centuries, Europe was experiencing an intermittent period of cold temperatures and glacier advance, the so-called 'Little Ice Age'. From the XVIth century onward, glacier advance became more widespread (Francou and Vincent; Solomina et al., 2016), and glaciers started to get the attention of the public. If at the beginning the glaciers were considered dangerous environments that threatened towns with their continuous advance (Rémy and Testut, 2006), such that priests had to be called to make the glaciers stop (as was done with success in the French and Swiss Alps (Francou and Vincent)), towards the end of the XVIIIth century the Illustration, and later the romanticism, changed the scientific and the general point of view on glaciers. Researchers began to ask themselves what were glaciers, and how they moved. The theories, much as glaciers during these centuries, followed a cycle of advance, retreat, and advance again, during which glaciologists combined field observations of increasing accuracy with theories of increasing complexity.

Pioneering among them, Saussure expanded on previous ideas and proposed in 1769 that glaciers moved by sliding over their beds as a solid block of ice, thanks to the presence of liquid water that lubricates the bed.

Another theory called dilatation found its strongest defender in the naturalist Louis Agassiz. In this mechanism, the water at the surface that falls through crevasses and moulins freezes when reaches the bed of the glacier. Since water expands upon freezing, this causes the glacier to increase its volume, expanding forwards. A variant of the dilatation theory was the regelation theory, developed later in the XIXth century and whose maximum exponent is John Tyndall. Tyndall proposed that glaciers advance by a combination of melting due to increased pressure and downstream refreeze of the meltwater. The dilatation/regelation theory became immensely popular during the mid XIXth century until well into the XXth century (Rémy and Testut, 2006) thanks to the efforts of Agassiz and Tyndall to refute other competing theories, their wealth of evidence, and the used of their respective reputation and manly exploration feats to push their ideas and mobilize support for them (Schaer, 2001; Rémy and Testut, 2006; Carey et al., 2016).

In the meantime, another school of glaciologists appeared, those supporting the 'Viscous Theory of Glaciers' as called by his most arduous defender, James Forbes (Forbes, 1959). The proponents of this theory were based on the fluid-like behaviour of glaciers, that adapted to the shape of the valleys and moved like 'liquor in a vase'. This mechanical behaviour could explain Forbes' observations that glaciers moved faster at the center and postulated that glaciers moved faster at the surface than at the bed (Forbes, 1959). Forbes also intuitively recognised the role of water in regulating glacier flow, observing that glaciers moved faster when the air temperature was hotter, and when their 'veins' were full of meltwater (as in summer). Unable to explain the solid-like behaviour of ice, such as crevasses, and confronted to Tyndall, support for the fluid theory was disregarded[1].

The last twist of the story arrived at the first half of the XXth century, during which the tide turned again towards the deformation and sliding theories. While theoretical models of glacier flow started to use the Navier-Stokes equations since 1906, more accurate observations of sliding and deformation supported this change of doctrine (Rémy and Testut, 2006). The entrance of fluid dynamics opened another line of research, whose echoes are found in this PhD: the rheology of ice, i.e. the relationship

[1]Forbes addressed the small success of the fluid theory as a gentleman, stating *It is often difficult to obtain a calm and full hearing for any new theory or experimental investigation; not because there is any antipathy to novelty, or that experiment is undervalued, but simply because, in an age of bustle and struggle for pre-eminence, each man is so busy with his own reputation, or the means of increasing it, that he has no leisure to attend to the claims of others* (Forbes, 1959)

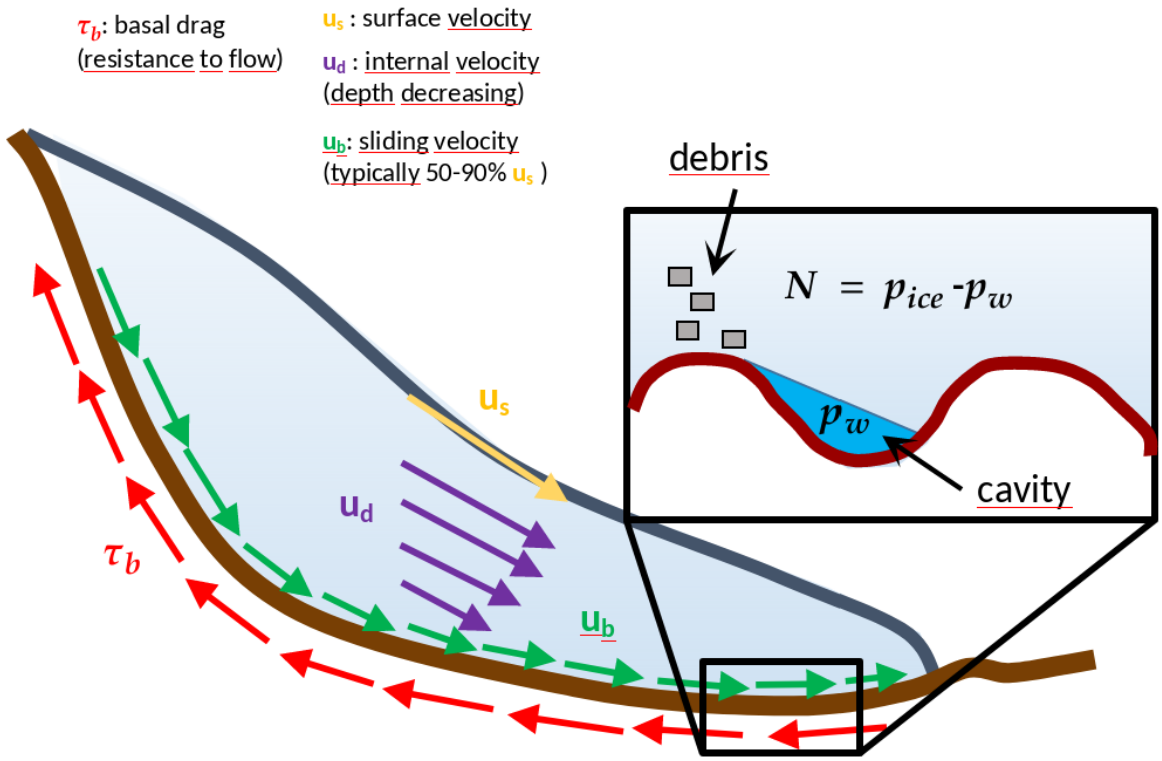

Figure 1.3: Scheme of a glacier with the elements discussed in this introduction. This figure also complies with the unwritten law that a PhD on glacier dynamics must, at some point, show a scheme of this type. **This is an early iteration of the picture, to illustrate what I want to do. I think I need to add: 1) Friction law =** $\tau_b = f(u_b)$ **2) Take the screenshot without the red lines :). 3) Add moulins and crevasses**

between force and deformation in a fluid. If ice was a fluid, was it a newtonian fluid, such as water but much more viscous, as initially assumed by Weinberg, Somigliana and Lagally (Perutz, 1947; Rémy and Testut, 2006), or was it a plastic material, such as metals (Seligman, 1949)? What was the relationship between the rheology of ice and the sliding and the base? The answer given to those questions in the 1950's and later decades founded today's physical framework of glacier dynamics.

1.2.2 Current framework and challenges

From the mid XXth century onwards, physicists and mathematicians started to get interested in glaciology, bringing a new dimension to the understanding of glacier dynamics (Clarke, 1987), as depicted in Figure 1.4.

The observations of Perutz (1949, 1950) showed that glaciers moved faster at the surface, observations that would be confirmed by even more observations later (Sharp, 1953; Mathews, 1959, e.g.). After shearing ice in the laboratory Glen (1955) showed that glaciers deformed non-linearly under continuously applied stress, setting the basis for modern understanding of glacier flow. Ice, therefore, was indeed a very viscous fluid. Since the seminal work of Glen, great efforts have been carried out to validate his work, determine the values of the parameters that control ice deformation, and establish the control of physical variables such as temperature, water content (Duval, 1977; Adams et al., 2021), or ice grain size in ice deformation. However, the complexity of ice rheology makes it very difficult to properly constrain *in-situ* observations of glacier flow, and laboratory experiments are also not without problems, such as similarities between artificial ice and natural ice (Adams et al., 2021; Cohen, 2000), how well can natural conditions be reproduced in a laboratory setting, or the small spatial

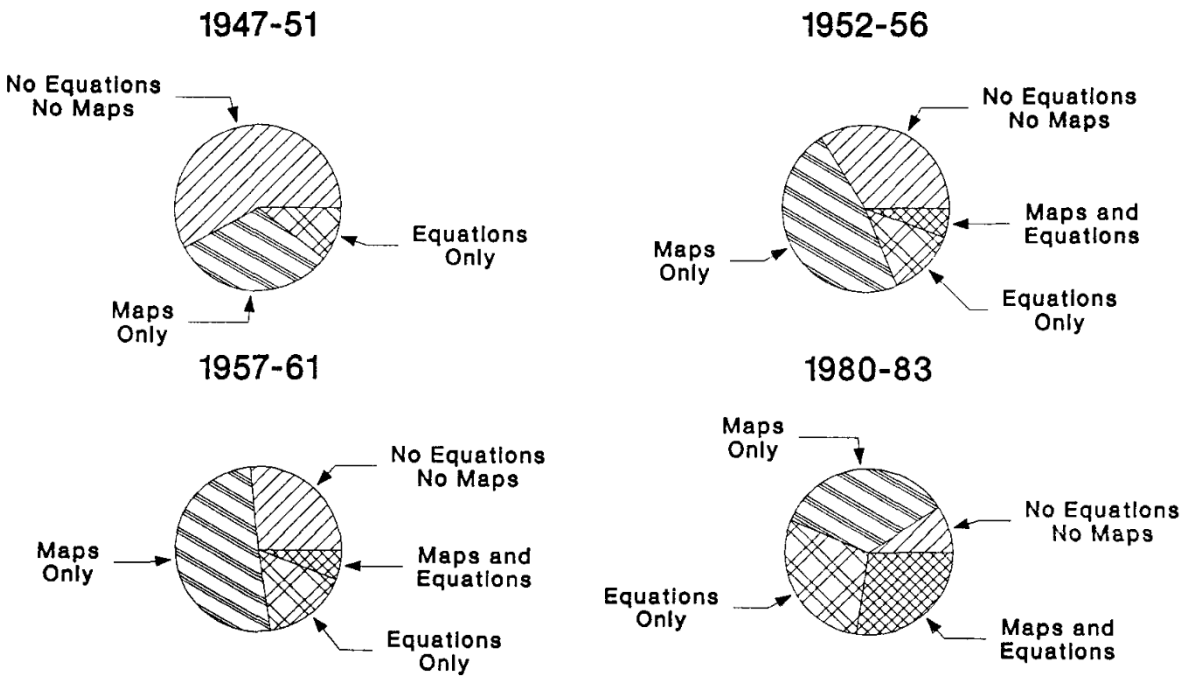

Figure 1.4: Evolution of the content in *Journal of Glaciolgy* during the 1947 - 1983 period, adapted from Clarke (1987). Equations pass from being present in less than one eighth of the publications in 1947-1951 to being in more than half the publications during the 1980-1983 period. This evolution is a result of the development of physical models in glaciology, i.e. the works of Weertman, Lliboutry, Röthlisberger...

and temporal scale that limit the experiments (Budd and Jacka, 1989). We give more details about the flow law proposed by Glen (1955) and the control on glacier deformation in chapter 2.

Parallel to the development of models and observations of ice deformation, glaciologists were also putting their attention at sliding, developing theories of how glaciers flow at their base, more or less backed by the available evidence. In this PhD we focus our study on hard-bedded glaciers, so we will ignore the research done on glaciers resting over sediments. The great kick-starter of hard-bed sliding theory was Weertman (1957), who proposed the first slip law (also known as friction law), a relationship between glacier sliding velocity and the drag (resistance to flow, τ_b in Figure 1.3) at the bed based on physical parameters. He envisioned that glacier slip at their base is a combination of two mechanisms. The first of them was the regelation around obstacles, and the second was enhanced creep, which results from increased deformation due to stress concentration at obstacles (a result of the flow law proposed by Glen (1955)). Shortly thereafter, Lliboutry (1958) proposed an additional mechanism, cavity opening[2], which could explain the fast speeds observed in some glaciers. In this third mechanism (see Figure 1.3), the water at the base of glaciers drowns part of the obstacles, reducing the apparent roughness of the bed so that glaciers slide faster. For the following years, Weertman and Lliboutry battled each other as to whom had the best understanding of sliding (Fowler, 2011), while other researchers provided increasingly complex friction laws for hard beds (e.g. Nye, 1969; Morland, 1976a,b; Fowler, 1979, 1986, 1987; Gudmundsson, 1997b,a; Schoof, 2005; Gagliardini et al., 2007), that are still, at their core, a combination of several or all three processes of regelation, enhanced creep, and cavity opening. Most of these studies share common features: they consider two-dimensional bed geometries despite glaciers being three dimensional entities, most of them do not consider the additional friction caused by sediments in spite of the evidence of debris-laden ice or debris-related

[2]Also known as cavitation. We prefer 'cavity opening' to avoid confusion with the more common cavitation considered in hydrodynamics, i.e. the phenomenon of bubble formation and bursting taking place in water flowing at high velocities.

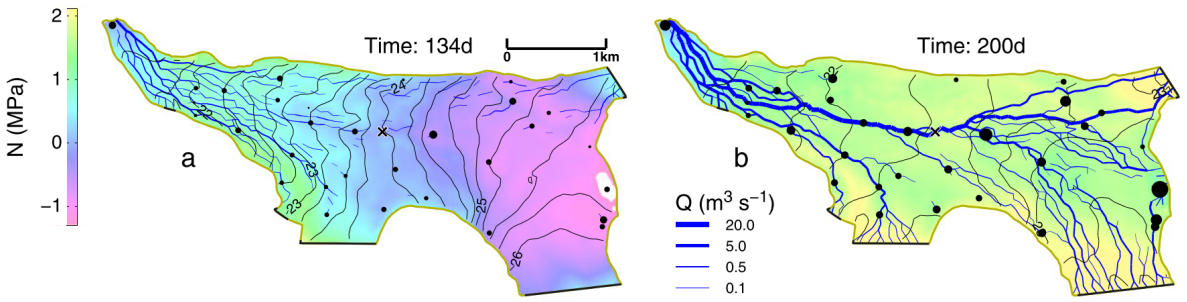

Figure 1.5: Effective pressures (a) and (b) retrieved in subglacial hydrology simulations done of the 2007 melt season of Gornergletscher (Switzerland). On panel (a), the subglacial hydrology system is made of a few, relatively small channels, specially on the lower part of the glacier (the left side). The upper part of the glacier is under high subglacial pressures, which sometimes even surpass the ice overburden pressure, thus reaching negative effective pressures N. On panel (b), the system has transitioned to an efficient hydrology system. Channels have grown and can sustain higher discharge Q, represented by the increase in density and size of the blue lines. As a result, the subglacial pressure decreases, and the effective pressure N increases towards the overburden pressure. Adapted from Werder et al. (2013).

phenomena at the base of glaciers (e.g. Cohen et al., 2005; Helmstetter et al., 2015), and all of them are formulated for the steady state.

Large-scale studies of glacier flow over hard beds usually consider the law of Weertman (1957) as basal boundary condition. This choice of one friction law over another has a great impact in glacier velocities, and affects future estimates of glacier flow and sea level (Ritz et al., 2015; Brondex et al., 2017, 2019; Pattyn and Morlighem, 2020). Due to the impact of this choice, and the fact that it is an unavoidable element in glacier models, recent studies have researched the limits and the applicability of these laws. Thus, Helanow et al. (2020, 2021) showed that these type of friction laws are extendable to synthetic and real three dimensional beds. Field validation has been performed in the long term analysis of velocities at Glacier d'Argentière by Gimbert et al. (2021b), and in the spatial analysis of velocities in the Greenland Ice-Sheet by Maier et al. (2022). These studies reveal that a law that integrates creep enhancement and cavity opening, developed based on physical reasoning, are indeed representative of glacier sliding over hard beds. Regarding the effect of additional friction, some studies (Fowler, 1979; Iverson et al., 2019) have discovered that debris at the base, at least in low quantities, does not change the form of friction laws. We explore this last point in detail in chapter 3.

The remaining aspect of glacier dynamics that we will introduce here is the role of water. During the 60's and 70's, models of sliding included the role of subglacial pressures in regulating the basal speed (e.g. Weertman, 1964; Lliboutry, 1968; Budd et al., 1979), the first models of subglacial hydrology were appearing (Röthlisberger, 1972; Weertman, 1972), and field observations of water pressures, subglacial discharge and subglacial channels and/or cavities, among others, formed the foundation of our knowledge of subglacial hydrology.

The overall consensus can be resumed in the following lines. Water crevasses and moulins (cracks and vertical openings in the glacier) route superficial and englacial water, originated from surface melting, rain, supraglacial and englacial lakes, deformation melting, etc, towards the base. If the base is temperate, the water reaches the bed and forms part of the subglacial hydrology system. How water is spread along the bed depends on the subglacial water pressure, which is intrinsically coupled with water input, discharge and glacier velocities. During periods of low water discharge, typically winter, water is distributed in a network of cavities, which are pockets of water that typically open at the lee (up-glacier) side of bed obstacles (Lliboutry, 1968;). These cavities are either connected, thus allowing for water flow between them through tortuous, narrow waterways, or isolated from the main

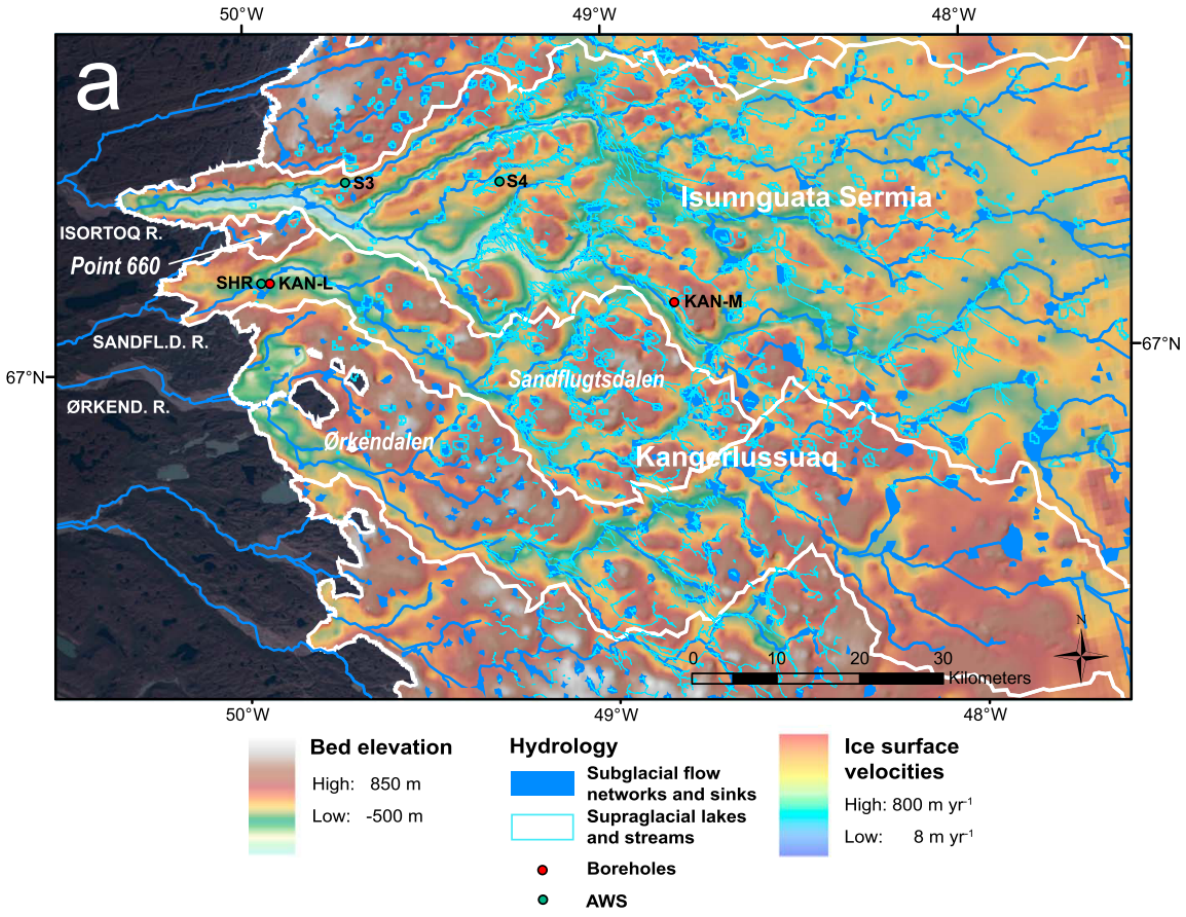

Figure 1.6: Predicted subglacial hydrology network in Isunnguata Sermia and Kangerlussuaq catchments, a land-terminating sector of the Greenland Ice Sheet. Chandler et al. (2021) observe that this system shows the expected evolution of inefficient to efficient during the onset of the melt season.

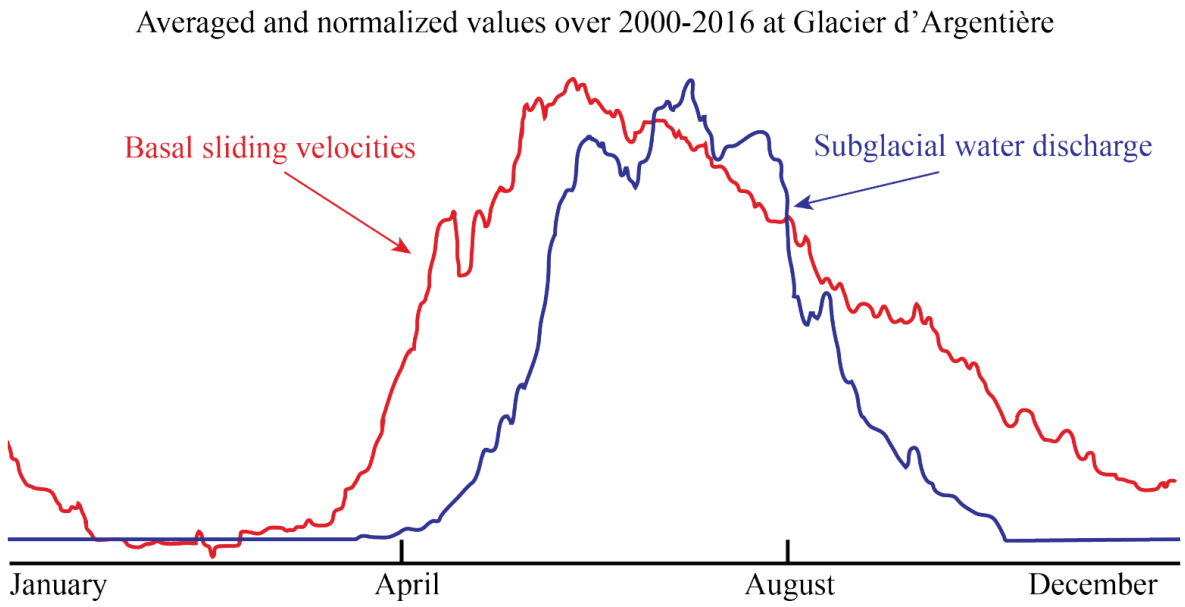

Figure 1.7: Averaged normalized water discharge (blue) and basal sliding velocities under the natural cavity (red) at Glacier d'Argentière (France), averaged over the 2000-2016 period. See Vincent and Moreau (2016) for absolute values. Diagram taken from Nanni (2020b).

subglacial network. Flow within connected cavities is difficult, and thus the system is considered *inefficient*. Due to this inefficiency in discharging water, high water input results in increased storage, which increases subglacial water pressures (see Figure 1.5 (a)). Increased water pressure in the cavity system leads to, as commented before, faster glacier flow (Lliboutry, 1968). An increase in glacier speed due to increase in water input has been well observed a multitude of times, and typically takes place at the onset of the melt season (e.g. Iken and Bindschadler, 1986), as a result of lake drainage (e.g. Chandler et al., 2021), or after rain events (e.g. Hooke et al., 1989). The increase in the volume of stored water eventually connects cavities between them with large conduits, and water flow concentrates forming channels, that join each other in an arborescent network (see Figures 1.5 and 1.6). These channels discharge water at lower pressures and higher water flux, thus the system is called *efficient*. The glacier slows down as water storage decreases, and the channel network collapses when water input eventually drops. This transition can be observed in Figure 1.8, where the lag between increases in basal velocities at the cavitometer (later discussed in chapter 6) and water discharge is thought to indicate the reaction time of the system as it adapts from a cavity-driven system to a channelized system (around April in Figure 1.8), and conversely for the decrease in both signals after August (Vincent and Moreau, 2016). Detailed observations show that the subglacial hydrology system is spatially complex, and close regions of the bed can display very different behaviour (Willis et al., 2003; Rada and Schoof, 2018) due to disconnected cavities that stay at high pressures (Rada and Schoof, 2018). In chapter 6 we will go over our observations of surface, internal and basal velocities at Glacier d'Argentière, and discuss our findings in terms of the possible evolution of the subglacial hydrology system.

While the influence of unsteady water pressures on sliding has been observed for decades, it is recently that models coupling ice flow and unsteady water pressures are appearing (Thøgersen et al., 2019; Tsai et al., 2021; Gilbert et al., Submitted). In chapter 4 we describe an unpublished model of sliding under unsteady water pressures developed by Louis Lliboutry in 2005. In chapter 8 we will describe the efforts done in the last years in our group to link glacier friction laws with unsteady water pressures.

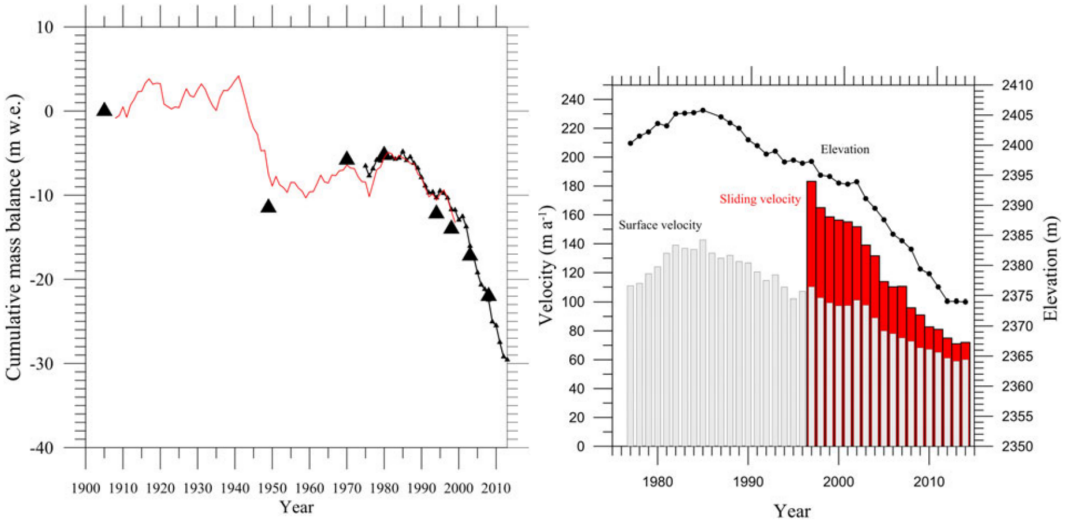

Figure 1.8: Cumulative mass balance of Glacier d'Argentière in the last century (left) and evolution of the dynamics at its ablation area (right) from 1977 to 2014, taken from Vincent and Moreau (2016). These two graphs show the clear link between glacier volume and velocities. The decline of the glacier has continued since these data were published, and surface velocities for 2020 and 2021 were lower than 50 m a^{-1} on average.

1.3 Glacier d'Argentière

While the aim of this PhD is universal, and directed towards understanding the flow of any glacier in the world, we focus part of our investigations in one particular french alpine glacier, Glacier d'Argentière. Glacier d'Argentière (see Figure 1.1) is a temperate glacier located in the Mont Blanc range, french Alps (45°10 N, 6°10 E). The glacier rests on hard bedrock and extends for 9 km within an altitude range of 1600 m to 3400 m, separated by an icefall at an altitude of 2300 m. It has a maximum thickness of about 250 m to 230 m on the centerline of the ablation area (Vincent et al., 2009; Sergeant et al., 2020), flowing at an average speed of roughly 47 m a^{-1} in 2021. The proximity of the glacier to populated areas and its accessibility have allowed researchers to study Glacier d'Argentière since long time. Additional interest stems from the hydropower company Electricité d'Emosson, which since 1975 catches the subglacial flow of Glacier d'Argentière to provide electricity (d'Emosson SA). As a result, Glacier d'Argentière has a wealthy record of mass balance (one of the longest records in the world), ice cover, ice thickness, surface velocities, subglacial flow, among others (Vincent and Moreau, 2016). Of particular interest is the measurements of the sliding velocity under a natural cavity close to the ice-fall, a picture of which is later given in Figure 3.1. In the last years, the instrumentation network has been extended with a GNSS network (Togaibekov et al., 2022), seismometers (Helmstetter et al., 2015; Nanni et al., 2020a, 2021; Gimbert et al., 2021b), englacial tiltmeters (Roldan-Blasco et al., see also chapters 3 and 7) and other sensors (e.g. automatic weather stations, *smart* ablation stakes (Rabatel and Biron)), all of which allow for continuous survey of the behaviour of the glacier at short time-scales.

Glacier d'Argentière shows features typical of alpine glaciers. It has been retreating since the end of the Little Ice Age, with a marked acceleration in mass loss from early 2000's up to now, as shown in Figure 1.8 (Vincent, 2002; Vincent and Moreau, 2016). Surface dynamics shows a seasonal pattern typical of mountain glaciers (see Figure 1.7), with low velocity between September and April, followed by a period of sustained high velocity between May and August (Vincent and Moreau, 2016; Gimbert et al., 2021b; Vincent et al., 2022a). High subglacial runoff is observed during the summer period, and melt season acceleration as well as late summer deceleration is paired with fast increase and decrease of subglacial runoff, respectively (Vincent and Moreau, 2016; Vincent et al., 2022a), as can be

observed in Figure 1.7. Observations of the local behaviour of the subglacial hydrology network are somewhat contradictory, however. Hantz and Lliboutry (1983) measured borehole water pressures at Glacier d'Argentière and determined that there probably was a channel on the right margin of Glacier d'Argentière that regulated the water in cavities on the central part of the glacier. They did not identify any particular channel (or waterway, as they called) draining the over-deepened area of the glacier. On a similar note, Vincent et al. (2022a) observed surface uplift during several summers, which could only be explained with summer increasing cavity volume in the central part of the ablation area. On the other hand, Nanni et al. (2021) observed active subglacial flow at the onset of the 2019 melt season. Based on tracing the noise generated by turbulent water flow, they determined that the subglacial network transitioned from a distributed, low efficient network, to a more concentrated network with a central channel, in line with what's commonly assumed.

All these measurements are accompanied by an equally powerful set of numerical simulations on the glacier. We have a three dimensional model of Glacier d'Argentière, that solves glacier flow without approximations, and accurately represents glacier surface velocities and ice thickness. We provide an example of the use of this model in chapter 6.

In resume, Glacier d'Argentière is a perfect natural and numerical laboratory for studying and glacier flow, and improving our understanding of it. In this PhD, we continue this line of work, already developed for more than 50 years.

1.4 Objectives of this PhD

After these introductory words, it should be clear that there are still many open fundamental questions regarding the flow of glaciers, all of which impact the assessment of the current and future state of the cryosphere. In this PhD, we will explore a diverse set of these questions, listed below:

1. Improve our understanding of glacier sliding with the suppression of the pure-sliding assumption
2. Uncover, structure and explain the last glacier model of Louis Lliboutry, which in his own words was 'a realistic model taking into account the laws of Mechanics and Physics' left for 'the younger researchers' to exploit
3. Observe the internal deformation and infer the basal velocity at Glacier d'Argentière at annual and seasonal timescales
4. Constrain the rheology of ice at Glacier d'Argentière using a combination of accurate in-situ observations of surface and internal velocity and high order numerical modeling

1.5 Structure of this work

This manuscript is made of 9 chapters, structured thematically. The first of them is *Introduction*, the chapter that the reader is just finishing now. Then, there are three chapters devoted to modeling of glacier flow. In *An introduction to ice continuum mechanics*, we set the very basis for understanding the mechanical developments partaken in the rest of the document. *The effect of local shear stress on glacier sliding* follows, in which we review our work on glacier friction laws for modeling flow of ice with non zero local shear stress at the base. Then, in *The lost last paper(s) of Louis Lliboutry* we shed a light on an unpublished glacier model developed by Louis Lliboutry shortly before his death. We follow with three chapters devoted to observations of glacier deformation and sliding. The first of

them is *Borehole inclinometry and related field surveys*, in which we introduce the technique of borehole inclinometry and review the studies carried out with this technique in temperate glaciers. We continue with *Deformation, sliding, and creep enhancement in a temperate alpine glacier*, in which we show our observations of internal deformation during 2020 in Glacier d'Argentière, and what conclusion we draw regarding its dynamics and ice rheology. The closing chapter of this set of three is *Inclinometry on the right margin of Glacier d'Argentière*, where we show the preliminary results on the field campaign that followed the 2020 borehole survey. The next two chapters close the PhD. *Next steps* shows some research work related to this PhD. In particular, we discuss the preliminary study on unsteady flow over sinusoidal beds done by different researchers in our group, and an assessment of water content in Glacier d'Argentière carried out during 2022. We finish with the chapter *Conclusions*, which provides an overview of the PhD and the achieved goals.

Chapter 2

An introduction to ice continuum mechanics

Mr Roldan, I haven't understood a single thing
My 'Mechanics of deformable solids' students, 2020-2021 and 2021-2022 cohorts

2.1 Introduction

In this chapter we will introduce basic concepts of continuum mechanics, and its applications to modeling ice dynamics. Many of the concepts are, for brevity, explained in less details in the following chapters, so we will use this section to lay them out with greater detail.

For those unfamiliar with the subject, continuum mechanics deals with the movement and deformation of continuous media. It is a very powerful tool to model the behaviour of solid and fluids, yet not an easy one to work with, since its mathematical representation can oftentimes become cumbersome (hence the opening quote). An assessment of such power is found in the amount of accurate mechanical analysis of glacier and ice-sheet flow performed prior to the advent of large-scale remote sensing techniques and numerical modeling techniques, Glen (e.g. 1955); Weertman (e.g. 1957); Nye (e.g. 1965); Lliboutry (e.g. 1968); Raymond (e.g. 1971); Hooke (e.g. 1973).

We will start the chapter with a short description of stress, strain rate, and the constitutive relation commonly used for ice. We will continue with a few notes on commonly assumed ice mechanical properties that will later be considered in this thesis. We will finish with a simplified view of the form of the vertical distribution of the stress and strain rate that can be reasonably expected in a glacier.

2.2 Stress and strain rate

2.2.1 General description

In a continuum mechanics framework objects deform when subjected to stress. In Figure 2.2 we schematize how a square volume deforms under compression, tractions, and shearing stress. Stress is a measure of force by unit area, therefore it represents a distributed force acting on a surface. strain rate is the rate (i.e. speed) of deformation, and measures how fast a medium, typically a fluid,

is deforming under continuously applied stress.

Ice is a mechanically complex material whose response to stress depends on the applied stress and the strain rates at which it is deforming. At the timescales relevant for glacier flow, we can assume that ice is a viscous fluid deforming at low strains, such that infinitesimal strain theory applies. This framework fails at correctly modeling processes involving large deformations, or happening at very short timescales, such as ice calving or crevasse opening, which require the use of more complex formulations of ice deformation, either with viscoelastic models within infinitesimal strain theory or within finite strain theory (Goldberg et al., 2014; MacAyeal et al., 2015; Christmann et al., 2019). Fortunately for us, during this PhD we will stay within the range of time and strain scales covered by infinitesimal strain theory.

2.2.2 Mathematical representation of vectors and tensors

We will start by assuming that we are working with a three dimensional ortonormal reference system, of directions x_1, x_2, and x_3, which we will also call x, y, and z respectively. We will identify x_1 (or x) with the along flow horizontal direction, and x_3 (or z) with the upwards vertical direction. Vectors, or first order tensors, such as velocity, will therefore have three components, one per direction. For a given vector a, its components will be a_1, a_2 and a_3, equivalent to a_x, a_y, and a_z. Second order tensors (abbreviated to just tensors, most of the time) have nine components, one per each unique combination of two directions. For a given tensor $\mathbf{A}$, the nine components will be A_{11}, A_{12}, A_{13}, A_{21}, A_{22}, A_{23}, A_{31}, A_{32}, and A_{33}. A typical example of second-order tensor that will appear often in this PhD is the velocity gradient tensor $\mathbf{L}$, represented by

$$\mathbf{L} = \nabla\mathbf{u} = \begin{pmatrix} L_{11} & L_{12} & L_{13} \\ L_{21} & L_{22} & L_{23} \\ L_{31} & L_{32} & L_{33} \end{pmatrix} = \begin{pmatrix} \frac{du}{dx} & \frac{du}{dy} & \frac{du}{dz} \\ \frac{dv}{dx} & \frac{dv}{dy} & \frac{dv}{dz} \\ \frac{dw}{dx} & \frac{dw}{dy} & \frac{dw}{dz} \end{pmatrix},$$

with $\mathbf{u} = (u, v, w) = (u_1, u_2, u_3)$ the velocity vector. In this case, any component L_{ij} refers to the derivative of the u_i component with respect to the direction x_j. Thus, L_{11} is equivalent to du/dx, L_{12} is equivalent to du/dy, L_{13} is equivalent to du/dz, and so on. The gradient can also be written with the gradient operator $\nabla = \partial/\partial x_j$ We will further develop this tensor in chapter 5.

Stress and strain rate are represented with second-order tensors $\boldsymbol{\sigma}$ and $\dot{\boldsymbol{\varepsilon}}$, called the Cauchy stress tensor and the strain rate tensor, respectively. At any given point of space, the term σ_{ij} represents the j component of the force per unit area acting on a plane with normal x_i. Figure 2.1 illustrates an example of how to translate forces into stress. Let's consider a force $\mathbf{F} = (F_1, F_2, F_3)$ acting on a point P, and a horizontal plane with normal vector $n = (0, 0, 1)$ passing through P, such that we can define the force per unit area $\mathbf{F_{surf}} = (F_1, F_2, F_3)/(dx_1 dx_2)$ for an infinitesimal surface of area $dx_1 dx_2$. This allows us to obtain already three components of the Cauchy stress tensor $\boldsymbol{\sigma}$. The first component is $\sigma_{31} = \sigma_{13} = F_1/(dx_1 dx_2)$, which over this plane is a shearing stress, as F_1 is parallel to the plane. The second component is $\sigma_{32} = \sigma_{23} = F_2/(dx_1 dx_2)$, which is also a shearing stress. The third component is σ_{33}, which is a compressive stress, since it is normal to the surface, and towards the surface.

In glaciology, we usually consider the stress tensor $\boldsymbol{\tau} = \boldsymbol{\sigma} - 1/3tr(\boldsymbol{\sigma})\boldsymbol{I}$, which is the deviatoric part of the Cauchy stress tensor. The reason behind this is that the isotropic pressure $\mathbf{p} = 1/3tr(\boldsymbol{\sigma})\boldsymbol{I}$, called the spherical part of $\boldsymbol{\sigma}$, has no effect on the deformation of incompressible media such as ice. Due to equilibrium conditions, it can be proven that $\boldsymbol{\sigma}$ and therefore $\boldsymbol{\tau}$ are symmetric. Conversely for the strain rate, $\dot{\boldsymbol{\varepsilon}}$ is defined as the symmetric component of $\mathbf{L}$, therefore $\dot{\boldsymbol{\varepsilon}} = 1/2(\mathbf{L} + \mathbf{L}^T)$, with $\mathbf{L}^T$ the

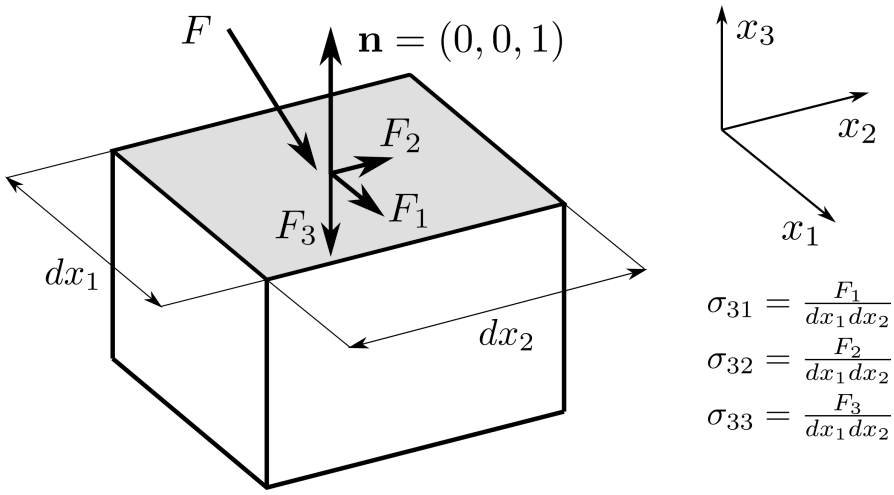

Figure 2.1: Scheme of forces and the derived Cauchy stress acting at a point over a horizontal plane.

transpose of $\mathbf{L}$. Because they are symmetric, $\boldsymbol{\tau}$ and $\dot{\boldsymbol{\varepsilon}}$ only have six independent components:

$$\boldsymbol{\tau} = \begin{pmatrix} \tau_{11} & \tau_{12} & \tau_{13} \\ \tau_{12} & \tau_{22} & \tau_{23} \\ \tau_{13} & \tau_{23} & \tau_{33} \end{pmatrix}; \; \dot{\boldsymbol{\varepsilon}} = \begin{pmatrix} \dot{\varepsilon}_{11} & \dot{\varepsilon}_{12} & \dot{\varepsilon}_{13} \\ \dot{\varepsilon}_{12} & \dot{\varepsilon}_{22} & \dot{\varepsilon}_{23} \\ \dot{\varepsilon}_{13} & \dot{\varepsilon}_{23} & \dot{\varepsilon}_{33} \end{pmatrix} = \frac{1}{2} \begin{pmatrix} 2\frac{du}{dx} & \frac{du}{dy} + \frac{dv}{dx} & \frac{du}{dz} + \frac{dw}{dx} \\ \frac{dv}{dx} + \frac{du}{dy} & 2\frac{dv}{dy} & \frac{dv}{dz} + \frac{dw}{dy} \\ \frac{dw}{dx} + \frac{du}{dz} & \frac{dw}{dy} + \frac{dv}{dz} & 2\frac{dw}{dz} \end{pmatrix}. \tag{2.1}$$

2.3 Ice rheology and constitutive law

So far, we have no information about the type of material that we are studying, which means we have no way to link stress and strain rate, which is our ultimate goal.

Ice is a polycrystalline material, made of a collection of crystals (also called grains), that present many discontinuities in their crystal structure, and at the boundaries between grains. These defects allows for the atoms that conform the crystals to move over the dislocations, facilitating the deformation of the crystalline structure. For a single ice crystal, this deformation happens along a plane, called basal plane, whose orientation is called c axes. The arrangement of c axes in a group of crystals is called the fabric. If a group of crystals have their c axes uniformly distributed on directions, then there is no preferred orientation for deformation, and the ice has an isotropic fabric and an isotropic behaviiour at the scale of the policrystal. Otherwise, it is anisotropic, with one or several preferred directions for deformation. Ice fabric, and crystal size, evolve as ice deforms, and can be used to study the history of stress of an ice sample (e.g. Raymond, 1971; Vallon et al., 1976).

At a macroscopic level, ice behaves as an incompressible fluid, such that when subjected to any deformation regime, its density ($\rho_i \approx 900$ kg m^3) does not change. In terms of strain rate this is equivalent to imposing that the trace of the strain rate tensor is zero,

$$tr(\dot{\boldsymbol{\varepsilon}}) = \dot{\varepsilon}_{11} + \dot{\varepsilon}_{22} + \dot{\varepsilon}_{33} = 0. \tag{2.2}$$

Thus, the number of unknown components of the strain rate tensor is reduced by 1. By definition, $\boldsymbol{\tau}$ is also trace-less.

The other 5 must be either known (or *assumed*, as we will do a few times in this PhD) or computed via the stress tensor. To link the deviatoric stress tensor and the strain rate tensor we will use a constitutive law, of the form $\dot{\boldsymbol{\varepsilon}} = f(\boldsymbol{\tau})$.

2.3.1 Glen flow law

The most common constitutive law for ice used in glaciology is the isotropic Glen's flow law (Glen, 1955),

$$\dot{\varepsilon}_{ij} = A\tau_E^{n-1}\tau_{ij}, \tag{2.3}$$

where A and n are material parameters called creep factor (also known as rate factor) and Glen's flow law exponent, respectively, and τ_E is the effective stress, a scalar measure of the deviatoric stress, computed with the deviatoric stress tensor at any point,

$$\tau_E^2 = \tau_{ij}\tau_{ij} = \frac{1}{2}(\tau_{11}^2 + \tau_{22}^2 + \tau_{33}^2) + \tau_{12}^2 + \tau_{13}^2 + \tau_{23}^2. \tag{2.4}$$

Therefore, we can see that ice deformation in any given direction ij (or, more accurately, strain rate) depends on material parameters (A and n), on the stress acting in said direction (τ_{ij}) and, very importantly, it depends non-linearly on all the other stress components. This brings all sorts of problems in modeling glacier dynamics and is one of the reasons why ice, despite being a slow moving fluid, is so difficult to study. In chapter 3 we will see one implication of this non-linear relation between strain rate and stress.

Glen's flow law was proposed for ice undergoing secondary creep, a creep regime for deviatoric stress roughly between 0.050 and 0.150 MPa (Lliboutry and Duval, 1985; Hooke, 2005; Cuffey and Paterson, 2010). For higher stress, experiments suggest that another type of creep regime, called tertiary creep, develops. Tertiary creep is characterized with softer ice and fabric development (anisotropy).

Nevertheless the potential inadequacy of Glen's flow law for modeling ice flow in some particular places of a glacier, it is widely considered a good approximation to model the overall ice flow of glaciers (Cuffey and Paterson, 2010), and as such, it should not be surprising that it may need some adjustments when we confront the law to actual field data. For what is left of this section, we will review with a little bit more detail the material parameters n and A, and how field observations and numerical modeling allows us to better adjust their values.

2.3.2 Glen's flow law exponent

The flow exponent is typically assued to be $n = 3$, following the value proposed by Cuffey and Paterson (2010) after reviewing many different laboratory experiments and field observations. It is the default value considered when modeling ice dynamics, common in an wide array of ice flow studies, ranging from future glacier evolution (e.g. Bolibar et al., 2022), contribution of glaciers to sea level rise (Ritz et al., 2015, e.g.), reconstruction of glaciers during past glaciations (**?**, e.g.), study of basal conditions such as melting (Karlsson et al., 2019, e.g.), basal velocities (Vincent and Moreau, 2016, e.g.), basal drag (Morlighem et al., 2013, e.g.), and bed erosion (Herman et al., 2015, e.g.), inversion of thickness (Millan et al., 2022, e.g.), the list goes on.

The influence of n on ice flow is important, since the higher n is, the softer ice becomes for an applied stress, and the more sensitive it is to the overall stress state. A multitude of studies suggest values between 2 and 4 (Cuffey and Paterson, 2010), and later studies at the natural scale propose a value that is closer to 4, therefore, that ice is softer than we usually consider. For low stress ($< 50-100$ kPa, depending in the study) it has been observed (Marshall et al., 2002; Chandler et al., 2008, e.g.) that ice behaves as a linear fluid as other mechanisms dominate deformation. Thus, in this scenario $n \approx 1$ and strain rates are directly proportional to the applied stress τ_{ij}.

In order to determine n, the most direct solution implies knowing (or at least having good constrains on) the strain rate and stress tensors, since rewriting Eqn. (2.3) gives

$$n = \frac{\log \dot{\varepsilon}_{ij}}{\log \tau_{ij}}.$$

Examples can be found in Marshall et al. (2002), where borehole inclinometry was used to constrain $\dot{\varepsilon}_{ij}$ and with estimates of τ_{ij} they found $n = 1$ close to the surface, and $n = 4$ on the deeper part of the glacier. Another example is the analysis of Millstein et al. (2022) of the deformation of antarctic ice-shelves, where they found $n = 4.1 \pm 0.4$ in fast flowing areas. Studying ice-shelves over glaciers has the advantage that the ice-shelves stress state is well constrained and remote sensing techniques allow for a wealth of deformation data. Alternative methods imply trying different values of n until we are able to reproduce a set of observations. That is the case of Gillet-Chaulet et al. (2011), where using $n = 4.5$ allowed them to best match the shape of ice layers in an ice divide (a location in ice-sheets where stress and strain rate are well constrained).

The use of these methods require good constrains on A, or at least caution to not overlook the influence of A on the measured deformation. We will briefly see in chapter 6 that a depth dependent creep factor can provide a completely wrong value of n if the stress tensor is not well constrained.

2.3.3 Creep factor

The typical value of A at 0°, common in recent studies of glacier dynamics at the glacier scale (e.g. Vincent et al., 2022a), or ice-sheet scale (Morlighem et al., 2013; Maier et al., 2019), is $A = 80$ MPa^{-3} a^{-1}, for $n = 3$. Its value is highly dependent on many, usually unquantified, physical variables, as we will see below, and depends on the flow law exponent. This typical value of A was proposed by Cuffey and Paterson (2010) for $n = 3$ after a review of lab-based experiments and studies at the natural scale, such that it works as a sort of jack of all trades. They recognise the variable nature of it, and so recommend researchers to find the best value when possible for any given glacier. A typical approach for retrieving a sensible value for A is based on inversion methods. In this case, glacier observations (typically surface glacier velocities and ice thickness) are used to infer the value (or values) of A and other parameters that make the glacier behave as closely as possible to said observations. This methodology integrates all dependencies on A into one value, that is sometimes considered uniform for a single glacier (Roldan-Blasco et al.), uniform for a whole set of glaciers of the same region (Millan et al., 2022), or spatially heterogeneous depending on the zone of the glacier (Hill et al., 2018).

While determining the value of A is a difficult task, we have a better idea on the dependency on A with respect to different physical variables, of which we can list temperature, interstitial water content, fabric development, and impurity content. For simplicity, we will concentrate the effects of variables other than temperature in an enhancement factor E, that we define as

$$E = \frac{A}{A^*}, \tag{2.5}$$

where A^* is a sort of standard value of A, when the variables that modify the creep factor others than temperature are not present, i.e., if we consider the effect of water content, $A^* = A$ when there is no enhancement due to interstitial water content. Note that Cuffey and Paterson (2010) reserve the word *enhancement* only for those variations in strain that cannot be explained by variations in temperature or water content, and must be an effect of fabric development, impurities, and other variables.

Temperature

Temperature plays a key role in ice creep, with A increasing exponentially the closer the temperature gets to the ice melting point. This behaviour is typically modeled with an Arrhenius law,

$$A = A_0 \exp - \frac{QR}{T_h}. \tag{2.6}$$

In this case, A_0 is called prefactor, Q is an activation energy that depends on the temperature, R the gas constant and T_h is the temperature, adjusted for the melting point depression due to pressure. More complicated expressions of the temperature dependency of A are available in the literature. For the purposes of this PhD, we will only consider temperate glaciers, i.e. glaciers that are everywhere at their pressure melting point, such that we will not go further in the temperature control on A.

Water content

Water content effect on creep enhancement of temperate ice has been only measured in two laboratory experiments, by Duval (1977) and more recently by Adams et al. (2021). Each study focuses on different stress regimes, and as such they are not completely comparable. We will start with Duval (1977), then comment on Adams et al. (2021), and finish with what has been observed in temperate glaciers.

Duval (1977) analyzed the water content in ice samples retrieved in 1971 in La Vallée Blanche (France), a tributary glacier of Mer de Glace (France). The procedure consisted in straining the ice at tertiary creep and measuring the stress and strain. Without stopping the experiment, they passed a cold wave through the ice samples, and measured the time Δt it took for the cold front to travel through a distance Δx. The speed of the cold front, $\Delta x / \Delta t$,allows to determine the amount of water in the sample by solving a Stefan problem. Their results suggest a linear relationship between ice creep and water content in the ice, which once rewritten in the form of an enhancement factor yields

$$E = 1 + 2.34w, \tag{2.7}$$

with water content w in %, and for $n = 3$. The w measured at temperatures between 0°C and 0.20°C ranged from 0 to 0.7 ± 0.1 %.

More than 40 years later, Adams et al. (2021) performed similar experiments on deionized lab-made ice, mostly sheared at secondary creep, and extending the range of water content beyond the 0.7% studied by Duval (1977) up to 1.7 ± 0.23 %. For better comparison purposes, they also ran one experiment at tertiary creep, with $w = 0.31 \pm 0.08$ %. While they don't provide a relationship between A and w, they observed the following:

1. A is more sensitive to w under secondary creep, than when deformed under tertiary creep.
2. For $w > 0.6$ %, ice under secondary creep becomes insensitive to further increments of w.
3. Additionally, for $w > 0.6$ % under secondary creep ice becomes linearly viscous ($n = 1$).
4. The results of the tertiary creep experiment were comparable to Duval (1977). The ice of Adams et al. was slightly stiffer than that of Duval, but it could be due to the use of deionized water (more details about the role of impurities later).

In view of their observations, Adams et al. (2021) recommend caution when extrapolating the model of Duval (1977) for $w > 0.7\%$. Unfortunately, the differences between both studies do not offer more light on the limits of their observations. In particular, we can ask ourselves if the switch from non-linear to

Study	Glacier	Area	Avg. w %	Method	Notes
Joubert, (1963)	Aiguille du Midi	Accum.	0.15 - 0.1	Calorimeter	Only surveyed upper part of the column
Lliboutry, (1971)	Aiguille du Midi	Accum. Ablat.	0 - 0.6 0 - 1.7	Calorimeter	No details on the spatial distribution
Vallon et al., (1976)	Vallée Blanche	Accum.	0.32 - 1.31	Calorimeter	Depth increasing w, drops at the bed
Lliboutry et al., (1985)	Argentière	Ablat.	0.71	Calorimeter	No trend with depth. Short scale variations
Murray et al., (2000)	Falljökull	Ablat.	0 - 3.3	GPR	Depth increasing w, drops at the bed
Benjumea et al., (2003)	Johnson	Accum.	0.6 - 2.3	GPR and seismics	Depth increasing w, drops at the bed
Hubbard et al., (2003)	Tsanfleuron	Both	$1W$ - $10.7W$	Ion concentration	Depth increasing w. W denotes w in the upper layers
Murray et al., (2007)	Tsanfleuron	Ablat.	1.18 - 3.8	GPR	Depth increasing w. Different layers than Hubbard et al. (2003)

Table 2.1: Measurements of water content in temperate glaciers, with emphasis on the studied area of the glacier and the in-depth distribution. We ignored studies that focused on basal ice, (Cohen, 1999; Zryd, 1991) and omitted the unpublished study of Dupuy on Glacier de Saint-Sorlin, mentioned in Vallon et al. (1976), due to lack of details. This table is partly adapted from a similar review carried out in Pettersson et al. (2004). We also omit Pettersson et al. (2004) own study, for being on a polythermal glacier, although some details of it are given in the text.

linear rheology for $w > 0.6$ % is a feature only present for secondary creep. If not, what is the threshold value of w at which that happens?

This question is very important for mountain glaciers, as several studies carried out in temperate glaciers have found $0 \leq w < 3$, well over the 0.6% threshold observed by Adams et al. (2021). It is quite unclear how this water content is spatially spread on a given glacier. Studies on vertical profiles of water content are somewhat contradictory, and while some find depth increasing water content (Vallon et al., 1976; Hubbard et al., 2003; Murray et al., 2007), others report an important decrease in w close to the bed (Lliboutry and Duval, 1985; Murray et al., 2000; Benjumea et al., 2003). More importantly, Lliboutry and Duval (1985) found no particular relationship between depth and water content, and observed highly variable values of w. Another factor to take into account is the differences between water content in the accumulation and the ablation zone of the glacier. Lliboutry (1971) shows higher w in the ablation zone in Aiguille du Midi than in the accumulation zone. Table 2.1 summarizes these studies. Studies carried out with GPR may provide an overestimation of w due to integrating interstitial water and small scale veins that would normally be considered part of the hydrology system, and not as water trapped between ice grains (Murray et al., 2007). Although we are focused on temperate glaciers, it is worth mentioning that Pettersson et al. (2004) reported lateral variations along a transect located on the ablation zone of Störglaciaren, a polythermal glacier. Their conclusion was that the observed spatial variability in w in the ablation zone was a result of different patterns of water content in the accumulation zone, which were then advected downstream. Differences in water input at the surface, strain heating, or even local melting or refreezing due to changes in the melting point of the ice as a result of gradients of hydrostatic pressure could not explain such changes.

Anisotropy

Anisotropic ice refers to ice whose crystals are oriented towards a particular direction, such that there is a direction of favorable deformation. In the case of temperate valley glaciers, it is expected that this process may take place close to the bed, due to fabric development during tertiary creep. Glen's flow law does not apply anymore, and there are several alternative constitutive laws to describe the behaviour of anisotropic ice (Gagliardini et al., 2009). The main difference, from a continuum mechanics point of view, is that since the deformation in an anisotropic material depends on the direction that we consider, creep factor is now a tensor instead of a scalar. To compare the effect of anisotropy with respect to isotropic ice, we can compare the strain rate that are given by Glen's flow law $\dot{\varepsilon}_{ij}^{glen}$ and an anisotropic formulation $\dot{\varepsilon}_{ij}^{ani}$ for the same stress, and creep factor (or analogous factor). In such a case, the enhancement factor due to fabric development can be defined as

$$E_{ij}^{fab} = \frac{\dot{\varepsilon}_{ij}^{ani}}{\dot{\varepsilon}_{ij}^{glen}}.$$

This depends first and foremost on the anisotropic constitutive law, and also on the stress state that we consider (Thorsteinsson, 2001).

Following Thorsteinsson (2001), we see that in the case of basal ice undergoing a mix of simple and pure shear, we can expect that $E_{xz}^{fab} > 1$, as fabric develops with a preferred vertical orientation. The case of ice extension is more complicated. Weak fabric development softens ice along the flow direction, since due to the dependence on effective strains rates (or stress), increased shearing $\dot{\varepsilon}_{xz}$ due to anisotropy enhances the deformation in the x direction, and $E_{xx}^{fab} > 1$. In the case of strong fabric development, we have the opposite effect, vertical compression of the ice is impeded by unfavourable crystal orientation, such that ice becomes stiffer for extension purposes, and $E_{xx}^{fab} < 1$.

In the case of Glacier d'Argentière, ice fabric is not available, although it is indicated in Hantz and Lliboutry (1983) that such measurements were made. However, Vallon et al. (1976) observed in a nearby glacier that while ice had three to four principal directions, thereby being anisotropic, their directions were stable with respect to the stress field. As later Lliboutry and Duval (1985) discussed, 'this supports the currently held belief that glacier ice, despite producing an anisotropic fabric, behaves as an isotropic body during tertiary creep'. Basal ice in Engabreen had no preferred directions (Cohen, 2000), the observed enhancement was rather due to the presence of water around sediments.

2.4 Simplified stress and strain rate in a valley glacier

We illustrate three typical stress states found in glaciers in Figure 2.2, where we also show the type of deviatoric stress tensors that describe those states. The shown example is done for two-dimensional flow, such that $\tau_{yy}, \tau_{xy}, \tau_{yz}$, which relate to the horizontal direction transverse to the flow, are zero. This assumption is typically valid for the center line of symmetric glaciers, and is a reasonable approximation for the stress regime in ice-sheets (Hooke, 2005), but should be taken into account when considering three dimensional flow, or flow close to lateral boundaries (e.g. Raymond, 1971).

Starting from the top, we show that close to the surface the glacier is subjected to a pure-shear state, this is, the deviatoric stress is characterized by compression and extension in the horizontal and vertical directions. For example, if the glacier is close to an icefall we expect strong tractions at the surface (typically indicated by the presence of crevasses, as in Glacier d'Argentière), such that $\tau_{zz} < 0$ and $\tau_{xx} > 0$ (Figure 2.2 shows this case). As we go towards the base, τ_{xx} and τ_{zz} decrease (Hooke, 2005),

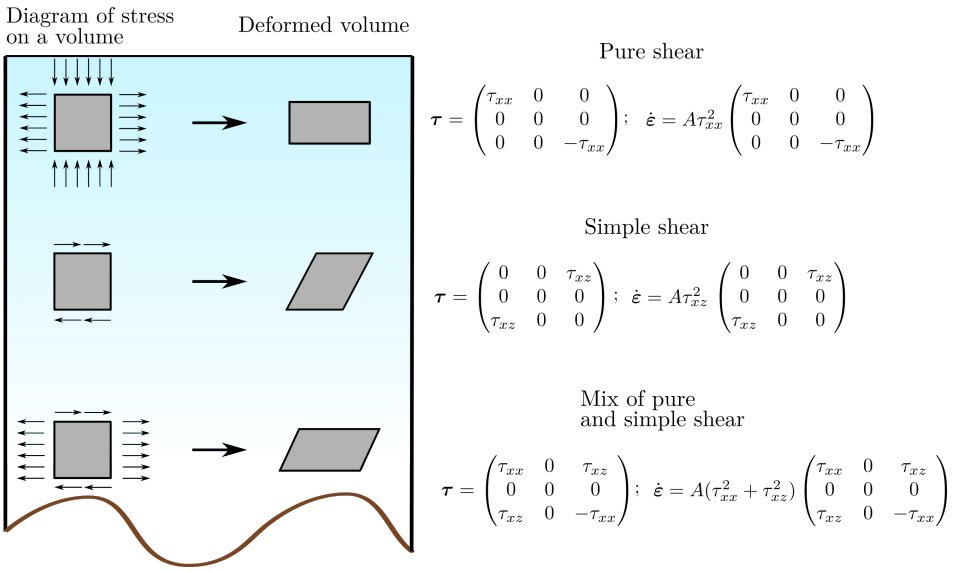

Figure 2.2: Simplified two-dimensional stress states with depth in a glacier. Based on Hooke (2005) for the surface and middle parts of the glacier and in Gudmundsson (1997a) for the basal part. Our observations in Glacier d'Argentière agree with this scheme. More details in the text.

but ice pressure increases, creating a horizontal pressure gradient between the upstream and downstream parts of the glacier, stronger the steeper the surface slope. This depth-increasing horizontal stress causes the stress state to be dominated by pure-shear, thus stress tensor components other than τ_{xz} can be neglected. Finally, immediately close to the bed, there are important stress gradients that develop as the ice deforms around the bed's ostacles, so that the stress state becomes a mix of extension, compression, and shear (Gudmundsson, 1997a), as indicated in Figure 2.2. Large scale models of ice flow tend to abstract this complex near-bed stress state into a large-scaled shear stress τ_b called basal drag. In the next chapter 3, we give more details about basal processes and how to compute the basal drag τ_b from micro-scale stress at the bed.

Chapter 3

The effect of local shear stress on glacier sliding

Except in a few cases, there doesn't seem to be any definite knowledge of just what is under these glaciers.
Johannes Weertman in Interlaken, 1985.

Abstract:

Current theories to describe drag of glaciers over hard beds are formulated on the basis that ice is free of debris and slides without friction over the glacier bed. However, debris at the basal layers and cold ice cause additional resistance to glacier flow. We provide an analytical model of glacier sliding that accounts for the effect of local shear stress at the ice-bed interface in the framework of Weertman (1957), and expand the solution to account for the opening of cavities. This additional drag slows glacier sliding but due to additional strain enhancement of the basal ice, the viscosity of the ice decreases and the basal speed is higher than expected. The inclusion of local shear stress makes the friction law implicit, complicating the identification of scaling parameters from the geometry alone. We further study this problem using a numerical finite element model of glacier sliding over a sinusoidal bed under steady-state conditions. We find that the law with non-zero local shear stress at the base retains the overall form of the friction law with zero local shear stress, such that an appropriate scaling can be obtained. The similarity between a friction law with zero and non-zero local shear stress is convenient for generalising empirical friction laws at the field scale, although it complicates the identification of the effect of local shear stress on glacier flow.

Plain Language Summary

Traditional models of glacier sliding over hard beds consider that all resistance to flow at the base of glaciers, called basal drag, originates from deformation around a rough bed. This assumption is contested by in-situ observations as well as models and laboratory experiments that show that drag between glaciers and their bed due to debris, or other factors, may represent an important portion of the total flow resistance. We provide a new model of glacier sliding that considers this new process. Our model overcomes previous limitations that simplified ice material properties or only considered a low amount of ice to bed drag. On one hand, we can expect more rapid flow, because this additional

drag softens the ice. On the other hand, the mathematical problem of sliding becomes more difficult to solve. The form of the law with and without this additional drag stays relatively the same.

3.1 Introduction

Glaciers with a temperate base have their dynamics strongly controlled by basal sliding (Hooke et al., 1992; Doyle et al., 2018; Maier et al., 2019). Basal sliding speed is typically related to bed stress conditions through a friction law defined at a meso-scale of meters to several tens of meters **?**e.g.,>Weertman1957,Lliboutry1968,Bu At this meso-scale, bed shear stress is envisioned to be primarily set by normal stresses acting on micro-scale (decimetric to metric) obstacles (Weertman, 1957). Stress concentration on these obstacles lowers the effective ice viscosity (Weertman, 1957). For a given obstacle size and under a given stress, the shorter the distance between obstacles, the lower stress concentrations, and thus the lower the basal velocity. For a given distance between obstacles and under a given stress, the rougher the bed, i.e. the higher the obstacles' aspect ratio, the higher the resistance to flow and the lower the basal velocity. As basal water pressure increases, the ice separates from the bed at the lee side of obstacles and opens cavities (Lliboutry, 1968). The opening of these cavities reduces the contact area between the ice and the bed, which reduces the apparent roughness and increases stress concentrations, thus allowing faster basal speed (Lliboutry, 1968; Fowler, 1986; Schoof, 2005; Gagliardini et al., 2007). In the above mentioned conceptualization, perfect sliding is assumed at the ice-bed interface, i.e. local shear stress is considered negligible.

Although typically neglected in existing theories, local shear stress may in reality be non-zero due to solid-type friction acting at the ice-bed interface, for example as a result of debris-bed friction, or due to ice-bed friction if the ice locally lies below the pressure melting point. Debris carried by basal ice have long been observed below mountain glaciers. Consider for instance the deliberation about abrasion and debris-laden ice deformation in the sections *Flow law of basal ice* and *Conditions at the glacier base* of the discussion in **?**, or see the images recorded in a natural cavity under Glacier d'Argentière in France (Figure 3.1), or the samples taken below Engabreen (Norway) (Iverson et al., 2003; Cohen et al., 2005; Zoet et al., 2013). At the latter site, basal force records showed higher than expected levels of bed shear stress that could be due to the extra contribution of debris to bed friction (Iverson et al., 2003; Cohen et al., 2005). Laboratory tests also show that the presence of debris increases bed shear stress (Zoet et al., 2013). Moreover, sliding at subfreezing temperatures could occur in places even under generally temperate base conditions, causing additional drag as observed in laboratory experiments under conditions near the pressure-melting point (McCarthy et al., 2017). Seismic observations of basal stick-slip events emanating from the ice-bed interface provide field evidence that solid-type friction can act across large regions of the bed (Wiens et al., 2008; Zoet et al., 2012; Helmstetter et al., 2015; Roeoesli et al., 2016; Lipovsky et al., 2019) and could be an ubiquitous component of glacier bed friction.

Experimental investigations of the role of solid-type friction on glacier sliding have been mostly devoted to understand the micro-scale mechanisms that control debris-bed friction (e.g. Cohen et al., 2005; Hansen and Zoet, 2019; Thompson et al., 2020) or cold ice-on-rock friction (e.g. Schulson and Duval, 2009; McCarthy et al., 2017). Meanwhile, several theoretical studies considered ice as a Newtonian fluid (Morland, 1976b; Hallet, 1979, 1981), or as a non-Newtonian fluid but under low magnitudes of local shear stress with respect to total bed shear stress (**?**Iverson et al., 2019). Under these simplifying considerations, the ice flow field in the boundary layer above the bed has been assumed to be undisturbed by local shear stress, such that the role of non-zero local shear stress is, essentially, the reduction in basal speed via a reduction in stress concentration. This leaves the following open

Figure 3.1: Cavity under Argentière Glacier, french Alps. The debris cover visible at the base of the glacier varies in density during time. Photograph by Luc Moreau at `http://www.moreauluc.com/`

questions: how is the ice flow disturbed by local shear stress, and how much does that modify the description of meso-scale friction with respect to the other frictional mechanisms?

In this paper, we derive a friction law that considers non-zero local shear stress, non-Newtonian ice rheology and, we believe for the first time, that accounts for the effect local shear stress has on the ice flow field and in particular on the effective viscosity. First, we provide a short background on friction laws and constitutive relationships that may be used to describe local shear stress. Then, we analytically and numerically derive friction laws at the meso-scale that include these descriptions. We demonstrate that common friction laws developed for sliding with zero local shear stress can reasonably well be extended to sliding with non-zero local shear stress providing appropriate scaling changes. Finally, we discuss our findings in the broader context of predicting glacier basal speed.

3.2 Rationale and Methodology

3.2.1 Glacier friction laws

The first proposed and probably most widely applied friction law (e.g. Morlighem et al., 2013; **?**; Larour et al., 2019), has been formulated by Weertman (1957) and takes the following form:

$$\tau_b = A_s^{-1/m} u_b^{1/m}, \tag{3.1}$$

where τ_b is the meso-scale averaged bed shear stress, u_b is the meso-scale averaged basal speed, m is a material exponent, and A_s is the sliding parameter which is dependent on ice rheology and bed geometry. If all the bed shear stress is a result of stress concentration around obstacles (i.e. other processes such as regelation are neglected), we have $m = n$, where n is the exponent of Glen's flow law, typically considered equal to 3 (Cuffey and Paterson, 2010). In the hypothesis of very low roughness r, it is found that A_s scales with $r^{-(n+1)}$ (Fowler, 1979).

Weertman law does not take into account the role of cavities, which is commonly included via the meso-scale averaged effective pressure. For a given average ice pressure $\bar{p}_i$ and subglacial water pressure at open cavities p_c, the averaged effective pressure is $N = \bar{p}_i - p_c$. In our analysis we compare our solution with the phenomenological law proposed by Gagliardini et al. (2007), which was defined based on approximating numerical results as

$$\frac{\tau_b}{N} = C\left(\frac{\chi}{1+\alpha\chi^q}\right)^{1/n}, \text{ with } \chi = \frac{u_b}{(CN)^n A_s},\ \alpha = \frac{(q-1)^{q-1}}{q^q}. \tag{3.2}$$

The parameter $C = \max(\tau_b/N)$ is bounded by the maximum bed slope (Iken, 1981). The exponent parameter $q \geq 1$ depends on the slope severity index, which describes the steepness of the obstacles for a given roughness (Gagliardini et al., 2007). For $q = 1$, τ_b/N increases monotonically (Fowler, 1987; Schoof, 2005) and we obtain a regularized Coulomb friction law (Joughin et al., 2019), while if $q > 1$ the law is double-valued and presents velocity weakening after the basal drag peak $\tau_b = CN$ is reached. At low u_b, Eqn. (3.2) predicts a similar behaviour than Eqn. (3.1). This type of law can be applied to three dimensional sinusoidal beds, as supported by laboratory experiments (Zoet and Iverson, 2015) and numerical simulations (Helanow et al., 2020), although the rate-weakening regime may no longer hold for realistic beds (Helanow et al., 2021).

3.2.2 Strategy for testing the effect of local shear stress on meso-scale bed friction

We first use a simplified analytical model to explore the changes in meso-scale friction with non-zero local shear stress. At this stage, the constitutive law for local shear stress does not require to be described specifically. Instead, we work directly with the meso-scale averaged local shear stress, which we denote τ_f and call solid drag. This first step yields a basis to better understand our findings with more realistic models of sliding, obtained in a second step using numerical simulations. The simplified analytical model developments are presented in section 3.3.1, and discussed in section 3.4.

In a second step, we use a numerical model of glacier sliding with non-zero local shear stress prescribed at the micro-scale. Numerical simulations enable to do so at every point of the ice-bed boundary based on an explicit description of the stress tensor σ and its normal and tangential components σ_{nn} and σ_{nt}, respectively. The numerical results are presented in sections 3.3.2 and 3.3.3, and discussed in section 3.4.

For the numerical simulations, a local law giving the local shear stress needs to be defined. We will test three different laws. The first law is a simplified version of the original description of debris-bed friction provided by Hallet (1981). This framework adopts the initial hypothesis of Weertman that a water film exists and satisfies static equilibrium everywhere at the ice bed interface, i.e. water pressure at the bed p_w equals normal stress $-\sigma_{nn}$ everywhere, such that local effective pressure $N_{loc} = -\sigma_{nn} - p_w$ is zero. In this case solid-type friction at the micro-scale is due to the buoyant weight of the clast and to its velocity perpendicular to the bed, which is non-zero as a result of ice stretching around obstacles and of basal melting. Iverson et al. (2019) showed that, under constant effective pressure, the meso-scale solid drag does not vary significantly with basal speed, since an increase in velocity (and friction force) is compensated by the growth of cavities that reduces the contact area between the ice and the bed. We approximate this result by considering that Hallet (1981) meso-scale solid drag with constant effective pressure is a constant function $\tau_f = c$ and local shear stress is uniform at the ice-bed interface such that it can be described as

$$\sigma_{nt} = c/s, \tag{3.3}$$

where the value of c depends on debris concentration and size, on bed roughness characteristics and effective pressure (Iverson et al., 2019) and s is the portion of the ice in contact with the bed. Note that this is a approximation of a more complex microscopic based model. In our particular implementation,

c is imposed and s is a solution of the problem. We call this approximation the Hallet-like model.

The second law that we consider was proposed by Schweizer and Iken (1992) as 'sandpaper friction'. This model was proposed for higher debris concentration than in Hallet (1981), under the assumption that a very concentrated debris cover would separate the ice from the bed, thus keeping the ice from converging towards the bed. The dependency of local shear stress to the bed normal velocity is thus negligible and local shear stress is controlled by ice pressure. Schweizer and Iken (1992) do not consider the role of water pressure, which means that water at the base must be either absent or not surrounding the clast in contact with the bed. In this case, local shear stress may be expressed through Coulomb friction at the ice-bed interface as

$$\sigma_{nt} = -\mu\sigma_{nn}. \tag{3.4}$$

We note that this Coulomb friction law is also relevant for modeling local shear stress for subtemperate ice (McCarthy et al., 2017). We later refer to this model as the sandpaper model.

In the third law, we consider the case for which the initial hypothesis of Weertman of a water film existing and satisfying static equilibrium everywhere at the ice bed interface is no longer satisfied, so that $N_{loc} = -\sigma_{nn} - p_w > 0$. This is for example expected if a nearby cavity or channel lowers the water pressure below that at static equilibrium around the debris, in which case a dependency on the local effective pressure N_{loc} must be accounted for and σ_{nt} at the ice-bed interface can be expressed as

$$\sigma_{nt} = \mu N_{loc}. \tag{3.5}$$

Later we refer to this law as the effective-pressure-driven Coulomb law, and assume a uniform water pressure everywhere equal to that in cavities.

3.2.3 Modeling setup

We consider a two-dimensional infinite glacier of average thickness $H + h_i$ and surface slope θ contained in the $x-z$ plane and flowing over a periodic bed of height $z = b(x)$ and period L (see Figure 3.2 and Table 1 for the notation definition). Normal and tangential unit vectors at the domain boundary are denoted by $\mathbf{n}$ and $\mathbf{t}$, respectively. The bottom boundary of the ice is given by the periodic function $z = h(x) \geq b(x)$. We study a subdomain of the glacier, limited in width to L and in height to H such that it defines four boundaries, the top $\partial\Omega_1$, the bottom $\partial\Omega_3$ (subdivided into the cavitated interface $\partial\Omega_{3C}$ and the uncavitated interface $\partial\Omega_{3U}$) and the left and right sides $\partial\Omega_2$ and $\partial\Omega_4$, respectively, see Figure 3.2. Above H, we assume that the flow field is undisturbed by the irregularities of the bed, such that at $z = H$ the stress and velocity fields are uniform. Domain length can be subdivided into two parts, $L = L_C + L_U$, each corresponding to $\partial\Omega_{3C}$ and $\partial\Omega_{3U}$ respectively. In this domain, the Stokes flow equations (momentum and mass conservation) are solved for the ice velocity $\mathbf{u}(x, z)$ and pressure $p(x, z)$:

$$\nabla \cdot \boldsymbol{\sigma} = \mathbf{0}, \nabla \cdot \mathbf{u} = 0. \tag{3.6}$$

Note that gravitational force is neglected in our domain Ω and ice is assumed incompressible. Periodic boundary conditions are applied on left and right sides, far field conditions are applied on the top boundary and correspond to overburden ice pressure of the ice column of height h_i over the modelled domain, $\sigma_{nn} = \bar{p}_i = -\rho_i g h_i \cos(\theta)$, and uniform horizontal velocity u_i. If open, the cavity is supposed to

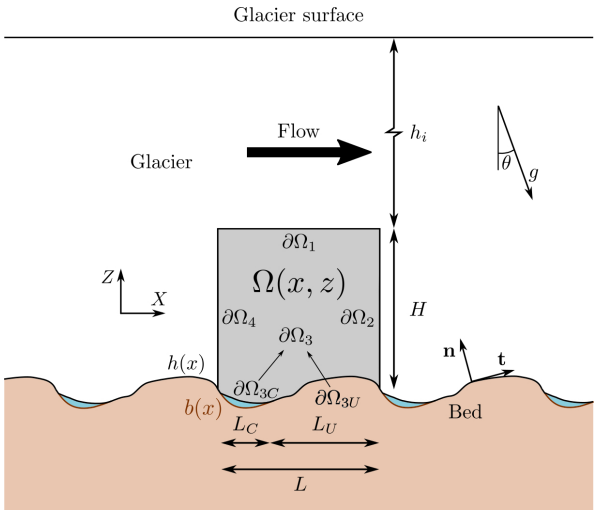

Figure 3.2: An example of a two-dimensional infinite glacier and the domain of interest Ω (in gray). The example shows a vaguely sinusoidal bed in brown with water-filled cavities in blue.

undergone a uniform water pressure p_c. At the uncavitated interface the conditions are impenetrability, $\mathbf{u}\cdot\mathbf{n} = 0$ and imposed shear stresses σ_{nt} given by either Eqn. (3.3), (3.4) or (3.5). At the cavitated interface we impose that normal stress is equal to the cavity water pressure $\sigma_{nn} = -p_c$, and tangential stress is zero $\sigma_{nt} = 0$.

We can perform the balance of vertical and horizontal forces over the bottom boundary to gain some insights about the friction law with non-zero local shear stress. We use the same procedure as that developed by Schoof (2005), considering the convention of negative stresses for compression, and normal and tangential vectors $\mathbf{n}$ and $\mathbf{t}$ with respect to the interface oriented as drawn in Figure 3.2.

Conservation of momentum dictates that basal drag and overburden pressure are balanced by reaction forces at the bottom boundary $\partial\Omega_3$

$$(-\tau_b, \bar{p}_i) = -\frac{1}{L}\int_{\partial\Omega_3} \boldsymbol{\sigma}\mathbf{n} ds. \tag{3.7}$$

Projecting into x and z, separating between horizontal and vertical directions and considering that $\sigma_{nt} = 0$ on $\partial\Omega_{3C}$ gives

$$\tau_b = \frac{1}{L}\int_L h'(-\sigma_{nn})dx + \frac{1}{L}\int_{L_U} \sigma_{nt}\, dx = \frac{1}{L}\int_L h'(-\sigma_{nn} - p_c)dx + \frac{1}{L}\int_{L_U} \sigma_{nt}\, dx \tag{3.8a}$$

$$\bar{p}_i = \frac{1}{L}\int_L -\sigma_{nn} dx - \frac{1}{L}\int_{L_U} h'\sigma_{nt}\, dx, \tag{3.8b}$$

with $h'(x)$ the local slope of the ice bottom boundary and $N = 1/L\int_L (-\sigma_{nn} - p_c)\, dx$. Adding p_c to the first integral will help later when studying the upper bound of the basal drag, and does not change the force balance because the integral of $h'p_c$ over the bed vanishes due to the periodicity of the bed. The first equation gives the balance of horizontal force at the bed, with basal drag divided into the viscous drag τ_u, defined as the meso-scale averaged local normal stress at the ice-bed interface, and the solid drag τ_f, defined as the meso-scale averaged local shear stress at the ice-bed interface,

$$\tau_u = \frac{1}{L}\int_L h'(-\sigma_{nn} - p_c)\, dx = \frac{1}{L}\int_L h' N dx, \text{ and } \tau_f = \frac{1}{L}\int_{L_U} \sigma_{nt}\, dx, \tag{3.9}$$

such that $\tau_b = \tau_u + \tau_f$. The horizontal force balance allows us to introduce the solid drag ratio T, a reduced variable that will be used in the following section and is defined as

$$T = \frac{\tau_f}{\tau_b},\ 0 \leq T \leq 1. \tag{3.10}$$

Note that $T = 0$ if sliding with zero local shear stress, i.e. $\tau_f = 0$.

We can also use the force balance to find the basal drag upper bound. Viscous drag is bounded by the slope and the effective pressure (Iken, 1981), so that from the first integral of Eqn. (3.8a) we can define $\tau_u \leq \sup(h')N$. This allows us to define a $C = \max(\tau_u/N) \leq \sup(h')$. Adding τ_f/N to both sides of the inequality we find a new bound in case of non-zero local shear stress, noted C_f, and defined as $C_f = \max(\tau_b/N)$ Substituting Eqn. (3.8a) into $C_f = \max(\tau_b/N)$ gives,

$$C_f \leq \sup(h'(x)) + \tau_f/N. \tag{3.11}$$

In the case of the Hallet-like model (Eqn. (3.3), note that the approach is for sliding under constant effective pressure), we have

$$C_f \leq \sup(h'(x)) + c/N. \tag{3.12}$$

For the sandpaper model, we combine Eqn. (3.4) with Eqn. (3.8a) to obtain

$$\begin{aligned}\tau_b &= \frac{1}{L}\int_L h' N dx + \frac{1}{L}\int_L -\mu(\sigma_{nn} + p_c - p_c) dx = \frac{1}{L}\int_L h' N + \mu N dx + \frac{1}{L}\int_{L_C} \mu p_c dx \\ &= \frac{1}{L}\int_L (h' N + \mu N)\, dx + \mu p_c s,\end{aligned}$$

with $s = L_C/L$ the portion of the bed not drowned by the cavity. If we now substitute the expression we just derived into Eqn. (3.8a), rewrite p_c as $\bar{p}_i - N$ and reorder some terms, we obtain the final expression of C_f for the sandpaper model,

$$C_f \leq \sup(h'(x)) + \mu s + \mu(1-s)\bar{p}_i/N. \tag{3.13}$$

In the case of effective-pressure-driven Coulomb law (Eqn. (3.5)) this is

$$C_f \leq \sup(h'(x)) + \mu, \tag{3.14}$$

as suggested by Schoof (2005).

The presence of local shear stress strengthens the bed, as it can support higher basal stress, i.e. $C_f \geq C$. Indeed, we expect solid drag to take up some of the force that would otherwise be supported by viscous drag. For a given driving stress this would result in slower basal speed compared to the scenario with zero local shear stress. In the following section we solve the flow of ice over an undulated bedrock assuming non-zero local shear stress at the interface. We provide an analytical solution over a simplified tombstone bed and a numerical solution over a sinusoidal bed.

For the analytical solution, we consider the 'tombstone model' similar to the bed of Weertman (1957), in which the bed $b(x)$ is a rectangular function made of protuberances of side $2a$ separated be-

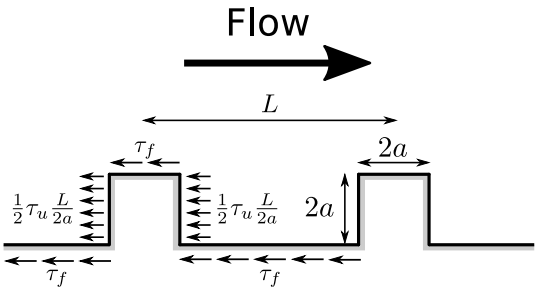

Figure 3.3: Continuous version of the tombstone model with the considered stresses, no cavity.

tween each other by a distance L, with roughness $r = a/L$ (see Figure 3.3). Considering this geometry allows only an approximate solution, albeit simplifies the problem such that it is tractable analytically. We further assume that i) viscous drag operates on the vertical sides of the bumps, and solid drag on the horizontal sides, and ii) the stress and strain rate fields are uniform over the domain of study.

To obtain the numerical solution we use the finite element model Elmer/Ice (Gagliardini et al., 2013). The numerical domain is a regular mesh of bi-linear quadrilateral elements, vertically refined towards the bottom boundary, with $L = H = 10$m. The bed height function is a single wave function with amplitude a,

$$b(x) = a \sin\left(\frac{2\pi x}{L}\right). \tag{3.15}$$

Note that since we keep the domain length fixed, we modify bed roughness by changing a. The major changes to the numerical implementation with respect to Gagliardini et al. (2007) are i) cavity opening, which now solves the corresponding contact problem between ice and bed using the residual of the Stokes equation (Gagliardini et al., 2013), ii) improved mesh resolution and iii) the already discussed local shear stress laws. Otherwise specified, the friction law is obtained by looking at steady state solutions for cavity water pressure p_c between 0 and $0.8p_i$ with increments of $0.01p_i$, with $p_i = 1.77$ MPa (the pressure of 200 m of ice) and top velocity $u_i = 150$ m a^{-1}, such that the solutions for square obstacles and for a sinusoidal bed are comparable. Spatially averaged variables u_b, τ_b, τ_f and N are then recovered from the velocity vector and the stress tensor.

3.3 Results

3.3.1 Analytical friction law

For the analytical solution, only the case without cavity is presented in the main text, the complete solution including the formation of cavities being given in 3.6. We use $u_b(T = 0)$ for basal speed in a zero local shear stress scenario and $u_b(T)$ for the basal speed when there is non-zero local shear stress at the ice-bed interface.

Assuming two-dimensional flow over square obstacles of side $2a$ and $r = a/L$, deviatoric stresses τ_{xx}, τ_{xz} and effective deviatoric stress τ_E can be approximated as (Cuffey and Paterson, 2010)

$$\tau_{xx} = \frac{1}{2}\tau_u \frac{L}{2a},\ \tau_{zz} = -\tau_{xx},\ \tau_{yy} = 0,$$
$$\tau_{xy} = 0,\ \tau_{xz} = \tau_f,\ \tau_{yz} = 0, \tag{3.16}$$
$$\tau_E = (\frac{1}{16}\tau_u^2 \frac{L^2}{a^2} + \tau_f^2)^{\frac{1}{2}}.$$

The constitutive law for ice is

$$\dot{\varepsilon}_{ij} = A\tau_E^{n-1}\tau_{ij}, \tag{3.17}$$

where creep parameter A is considered constant. Combining Eqn. (3.16) with Eqn. (3.17) gives the following strain rates:

$$\dot{\varepsilon}_{xx} = A\left(\frac{1}{16}\tau_u^2 \frac{L^2}{a^2} + \tau_f^2\right)^{\frac{n-1}{2}} \frac{1}{4}\tau_u \frac{L}{a}, \text{ and } \dot{\varepsilon}_{xz} = A\left(\frac{1}{16}\tau_u^2 \frac{L^2}{a^2} + \tau_f^2\right)^{\frac{n-1}{2}} \tau_f, \tag{3.18}$$

where $\dot{\varepsilon}_{xx}$ is the extension strain rate, and $\dot{\varepsilon}_{xz}$ the shear strain rate, both dependent on τ_u and τ_f. The basal speed is evaluated as the integral of the horizontal velocity gradient over a bump of size $2a$, at a height l from the bed. Assuming uniform strain rates, and $dw/dx = 0$, this is equivalent to

$$u_b = \int_{2a} \frac{du}{dx}dx + \int_l \frac{du}{dz}dz = \dot{\varepsilon}_{xx}2a + 2\dot{\varepsilon}_{xz}l. \tag{3.19}$$

In particular, if we take $l = 2a$ (the distance between the highest and the lowest points of the bed) and rewrite Eqn. (3.18) to include the roughness $r = a/L$ we get

$$u_b = A\left(\frac{1}{16}\tau_u^2 \frac{1}{r^2} + \tau_f^2\right)^{\frac{n-1}{2}} \frac{1}{4}\tau_u \frac{1}{r}2a + A\left(\frac{1}{16}\tau_u^2 \frac{1}{r^2} + \tau_f^2\right)^{\frac{n-1}{2}} 4a\tau_f. \tag{3.20}$$

Substituting solid drag ratio $T = \tau_f/\tau_b$ into Eqn. (3.20) and factoring out common terms gives the basal speed

$$u_b = A\left(\frac{1}{16}(1-T)^2 \frac{1}{r^2} + T^2\right)^{\frac{n-1}{2}} \left(\frac{1}{4}(1-T)\frac{1}{r} + 2T\right)2a\tau_b^n. \tag{3.21}$$

One can note that Weertman's solution is recovered using $T = 0$, in which case we have

$$u_b(T=0) = \frac{1}{4^n}A\left(\frac{1}{r}\right)^n 2a\tau_b^n. \tag{3.22}$$

To proceed further, we investigate the effect of solid drag on the flow speed with respect to Weertman's solution through evaluating the ratio $(u_b(T)/\tau_b^n)/(u_b(T=0)/\tau_b^n)$, equivalent to the ratio $u_b(T)/u_b(T=0)$, which takes the form

$$u_b(T)/u_b(T=0) = \underbrace{(1-T)^{\frac{2n}{n-1}}}_{\text{pure shear}} + \underbrace{16r^2(1-T)^{\frac{2}{n-1}}T^2 + 8r(1-T)^2T^{\frac{2}{n-1}}}_{\text{strain enhancement}} + \underbrace{128r^3T^{\frac{2n}{n-1}}}_{\text{simple shear}}. \tag{3.23}$$

The first term corresponds to the reduction of basal speed caused by a decrease in pure shear deformation if drag is only due to creep around obstacles. This term is a decreasing function of T, while the other terms mitigate this decrease in basal speed. The second and third terms appear due to the non-linearity of Eqn. (3.17), i.e. ice deformation depends on all stress components, such that shearing the ice will enhance ice deformation by extensional strain rates. The fourth term is the deformation

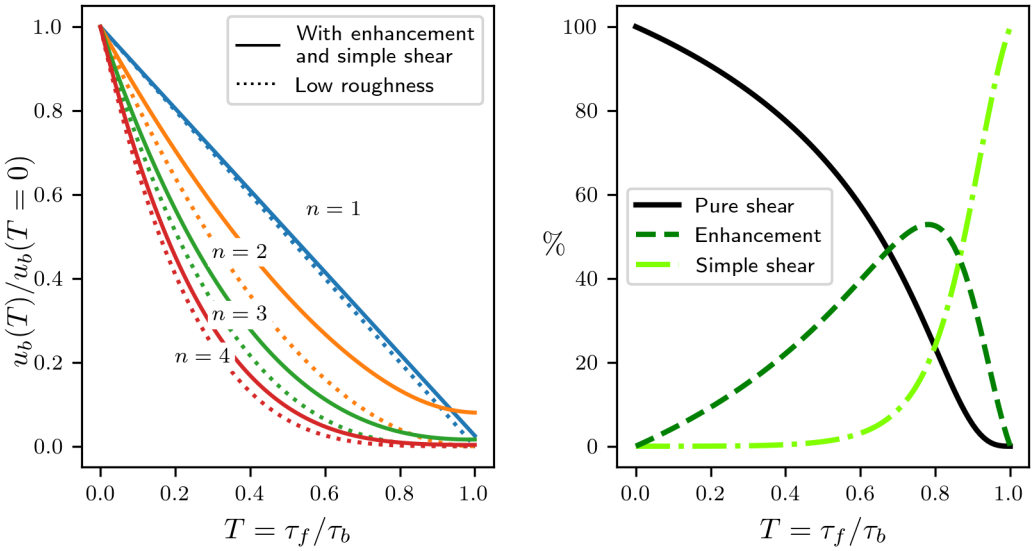

Figure 3.4: Decrease in basal speed as a function of the relative solid drag $T = \tau_f/\tau_b$ for different values of n. Panel (a) shows solutions of Eqn. (3.24) (the $n = 1$ lines) and Eqn. (3.21) ($n = 2$, $n = 3$, $n = 4$), using the full expression (continuous lines) and the low roughness approximation (dotted lines). Panel (b) shows the relative contribution of each term of Eqn. (3.21) for $n = 3$.

of ice subjected to simple shear only.

If the roughness is very low, Eqn. (3.23) simplifies to $\lim_{r\to 0} u_b(T)/u_b(T=0) = (1-T)^{2n/(n-1)}$, as proposed by **?**. Note that, if $r = 0$, there is no resistance due to creep around bumps and we have $\tau_u = 0$, and Eqn. (3.21) does not hold. The specific form of τ_b will then be inherited from the form of the local shear stress law , i.e., if we assume that τ_f is given by effective-pressure-driven Coulomb friction, we have $\tau_b = \tau_f = \mu N$.

In the case of Newtonian ice, the flow exponent (Eqn. (3.17)) is $n = 1$, and to avoid indeterminate exponents in Eqn. (3.23) we have to derive the expression from Eqn. (3.21), obtaining

$$u_b(T)/u_b(T=0) = (1-T) + 8rT. \tag{3.24}$$

For very low roughness it simplifies to $\lim_{r\to 0} u_b(T)/u_b(T=0) = 1-T$.

Figure 3.4 (a), shows the expected decrease in basal speed when we introduce local shear stress for $n = 1$, $n = 2$, $n = 3$ and $n = 4$, when we consider the full expression (solid lines, Eqn. (3.21) and (3.24)) or the low roughness approximations of Eqn. (3.21) and (3.24), (dotted lines). On the right panel, we show the relative contribution of the terms of Eqn. (3.21) to the total decrease in basal speed for $n = 3$. Except for high values of $T = \tau_f/\tau_b$, the low roughness expression is a good approximation of the decrease in basal speed with T. For example, if $T = 0.5$, meaning half the basal drag is given by solid drag, the low roughness approximation underestimates the basal speed by 30%. Indeed, this approximation, given by the *pure shear* term of Eqn. (3.21), and represented by the solid line on Figure 3.4 (b), dominates the decrease in basal speed until roughly $T = 0.7$.

We can invert Eqn. (3.21) to obtain a friction law,

$$\tau_b = \left[A\left(\frac{1}{16}(1-T)^2\frac{1}{r^2} + T^2\right)^{\frac{n-1}{2}}\left(\frac{1}{4}(1-T)\frac{1}{r} + 2T\right)2a\right]^{-1/n} u_b^{1/n}. \tag{3.25}$$

Note that this expression is non-linear, since $\tau_b = f(u_b, N, T(\tau_b))$, and solving it requires knowledge of

the form of $T(\tau_b)$. Moreover, in the case of no local shear stress, Eqn. (3.1), τ_b and $u_b^{1/n}$ were linked by a sliding parameter, $A_s^{-1/n}$. This is no longer the case when local shear stress is non-zero, in which case $\tau_b/u_b^{1/n}$ is a function of $T(\tau_b)$, such that what was a constant parameter is now a variable. Moreover, the dependency in T is stronger for lower roughness, as r appears in the denominator in Eqn. (3.25). We illustrate this point in Figure S1, where we plot the sensitivity of u_b/τ_b^n to T for several values of r, i.e. $d(u_b/\tau_b^n)/d(T)$. If $T = \tau_f/\tau_b$ is constant then we can define a scaling parameter $A_f^{\mathrm{Tconst}} = u_b/\tau_b^n$, equivalent to

$$A_f^{\mathrm{Tconst}} = A_s\left((1-T)^{\frac{2n}{n-1}} + 16r^2(1-T)^{\frac{2}{n-1}}T^2 + 8r(1-T)^2T^{\frac{2}{n-1}} + 128r^3T^{\frac{2n}{n-1}}\right). \tag{3.26}$$

With A_s the same as in Eqn. (3.1). We show a friction law with constant $T = \tau_f/\tau_b$, scaled with A_f^{Tconst} in the examples given in 3.6.

3.3.2 Numerical friction law with effective-pressure-driven Coulomb local shear stress

Here we present the numerical simulations over sinusoidal beds and effective-pressure-driven Coulomb local shear stress at the base using the model setup presented at the end of section 3.2.3. The friction laws for $r = 0.05$, using scaling parameters C and A_s, are shown in Figure 3.5 (a, b), while the laws for $r = 0.03$ and $r = 0.08$ are given in the supporting information, Figures S2 and S3. C and A_s are obtained for each roughness r based on the simulation with $\mu = 0$ as explained in Gagliardini et al. (2007). The friction laws when scaled with C and A_s have the same overall shape, characterized by an initial rate-strengthening regime, with increasing curvature until a peak in $(\tau_b/CN)^3$ is reached and a transition to the rate-weakening regime. The larger the friction parameter μ, the higher the peak value and the steeper the curve in the rate-strengthening phase. The peak in bed shear stress being located higher for higher μ is a consequence of higher upper bound of τ_b, as shown in Eqn. (3.14). Likewise, the origin behind the change in the slope of the rate-strengthening regime can be found in Eqn. (3.23). Under a given basal drag, the higher T is, the slower the glacier flows and the higher the ratio τ_b/u_b, thus the slope of the curve in the rate-strengthening regime increases.

We more quantitatively investigate the extent to which the different friction laws share the same shape by scaling each of these laws with the parameters C_f^{num} and A_f^{num}, analogous to C and A_s in Eqn. (3.2), except they now account for the effect of local shear (Figure 3.5 (c, d)). To compute these parameters we impose that the peak of the laws coincide in the scaled space. C_f^{num} is calculated as $C_f^{\mathrm{num}} = \max(\tau_b/N)$. A_f^{num} is calculated such that $u_b/(A_f^{\mathrm{num}}(CN)^3) = \chi_M$, with χ_M a constant. We fix the value of χ_M by using as reference point the peak of the friction law in Eqn. (3.2) that matches well the friction law with zero local shear stress. We found that $\chi_M = q/(q-1)$, with $q = 1.8$ gives an appropriate collapse of all the curves. The quality of this scaling worsens for lower r, as can be seen in the $r = 0.03$ curves given in Figure S2.

Focusing on the values of the scaling parameters, we compare C_f^{num} with a (semi)theoretical value $C_f^{\mathrm{the}} = 2k\pi r + \mu$, computed as a combination of Eqn. (3.14) with the expression $C = 0.84\ 2\pi r$ suggested by Gagliardini et al. (2007) for sinusoidal beds. We find that the value of k that best fits C_f^{num} is $k = 0.72$, 12% lower than the value 0.84 found by Gagliardini et al. (2007). The comparison between C_f^{the} and C_f^{num} is shown in the left panel of Figure S4. While the overall shape of the friction law is conserved, as seen in panel (c) of Figure 3.5, the detailed view in panel (d) shows that the different laws do not all collide into the expected Weertman type behaviour (black line). Moreover, the higher μ, the further from the Weertman line they are. This is a direct consequence of using a constant A_f^{num} when T

evolves, which limits the effectiveness of scaling the law by a constant A_f^{num}, specially for lower values of r. In the absence of an explicit theoretical expression for A_f in the case of variable T, we refrain from defining A_f^{the} for these experiments. We plot the values of the scaling parameters normalised by the parameters with no local shear stress, C_f^{num}/C and A_f^{num}/A_s, as functions of μ/r in the supporting information, Figure S4.

3.3.3 Comparison between the three solid-type friction laws

In this section, we test whether the above presented results using the effective-pressure-driven Coulomb model also hold under other micro-scale descriptions of solid-type friction such as the Hallet-like (Eqn. (3.3)) and sandpaper (Eqn. (3.4)) models. For that, we use a sinusoidal bedrock with a given roughness $r = 0.05$. Since the Hallet-like model assumes constant effective pressure, we change the top boundary conditions from varying effective pressure and constant upper horizontal velocity to constant effective pressure at ≈ 700 kPa (40% of the initial effective pressure used in the other tests) and varying upper velocity u_i from 20 to 400 ma^{-1}. The Hallet-like model is run at fixed solid drag $\tau_f = 50$ kPa in order to lie within the range of values obtained by Iverson et al. (2019, Figure 8) for a sinusoidal bed of roughness $r = 0.05$ with debris of radius 60 mm and an effective pressure of $N = 500$ kPa (note that the roughness defined in Iverson et al. (2019) is two times the roughness defined here). The sandpaper model is implemented with a friction parameter $\mu = 0.05$, with the same top boundary conditions as the effective-pressure-driven Coulomb tests explained in section 3.2.3.

As shown in Figure 3.6, both the Hallet-like and sandpaper models yield similar predictions as those with the effective-pressure-driven Coulomb model (Eqn. 3.5) presented in the previous section. The same scaling using A_f^{num} and C_f^{num} is used here to compare the three different models of local shear stress.

The values of $C_f^{\text{num}} = \max(\tau_b/N)$ are found to match quite well the theoretical values of C_f^{the}, which as in the previous section result from combining $C = k2\pi r$ proposed by Gagliardini et al. (2007) (with the $k = 0.72$ found in our study) with the different expressions for C_f given in Eqn. (3.12) to (3.14). Indeed, for the Hallet-like model with $\tau_f = 50$ kPa, the numerical value $C_f^{\text{num}} = 0.320$ for $N = 700$ kPa is also not far away from the expected theoretical one $C_f^{\text{the}} = 0.72 \times 2\pi r + \tau_f/N = 0.298$ obtained from Eqn. (3.12). For the sandpaper model, the numerical value $C_f^{\text{num}} = 0.331$, reached for an uncavitated bed portion of $s = 0.693$ and an effective pressure $N = 634$ kPa, is very close to $C_f^{\text{the}} = 0.72 \times 2\pi r + \mu s + \mu(1-s)p_i/N = 0.312$ given by Eqn. (3.13).

3.4 Discussion

We demonstrate that meso-scale friction over sinusoidal beds under non-zero local shear stress exhibits similar characteristics to laws previously introduced with zero local shear stress, which are, mainly, softening during the rate-strengthening behavior due to the onset of cavities, a maximum attainable basal drag for a given effective pressure, and rate-weakening regime after such maximum drag is attained. The new element introduced in the friction law is the influence of local shear stress on stress concentrations and thus ice viscosity, which was ignored in previous models, although it has a relatively low impact on the overall result. Added local shear stress lowers sliding speed, although this decrease is mitigated by an increase in the effective deviatoric stress, which decreases the effective viscosity. This strain enhancement effect is represented by the T dependent terms in the (implicit) friction law given in Eqn. (3.21). This complicates the use of scaling parameters that generalize the fric-

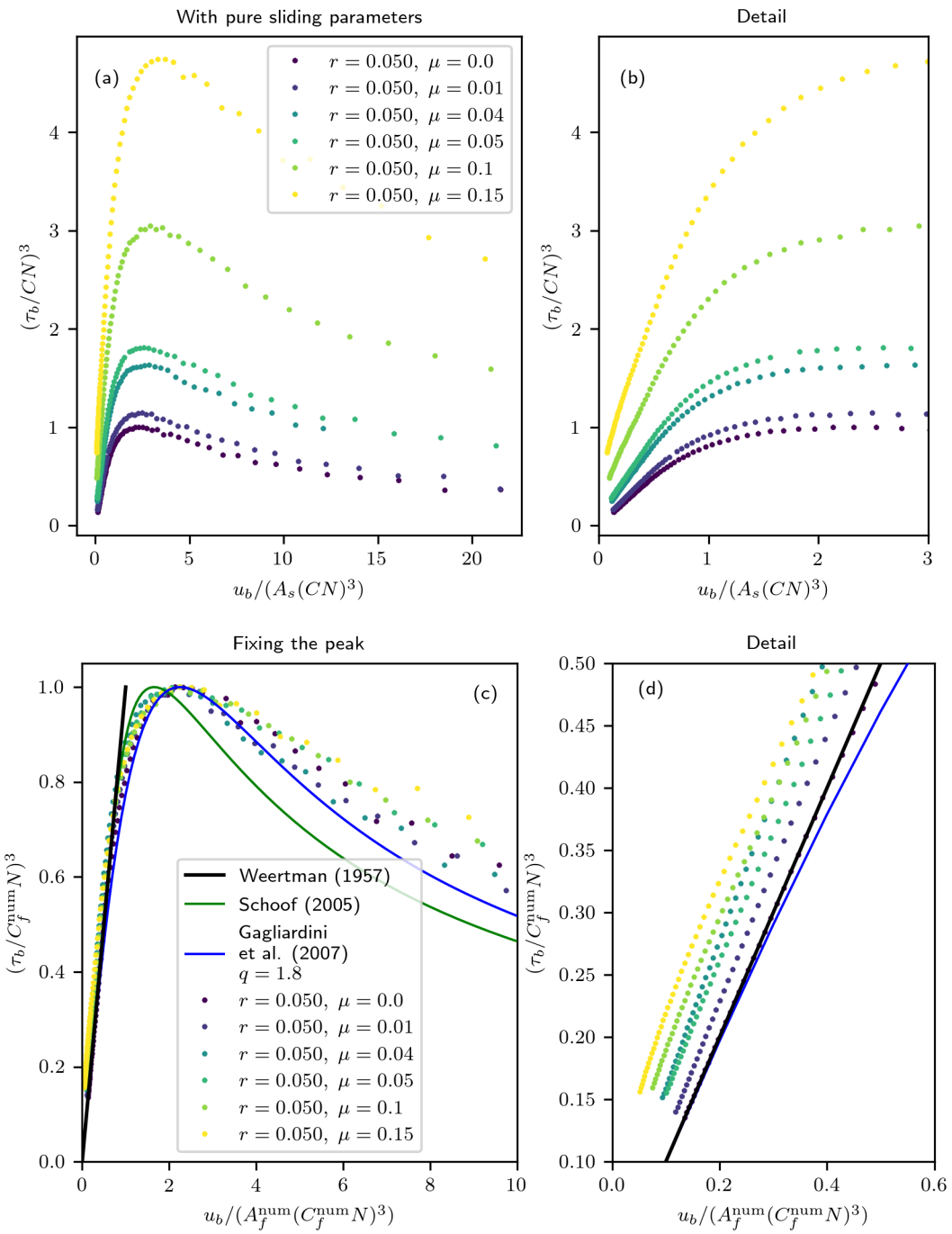

Figure 3.5: Comparison of the friction laws obtained numerically for a sinusoidal bed of roughness $r = 0.05$ and different values of μ, using ((a) and (b)) C and A_s as scaling parameters and ((c) and (d)) C_f^{num} and A_f^{num} as scaling parameters. Panels (b) and (d) are limited to the rate-strengthening part of the curves shown in (a) and (c), respectively. Symbols represent the numerical results and the curves show the Weertman (Eqn. (3.1)), Schoof (2005) and Gagliardini et al. (2007) (Eqn. (3.2)) solutions.

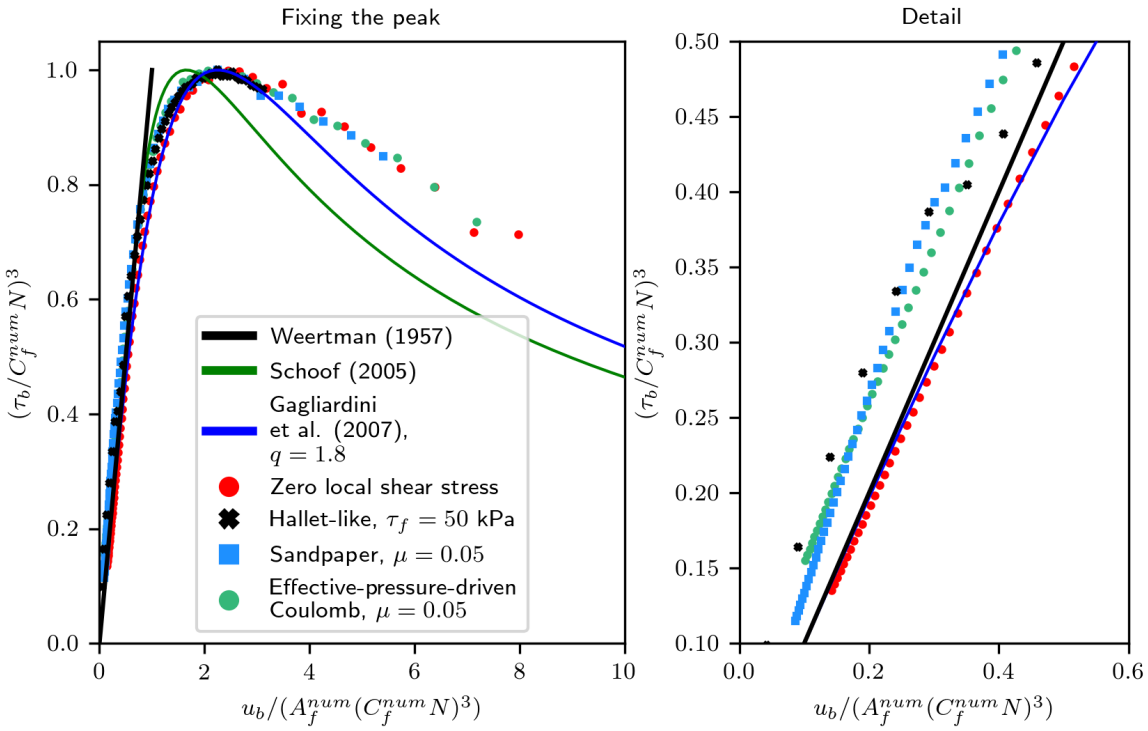

Figure 3.6: Numerical friction laws over a sinusoidal bed of $r = 0.05$ using three different local shear stress laws, constant solid drag (also called Hallet-like, Eqn. (3.3)) with $\tau_f = 50$ kPa, Sandpaper (Eqn. (3.4)) with $\mu = 0.05$, and effective-pressure-driven Coulomb (Eqn. (3.5)) with $\mu = 0.05$. Symbols represent the numerical results and the curves show the Weertman (Eqn. (3.1)), Schoof (2005) and Gagliardini et al. (2007) (Eqn. (3.2)) solutions.

tion law for a variety of boundary conditions. In the case of sinusoidal beds, we see that for our tested roughness and local shear stress laws, we can exploit that the form of the law is similar to sliding with no local shear stress to obtain reasonable scaling parameters by imposing that all friction laws attain the peak at the same point $(u_b/(A_f^{\mathrm{num}}(C_f^{\mathrm{num}}N)^3) = q/(q-1)$ (with $q = 1.8$) and $\tau_b/(C_f^{\mathrm{num}}N) = 1$. The quality of the scaling becomes worse for high μ and low r, as a result of the sensitivity of u_b/τ_b^n to $T = \mu N/\tau_b$ and r, see Figure S1. Our results show that determining A_f^{num} requires solving the friction law until the peak is reached. This has several important implications. Firstly, it requires knowledge of the form of local shear stress and its relationship with other variables (e.g. glacier basal speed, effective pressure), since the friction law has to be solved. Secondly, it requires that the weakening regime is not suppressed when sliding with local shear stress, as our results show, in accordance with those of Iverson et al. (2019) which were obtained using Hallet friction and neglecting the enhancement effect. The weakening regime can only be suppressed if local shear stress increases fast enough with increasing sliding, as shown in 3.6.

How accurate is the value of the computed C_f^{num} and A_f^{num} will depend on the resolution of the friction law around the peak, i.e. on the number of points used in each numerical friction law. Since we compute C_f^{num} and A_f^{num} by looking at the point with the highest τ_b/N, too few points will mean that the numerically retrieved peak is far away from the expected position. It does not pose a problem in our case, since the relatively cheap computational cost of the numerical scheme (2D) means we compute one point of the simulation for each 1% increment of p_c, obtaining a satisfactory number of points around the peak. It could, however, pose a problem if performing a similar analysis on more complex configurations, such as three dimensional geometries.

The similarity of the friction laws with zero and with non-zero local shear stress appears to be

valid regardless of the specific constitutive law used to describe local shear stress. We further explore the validity of this assumption in our comparison between models of local shear stress, as shown for different regimes of the friction law in Figures S5, S6 and S7 of the supplementary material. The biggest differences in local shear stress distribution across models happens in the no-cavity regime, where the pressure-based laws vary by a factor of $\pm 100\%$ with respect to the Hallet-like implementation. However, in Hallet (1981) local shear stress comes from the weight of the particle and the stretching rate of the ice, which we can expect to concentrate at the upslope portions of glacier beds. This is already the case for a pressure based shear stress model, thus increasing even more the similarities between models for the no-cavity regime, and therefore the convenience of simple, straight-forward models of pressure-based friction for studying how τ_f affects sliding.

We have seen that the forms of a friction law with zero solid drag and a friction law with solid drag are very similar, complicating the identification of the presence or not of solid friction based on real data (e.g. Gimbert et al., 2021b). A possible solution would be the comparison of field estimates of A_s and C with those obtained with accurate flow simulation over detailed three-dimensional glacier beds (Helanow et al., 2021). Large discrepancies between them could indicate the presence of non-zero local shear stress. This comparison would require accurate knowledge of bed geometry, which is usually only possible in deglaciated areas, as well as good estimates of basal drag acting upon the studied zone, so it is not a feasible option for the large majority glaciers.

Our study has been formulated under steady-state conditions and the results may differ drastically under non-steady conditions, since solid drag likely has a shorter response time than viscous drag. Similarly, we don't expect that the presently established conclusions applies to the case of highly concentrated debris at the glacier base that would make the ice-debris mixture behave differently than a viscous fluid. The validity of our result should be also tested for other geometries, both two and three dimensionals. For three dimensional beds, we can expect that lateral variations in bed topography will restrict high stresses to a smaller bed area (Helanow et al., 2020), increasing the strain enhancement effect with respect to two dimensional beds.

3.5 Conclusions

In this study, we developed a new analytical model of glacier sliding over rough hard beds with local shear stress (such as debris-bed friction) that includes the effects of local shear stress on viscosity. The influence that non-zero local shear stress has on sliding can be included in the friction law by adding terms to the friction law based on bed geometry and average solid-type drag. We show that additional strain enhancement will result in faster flow than could be expected, if the effects of local shear stress on friction are neglected. The effect of local shear stress on ice viscosity render the friction law implicit, further complicating the identification of scaling parameters from a purely physical point of view. Nevertheless this complication, our findings on the form of the friction law are coherent with previous studies that assumed low quantities of ice to bed friction. Ice creep around obstacles and cavities will still be representative of the sliding process, unless i) there is rate increasing solid drag and ii) it is strong enough to compensate the rate-weakening viscous drag. As a result, the friction law of glaciers sliding with non-zero local shear stress at the base will retain the same form as the law developed for sliding with no local shear stress, including the rate-weakening regime. We can exploit this fact to use laws developed for sliding with zero local shear stress to represent sliding with non-zero local shear stress, although this can fail at some circumstances, such as low roughness or high degrees of solid drag. Further work has to be carried out to confirm how the interplay between local

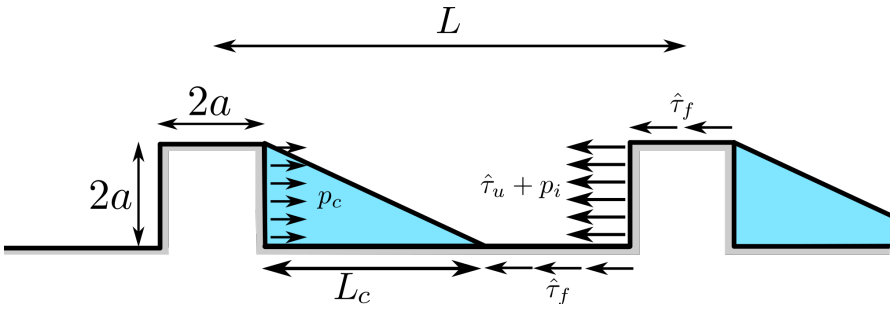

Figure 3.7: Conceptual model of cavity opening in a tombstone bed. Adapted from Andrew Fowler's solution.

shear stress and water pressure modifies the overall sliding dynamics, and how important the strain enhancement effect can be when sliding over realistic three-dimensional beds.

3.6 Appendix: Analytical model of sliding with non-zero local shear stress and open cavities over square obstacles

We continue in detail the analytical model developed in the main text. This solution includes the presence of cavities, and is greatly inspired by the solution for sliding over a tombstone bed with and without open cavities done by A. Fowler as part of the exercises of the Mathematical Geoscience course in Oxford University.

3.6.1 Rate-strengthening regime

We assume a cavitation state as in Figure 3.7. The spatially averaged values are lower than the actual stress applied onto the ice,

$$\begin{aligned} \tau_u L &= (\hat{\tau}_u + p_i - p_c)2a = (\hat{\tau}_u + N)2a, \\ \tau_f L &= \hat{\tau}_f (L - L_C). \end{aligned} \tag{3.27}$$

We can rewrite the equations to have the stresses as function of the spatially averaged drags. We can estimate cavity length L_C from mass continuity. In the uncavitated part, we have

$$\frac{du_b}{dx} = -\frac{dw}{dz},$$

with w the vertical component of ice velocity. Now we consider that dw/dz can be approximated by the strain rate $\dot{\epsilon}_{zz} \approx AN^n$, the strain rate of the ice being compressed by the difference between the ice pressure and the water pressure. Taking $du_b/dx \approx u_b/(L - L_C - 2a)$ gives $u_b/(L - L_C - 2a) \approx AN^n$. To continue we define the roughness as $r = a/L$, the solid drag ratio $T = \tau_f/\tau_b$, and the portion of cavitated bed as

$$s = \frac{L_C}{L} \approx \frac{u_b}{LAN^n} - 2r. \tag{3.28}$$

We obtain the following expressions for the stresses at the uncavitated part of the bed,

Variable	Description	Unit
A	Creep parameter	$MPa^{-n}a^{-1}$
A_s	Sliding parameter if sliding with zero local shear stress	$m\ a^{-1}\ MPa^{-n}$
A_f	Sliding parameter if sliding with non-zero local shear stress	$m\ a^{-1}\ MPa^{-n}$
A_f^{Tconst}	Sliding parameter under constant T	$m\ a^{-1}\ MPa^{-n}$
A_f^{num}	Numerically computed A_f	$m\ a^{-1}\ MPa^{-n}$
a	Half bump height, sinus amplitude	m
$b(x)$	Bed height	m
c	Local shear stress in the Hallet-like model	MPa
C	Maximum attainable τ_u/N	-
C_f	Maximum attainable τ_b/N	-
C_f^{num}	Numerically computed C_f	-
C_f^{the}	C_f computed with a (semi) theoretical expression	-
H	Top boundary height	m
h_i	Height of the ice column	m
$h(x)$	Bottom of the ice	m
$h'(x)$	Slope of $h(x)$, dh/dx	-
L	Domain period length	m
L_U	Length of the uncavitated bed	m
L_C	Length of the cavity	m
$\mathbf{n}$	Normal vector	-
n	Glen's flow law exponent	-
N_{loc}	Local effective pressure	MPa
N	Mean effective pressure	MPa
p	Flow pressure	MPa
p_i	Ice column pressure	MPa
p_c	Cavity water pressure	MPa
p_w	Local subglacial water pressure	MPa
r	Bed roughness, a/L	-
s	Portion of the bed drowned by a cavity, L_C/L	-
T	Solid drag ratio, τ_f/τ_b	-
$\mathbf{t}$	Tangential vector	-
$\mathbf{u}$	Flow velocity vector	$m\ a^{-1}$
u	Horizontal component of $\mathbf{u}$	$m\ a^{-1}$
u_i	Ice velocity at top boundary	$m\ a^{-1}$
u_b	Basal slip	$m\ a^{-1}$
v	Vertical component of $\mathbf{u}$	$m\ a^{-1}$
μ	Bulk friction parameter	-
τ_b	Basal drag	MPa
τ_u	Viscous drag	MPa
τ_f	Solid drag	MPa
$\boldsymbol{\sigma}$	Cauchy stress tensor	MPa
σ_{nn}	Normal stress	MPa
σ_{nt}	Tangential stress, local shear stress	MPa

Table 3.1: Table of variables

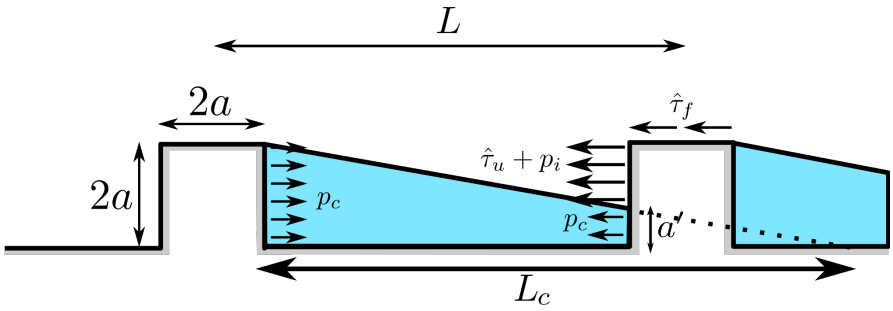

Figure 3.8: Conceptual model of square bed with open cavities that drown part of the obstacles. Adapted from Andrew Fowler's solution.

$$\hat{\tau}_u = \left(\frac{1}{2r}(1-T) - \frac{N}{\tau_b}\right)\tau_b,$$
$$\hat{\tau}_f = \frac{1}{1-s}T\tau_b.$$

Applying Glen's flow law, this gives the following strain rates around the best obstacles

$$\begin{aligned}
\dot{\epsilon}_{xx} &= \frac{1}{2}A(\hat{\tau}_u^2 + \hat{\tau}_u^2)^{\frac{n-1}{2}}\hat{\tau}_u \\
&= \frac{1}{2}A\left(\left(\frac{1}{4r^2}(1-T) - \frac{N}{\tau_b}\right)^2 + \frac{1}{(1-s)^2}T^2\right)^{\frac{n-1}{2}}\left(\frac{1}{2r}(1-T) - \frac{N}{\tau_b}\right)\tau_b^n, \\
\dot{\epsilon}_{xz} &= A(\hat{\tau}_u^2 + \hat{\tau}_u^2)^{\frac{n-1}{2}}\hat{\tau}_f \\
&= A\left(\left(\frac{1}{4r^2}(1-T) - \frac{N}{\tau_b}\right)^2 + \frac{1}{(1-s)^2}T^2\right)^{\frac{n-1}{2}}\frac{1}{1-s}T\tau_b^n.
\end{aligned} \tag{3.29}$$

Using the same arguments as for sliding without cavities, the basal speed is $u_b = \dot{\epsilon}_{xx}2a + 2\dot{\epsilon}_{xz}2a$.

3.6.2 Rate-weakening regime

Here we consider that cavities start to drown the vertical faces of the obstacles and the bed cannot support as much stress as before, see an example in Figure 3.8. The length of cavity is now $L_C > L - 2a$. The vertical face of the obstacles has been reduced to $2a - a'$, this area decreases with increasing cavitation. Conversely, the area where $\hat{\tau}_f$ applies is $2a$ for any degree of cavitation (a particularity of the tombstone model, in general it decreases with increasing cavitation).

The force balance gives

$$\begin{aligned}
\tau_u L &= (\hat{\tau}_u + N)(2a - a'), \\
\tau_f L &= \hat{\tau}_f 2a.
\end{aligned} \tag{3.30}$$

The drowned side of the obstacle, a', can be obtained by application of Thales' theorem (see Figure 3.8),

$$\frac{2a}{L_C} = \frac{a'}{L_C - L + 2a}.$$

Rewriting and multiplying by L on both sides gives

$$a' = 2a(s - 1 + 2r)/s. \tag{3.31}$$

Following the same steps as before, we have the stresses in the undrowned part of the bed,

$$\hat{\tau}_u = \frac{1}{2r - a'/L}\left((1-T) - \frac{N}{\tau_b}\right)\tau_b,$$
$$\hat{\tau}_f = \frac{1}{2r} T \tau_b.$$

And applying Glen's flow law gives

$$\begin{aligned}
\dot{\epsilon}_{xx} &= A(\hat{\tau}_u^2 + \hat{\tau}_f^2)^{\frac{n-1}{2}}\hat{\tau}_u \\
&= A\left(\left(\frac{1}{2r - a'/L}(1-T) - \frac{N}{\tau_b}\right)^2 + \frac{1}{4r^2}T^2\right)^{\frac{n-1}{2}}\left(\frac{1}{2r - a'/L}(1-T) - \frac{N}{\tau_b}\right)\tau_b^n, \\
\dot{\epsilon}_{xz} &= A(\hat{\tau}_u^2 + \hat{\tau}_f^2)^{\frac{n-1}{2}}\hat{\tau}_f \\
&= A\left(\left(\frac{1}{2r - a'/L}(1-T) - \frac{N}{\tau_b}\right)^2 + \frac{1}{4r^2}T^2\right)^{\frac{n-1}{2}}\frac{1}{2r}T\tau_b^n.
\end{aligned} \tag{3.32}$$

The basal speed is as before, $u_b = \dot{\epsilon}_{xx} 2a + 2\dot{\epsilon}_{xz} 2a$.

3.6.3 Full law

We obtain a law in three parts:

1. Weertman style, as long as $N \geq (1-T)\tau_b/(4r)$
2. Rate-strengthening with cavities, from $N < (1-T)\tau_b/(4r)$ until $s = 1 - 2r$
3. Rate-weakening regime with cavities

The law is continuous with discontinuous slope. We plot in Figure 3.9 the law for $r = 0.1$, $N = 2$ MPa, and $\tau_f = T\tau_b$ with constant T, with (solid curves) and without (dotted curves) the strain enhancement effect, with no scaling variables on the top panel and with $C_f^{\text{num}} = \max(\tau_b/N)$ and A_f^{Tconst} (see Eqn. (3.26)) on the bottom panel.

We see that the rate-weakening regime is not suppressed under constant T. Moreover, rate-weakening can only be suppressed if τ_f increases with sliding speed faster than τ_u decreases i.e. if the increase in τ_f is enough to overturn the weakening due to cavity growth. We compare in Figure 3.10 such a case with the friction law obtained for $T = 0.2$. The blue line corresponds to a friction law with rate increasing solid drag, such that the solid drag ratio is $T = 0.3 + 1.25 \times 10^{-4} u_b$. This expression for T was chosen just for illustration purposes of the possibility of rate-weakening suppression and it does not intend to represent a realistic expression of solid drag ratio.

Open Research

The numerical output and the scripts used process the data and generate the plots are accessible in the Zenodo repository of the SAUSSURE project, https://doi.org/10.5281/zenodo.5046764 (**?**).

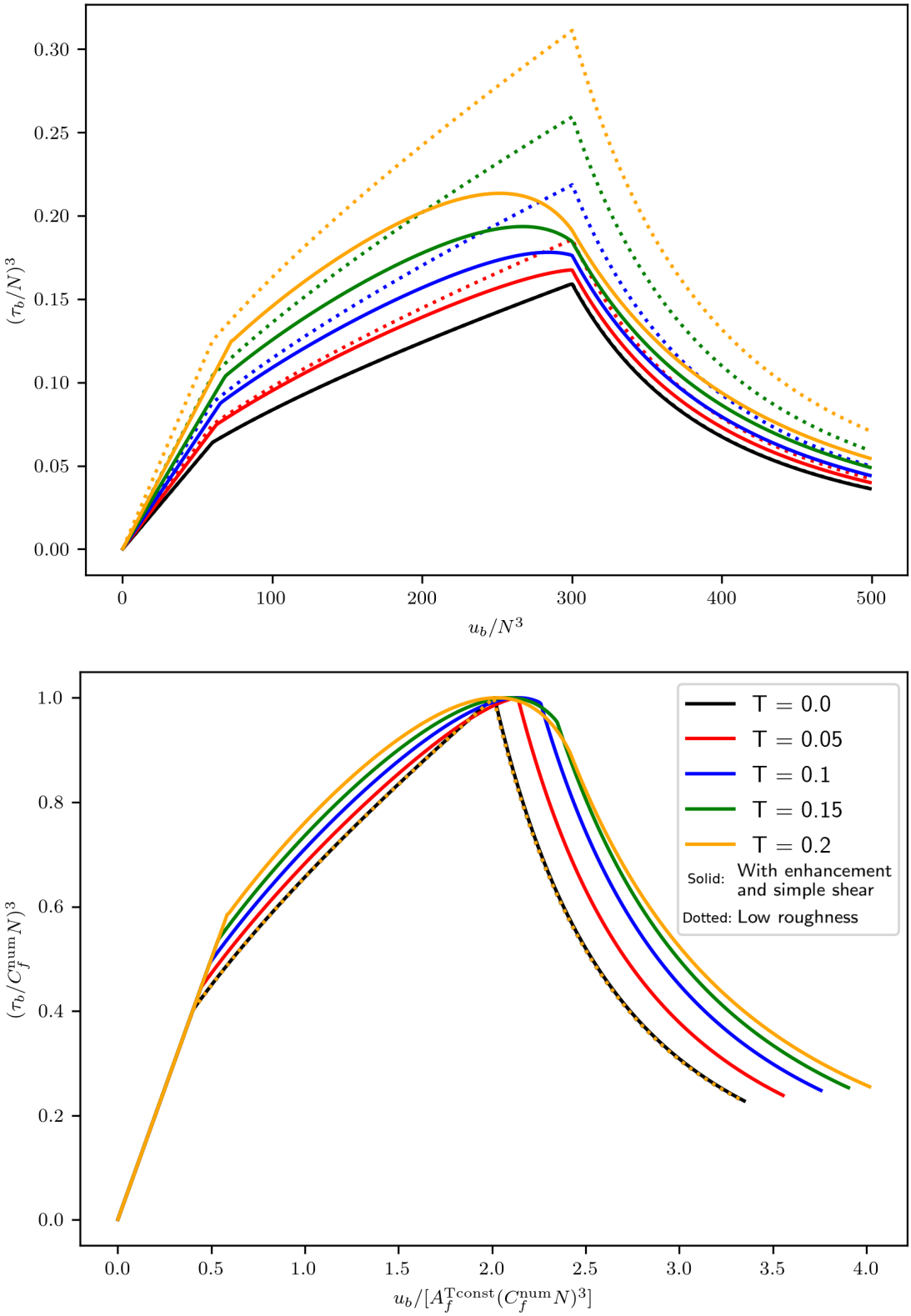

Figure 3.9: Theoretical friction laws over a tombstone bed under constant solid drag ratio, for $r = 0.1$ and $N = 2$ MPa. We show the solutions with (solid curves) and without (dotted curves) the strain enhancement effect, in their unscaled (top panel) and scaled (bottom panel) version. We can see in the top panel that at equal basal drag, ignoring the influence of τ_f in ice viscosity results in an underestimation of sliding velocity. Once properly scaled, the friction laws converge approximately into the same shape.

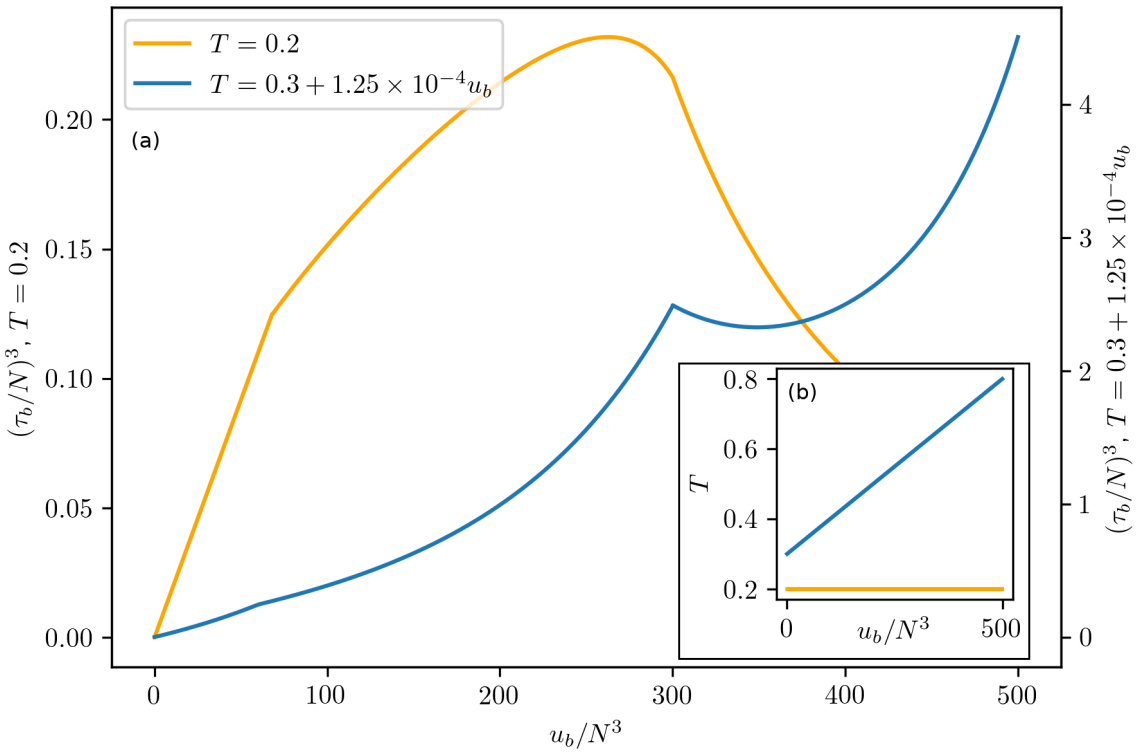

Figure 3.10: Theoretical frictions laws over a tombstone bed with constant $T = 0.2$ and linear $T = 0.3 + 1.25 \times 10^{-4} u_b$. We show the laws in the main panel (a), and the values of T in subpanel (b). Comparing the shapes of the orange and and blue curves we see that under very high and rate increasing solid drag ratio T, the friction law has no weakening, except for just after the bumps start to be drowned (u_b/N^3 between 300 and 400 m a^{-1} MPa^{-3} in this particular example). The linear expression of T of the no-weakening example (blue line) is chosen for illustration purposes only.

Chapter 4

The lost last paper(s) of Louis Lliboutry

We still have rough, incomplete and wrong theories developed in the 60's by Weertman, myself, Nye, Röthlisberger and Budd, that have but a historical interest.
Louis Lliboutry, 2005

4.1 Introduction

Louis Lliboutry's contribution to glaciology is vast, covering a wide array of topics (e.g. ice mechanical properties, geomorphology, surface processes, numerical modeling of glacier flow, theoretical fluid dynamics). The most notorious of them all is, most probably, glacier friction laws, to which he dedicated more than 20 papers. It occupied a great portion of his scientific production from the late 50's through the 60's, up to the point that the correctness of his own theories, and the incorrect theories of his peers became a personal issue. As stated by Fowler (2011), '[Weertman and Lliboutry] bickered with one another through a number of publications, variously adapting or improving (largely in cosmetic ways) their two theories. The course of this tussle was finally charted in exasperation by (Lliboutry, 1968), following which the eruptive phase entered a period of dormancy'. What Andrew Fowler probably didn't know, nor many researchers at the LGGE (the Laboratory of Glaciology and Geophysics of the Environment of Grenoble, now part of IGE), is that Louis Lliboutry continued to think about the problem long after he retired. Let's put things in perspective.

On Thursday 10th March 2005, the glaciology and snow sciences section of the SHF (Hydrotechnical French Society, or Societé Hydrotechnique Française in the original french) organised their annual meeting in Grenoble. Among the speakers there was the already retired Prof. Louis Lliboutry, and attending the presentation there was Olivier Gagliardini, then a young postdoctoral researcher. In fifteen minutes, Liboutry presented a conference paper of six pages titled *Sliding and subglacial hydraulics* (*Glissement et hydraulique sous-glaciares*, in the original french), whose first paragraph stated:

During the last three years, my intellectual activity has focused on the sliding of temperate glaciers and the subglacial flow of water. I have developed a theory of which I cannot but give here a brief and incomplete sketch. It is explained in three articles that I am finishing, and that I will submit to Journal of Glaciology.

In the following pages, he develops a new conceptual hydro-mechanically coupled model of glacier flow, including a new friction law, temporal changes in cavity volume due to transversal flow along the glacier cross section and a spatially variable water pressure. Of the three announced paper, the first one would (probably) be the model of temperate valley glaciers, the second one would treat surging glaciers, and the third one would deal with sub-daily unsteady water pressures.

The methodology sections are consistently written in the following way. Lliboutry introduces a physical process (say, the friction law), describes the idea behind his model (sliding past bumps with connected and unconnected cavities), gives some assumptions (hemispherical bumps of same radius, no regelation), continues with the resulting equation (in this case, equation (4.2)) and he adds an interpretation of it (we can expect non-negligible drag due to isolated cavities) and a motivation (this new law allows for explaining the fast sliding velocities in some glaciers). He repeats this cycle for several parts of the hydro-mechanically coupled model: the friction law, subglacial flow, the temporal evolution of the subglacial hydrology system, After presenting the model, he proposes an example for a valley glacier, "solves" it, discusses that it yields reasonable results, and closes the communication saying

In conclusion, this study shows that

- *A realistic model, taking into account the laws of Mechanics and Physics can be established. Glaciologists should not try to just look for simple correlations.*
- *There is a considerable amount of numerical calculations to be done. I leave it for the younger researchers, not taken back for the fact that the topic is not fashionable anymore.*

This introduction is partly based on the recollection of this story written by Olivier Gagliardini for Louis Lliboutry's biography, (Turrel, 2017), translated into english for the introduction of the SAUSSURE project, https://saussure.osug.fr/-History-.

The presentation and the accompanying document were regarded by the public as incomprehensible, and it was soon forgotten. In its defence, the model was quite complex to be explained in such a short time, and it can be said that since the model and its applications were going to be published in three articles, the details could be worked out later.

Unfortunately, that never happened. When Louis Lliboutry died two years later, the articles hadn't been published. Olivier Gagliardini looked for them in Lliboutry's personal notes and computer, but neither he nor Lliboutry's family could find anything. Likewise, the editorial board at *Journal of Glaciology* confirmed that they had never received any finished paper, nor any draft whatsoever. The only thing that was left was a short, convoluted document written in french that juxtaposed assumptions with results and conclusions, with only seven equations and one single figure providing part of the initial conditions needed to successfully run the model.

Fourteen years after these events, during one meeting held at the beginning of this PhD, Olivier Gagliardini immediately caught my attention when he recalled that he had scanned the document, and proposed to give it a look. He promptly shared it with a few collaborators of the SAUSSURE project, and while we realised that there was potential behind it, notably on the treatment of intra-annual dynamics changes due to unsteady water pressures, the amount of effort needed to unravel the work of Lliboutry was perhaps too much for what it was worth. The idea kept wandering around our heads while we were busy with our everyday research, and we never really got to take a further look. It wasn't until the end of 2021 that, dreading to perform yet another correction on *The effect of local shear on glacier sliding*, I decided to work on Lliboutry's last paper in order to procrastinate. I couldn't have done it in a better time, since the experience during my PhD had led me in a pretty good position to

reverse engineer the models presented by Lliboutry and provide a reasonable exposition of the model. Working on analytical friction laws, and having passed time with Lliboutry's first (english written) paper on glacier friction laws (Lliboutry, 1968) helped me understand his geometrical reasoning, which was key to unravel the equations proposed. The experience dealing with the actual dynamics of mountain glaciers, and their complex mechanical behaviour (e.g. effect of valley sides, distribution of subglacial channels, opening and closing of cavities) helped interpret the physical, non-equations based, aspect of the paper. A few dedicated weeks during spring and summer 2022 and the opportune assistance of Facu Sapienza just after the 2022 Karthaus Summer School helped me iron most of the details of the paper that were still around[1], and thus this account became possible.

In the following sections I will introduce the problem, the hypothesis behind, and the model. The original structure has been changed to make the article more understandable, and all the diagrams are new. All numbered equations are as given in the original paper, while those that have been written to improve the understanding are unnumbered. For internal consistency we rename all variables with the nomenclature already used in this dissertation (i.e. basal speed will be called u_b, not U as in the original). We try to keep the definition of new variables to a minimum. The model proposed by Lliboutry was based on a few assumptions and can be considered for a glacier valley of any shape and roughness. The particular example that he proposed was more refined, and included the assumption that the glacier valley was parabolic, with given values for the physical parameters of the problem, e.g. bed roughness, permeability, height and width of the valley.

The work will be presented in the following way. First, we will provide the set up and main hypothesis. Then, we will treat the friction law (slip law, actually), and the treatment of cavities. Later, we will continue with changes due to subglacial flow, including the permeability and the temporal evolution of cavities. We will follow with some words about the spatial distribution of stress. Finally, we will provide the numerical scheme to solve the paper.

4.2 Preliminary considerations

Let's consider an infinitely long glacier flowing down a parabolic-shaped valley, of maximum height H and half-width D, as shown in Figure 4.1. We will work with three directions, the along flow direction x, the upwards vertical direction z and the across flow direction along the bed profile, s, different from the horizontal direction y, with origin at the mid point of the bed. The bed height is given by $b(y) = (H/D^2)^2 y^2$, and the thickness is simply $h(y) = H - b(y)$. The conversion from y to s is

$$s(y) = \frac{1}{2} y \sqrt{4\frac{H^2}{D^4} y^2 + 1} + \operatorname{asinh}\left(2\frac{H}{D^2} y\right)\left(4\frac{H}{D^2}\right)^{-1}.$$

With s we can define the reduced coordinate $S = s/s_1$, where $s_1 = s(D)$ is the length of half the profile. Ice creep follows Glen's flow law, with creep parameter A and Glen's law exponent $n = 3$. Regelation and local shear stress at the ice - bed interface are neglected.

If we focus on the bed at the local scale, we model the bed as a flat plane with hemispherical bumps of radius R, see Figure 4.2, separated by a distance λ from each other (or, conversely, there is one bump per every λ^2). We define the roughness r as the frontal section of the bumps that the

[1] I have not been able to solve it, though. Some work is still to be done to fully determine the potential behind Lliboutry's last lost paper(s).

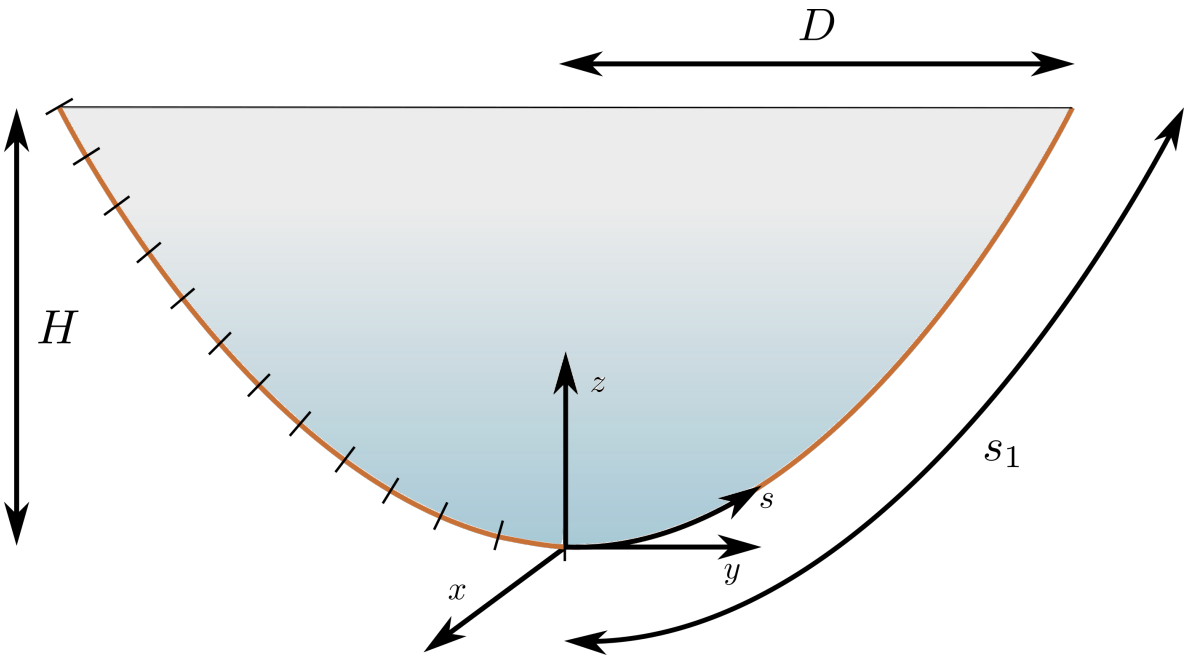

Figure 4.1: Cross section of a parabolic glacier valley of depth H and half-width D. The left branch of the bed is discretized in 12 elements, as considered by Lliboutry for his example.

glacier must overcome per unit area, therefore

$$r = \frac{\pi}{2} R^2 \frac{1}{\lambda^2}.$$

If the subglacial water pressure at the lee side of the bumps is high enough, cavities will open. The cavities are approximately modeled as spheroids (as depicted in panel (b) of Figure 4.2), with principal axes R (along z), R (along s), and L (along x), where L is called the cavity length and is computed from the last point of the bump on which they open till the tip of the cavity, as depicted in Figure 4.2 (a,c). The volume of the cavity is thusthe quarter of an spheroid, yielding

$$V_c = \pi R^2 L/3.$$

Lliboutry considers that cavity length attains a maximum $L_M = \lambda - R$ when the cavity connects with the downstream cavity as depicted in the top left bump in Figure 4.2. This allows us to define a reduced cavity length l, such that

$$l = \frac{L}{L_M} = \frac{L}{\lambda - R},$$

$l = 0$ when there is no cavity, and $l = 1$ when there is hypercavitation, i.e. all bumps are connected with downstream bumps. Each cavity is at a pressure p_c, such that the effective pressure of the ice around the cavity is $N = p_i - p_c$. In the case of cavities at the atmospheric pressure (i.e. empty of water) this is simply $N = p_i$, while in the case of unconnected cavities we assume that they stay at equilibrium with the surrounding ice, and thus $N = 0$. At any point at the bed, the hydraulic head Z, taking as reference the origin, is the sum of the cavity pressure head and the height of the bed (related to the potential

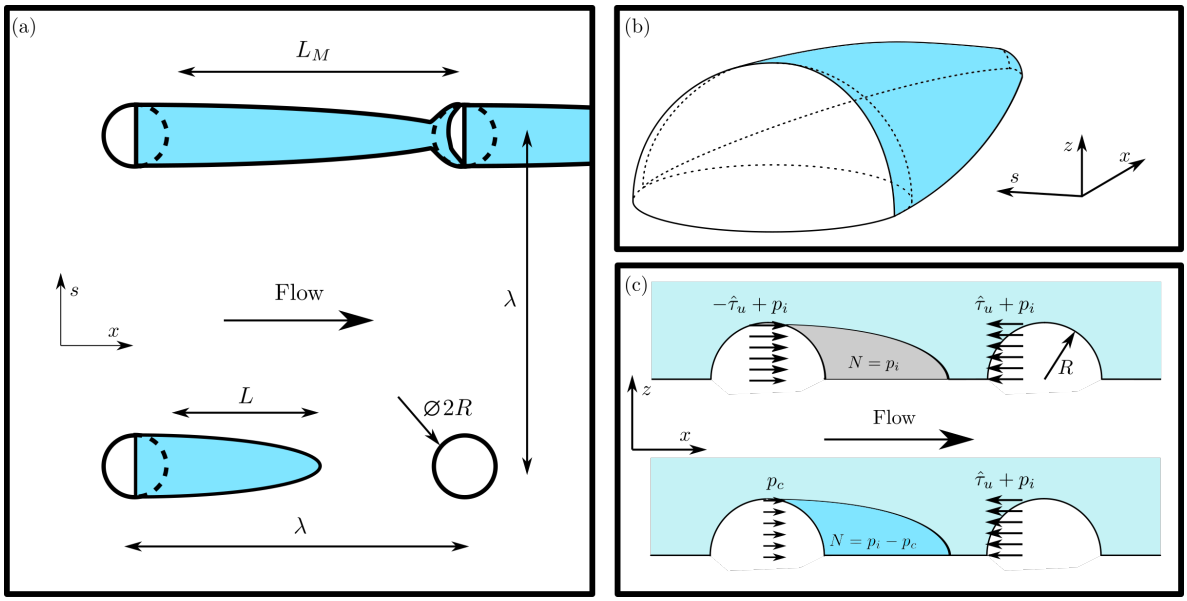

Figure 4.2: Meso scale description of the bed envisioned by Lliboutry. We give a top view in panel (a). The shape of the cavity behind the top left bump is drawn so as to have the cavity go around the bump and connect with the downstream cavity, which should happend for $L = L_M$. In panel (b) we draw a perspective of the spheroidal cavities behind a bump. Panel (c), similar to Figure 2 of chapter 3shows the distribution of stresses needed for the friction law described by LLiboutry.

gravitational energy). Therefore, we can write

$$Z(s) = \frac{p_c}{\rho_w g} + b(y(s)) = \frac{-N + \rho_i g h(y(s))}{\rho_w g},$$

where ρ_i and ρ_w denote ice and water density, respectively.

The subglacial hydrology network is not uniform, and can be composed of a mix of isolated and connected cavities. This network is spatially heterogeneous, such that we can observe, for instance, a series of isolated cavities of different lengths on the margins, a partially connected system of cavities towards the center, and a subglacial channel with fully connected cavities on the central part of the bed. In order to account for that, we will consider a connection ratio c, where $c = 0$ means all bumps are unconnected, the water pressure must be in equilibrium with the surrounding ice at every cavity, and $c = 1$ means intense cavitation, and all bumps and their cavities are freely connected between them. Lliboutry considers that even in the absence of cavities, there must be some bumps hydraulically connected to each other, such that sliding is favored at these bumps. On the other hand, if cavities grow, more bumps become connected and at the same pressure. A simple solution to reconcile these two assumptions is to consider the following connection ratio (equation 2 in the original),

$$c = c_0 + (1 - c_0)l. \tag{4.1}$$

We call c_0 the background connection ratio. If all cavities are connected, $l = 1$ and then $c = 1$.

4.3 Friction law

Since we saw earlier in chapter 3 how to obtain a simple friction law, we will go over the details here. For those bumps that don't have open cavities or whose cavities are unconnected such that the water

pressure within the cavity is equilibrium with the surrounding ice, we have a Weertman type friction law,

$$\tau_n = \left(\frac{u_b}{A_1 R}\right)^{1/3} 2r.$$

In the case of cavities within connected cavities, we have

$$\tau_c = \left[\left(\frac{u_b}{A_1 R}\right)^{1/3} + N\right] r.$$

Now, considering that both unconnected bumps (ratio $1-c$) and connected bumps (ratio c) contribute proportionally to the basal drag, we have that at equal basal speed

$$\tau_u = (1-c)\tau_n + c\tau_c = (1-c)\left(\frac{u_b}{A_1 R}\right)^{1/3} 2r + c\left(\frac{u_b}{A_1 R}\right)^{1/3} r + cNr = (2-c)\left(\frac{u_b}{A_1 R}\right)^{1/3} r + cNr.$$

The friction law is not anymore a function of the type $\tau_u = f(u_b, N)$, but $\tau_u = f(u_b, N, c)$. A more compact form, similar to the friction law developed in chapter 3 is

$$\frac{\tau_u}{N} = \left[(2-c)\left(\frac{u_b}{A_1 N^3 R}\right)^{1/3} + c\right] r.$$

We can rewrite the friction law to make it a slip law, obtaining the same equation as Lliboutry (equation 1 in the original),

$$u_b = A_1 R\left(\frac{\tau_u/r - cN}{2-c}\right)^3. \tag{4.2}$$

4.4 Subglacial permeability

The spatially and temporal variable hydraulic conditions require water transport through the subglacial network. Let's consider that the hydraulic gradient is continuous at the local scale, such that we can apply Darcy's law for the subglacial water flow parallel to the main flow axis (along x) $\varphi_{\parallel}$ and perpendicular to the main flow axis (along s) $\varphi_{\perp}$, we have

$$\varphi_{\parallel} = -K_{\parallel}\frac{\partial Z}{\partial x};\ \varphi_{\perp} = -K_{\perp}\frac{\partial Z}{\partial s}. \tag{4.3}$$

With cavity volume known and some rewriting we have the amount of water per unit area,

$$W = \frac{2}{3}crL = \frac{2}{3}rmR\left[c_0 l + (1-c0)l^2\right], \tag{4.4}$$

we call $m = L_M/R$ the shadow slope, since it is the (approximate) slope between the highest and the lowest point of the cavity. With the water flow and the volume established, we can now write the conservation of mass for water within the subglacial hydrology system. Assuming that W stays relatively uniform in x, but varies along s, we have that any temporal changes in the stocked water volume is due to lateral flow,

$$\frac{\partial W}{\partial t} + \frac{\partial \varphi_{\perp}}{\partial s} = 0. \tag{4.5}$$

Rewriting to use S, allows us to obtain the rate of redistribution of Z as a function of the temporal evolution of cavity length,

$$\frac{\partial^2 Z}{\partial S^2} = -\frac{\partial W}{\partial t} = E\left[c_0 + 2(1-c_0)l\right]\frac{\partial l}{\partial t}, \tag{4.6}$$

with $E = 2rmRs_1^2(3K_\perp)^{-1}$.

4.5 Closing the system

So far, there are four independent variables, $u_b(S,t)$, $\tau_b(S,t)$, $l(S,t)$ and $Z(S,t)$. In order to solve the system, we have equations (4.2) and (4.6), such that we need to provide two more. This section is perhaps the most complex to understand of the original document, since it has almost no hints. I will therefore present what Lliboutry wrote, and my interpretation of it based on physical reasoning. The results in this section can be considered, at most, an educated guess.

The third equation is given by the plastic deformation of the cavity, a balance of two competing processes, the cavity opening due to sliding v_o, and cavity closing due to creep v_c(e.g. Werder et al., 2013),

$$\frac{\partial L}{\partial t} = v_o(u_b) - v_c(A_1, N^3).$$

We schematize both processes in Figure **??**. Let's consider a cavity at time t with volume $V = 1/3\pi R^2 L$, as discussed earlier. If we consider only cavity opening due to sliding (ice is turned into a solid), in a dt the ice advances $u_b dt$, and the cavity grows to have a volume $V^* = V + dV = V + 1/2\pi R^2 u_b dt$. To accomodate the new volume, the cavity will have a new length L^*, such that we have

$$1/3\pi R^2 L^* = V + dV = 1/3\pi R^2 L + 1/2\pi R^2 u_b dt.$$

Rewriting the terms, and considering $dL/dt = (L^* - L)/dt$

$$\frac{dL}{dt} = \frac{3}{2}u_b.$$

Focusing on cavity closing, **read werder and hewitt and schoof to see what they say about cavity opening** Lliboutry provides the following result with no further ellaboration,

$$\frac{\partial l}{\partial t} = \frac{3}{2mR}\left[u_b - A_1 R(1+ml)N^3\right], \tag{4.7}$$

valid for $0 \leq l \leq 1$.

The fourth equation is even more obscure. Lliboutry claims that *the fourth relationship comes from the fact that τ_u and u_b are components of the stress and velocity tensors on the whole glacier.[...] Fortunately, we can find good approximations of $\tau_u(S)$ and $u_b(S)$ using 4th degree polynomials, only dependant on $\tau_u(S=0) = \tau_0$ and $\tau_u(S=1) = \tau_1$, provided we consider a cylindrical glacier with parallel flow. Explaining how to determine them would be too long to be done here. Let's only say that if we know l and Z on 5* control points*, regularly spread over the demi-transverse profile of the glacier, there is one unique solution to this mathematical problem*.

What are those polynomials? We have no more information on how to obtain them, only that they must depend on five constants, so as to need five points to determine them. Thus, we look for

polynomials of the form

$$\tau_u(S) = \alpha S^4 + \beta S^3 + \gamma S^2 + \delta S + \tau_0,\ u_b(S) = aS^4 + bS^3 + cS^2 + dS + u_{b0}$$

If we dig deep in Lliboutry's works, we find that in Lliboutry (1969), through successive approximations and 84 equations over 21 pages, Lliboutry derives this type of equations for τ and u_b for plane and cylindrical glaciers. The results of such paper are not directly applicable to this case, though.

Chapter 5

Borehole inclinometry

The velocity of the surface is sensibly the same as [...] 100 feet deep in most glaciers
It is only near the bottom or bed that the velocity is materially affected.
J.D. Forbes, 1842, at the beginning of glaciology as a scientific discipline.

5.1 Introduction

For more than 70 years, glaciologists have been using boreholes to observe the deformation of glaciers and measure their internal velocity. This technique has been used in combination with others observations such as surface velocities (with GPS networks, for instance) or subglacial water pressures, to improve our understanding of bed processes, since direct access to the bed of glaciers is almost impossible. Among the studies that have used borehole inclinometry, we find a variety of goals. Since the work of Glen (1955), glaciologists have used borehole inclinometry to constrain ice rheological parameters (e.g. Perutz, 1950; Miller, 1957; Mathews, 1959), or constrain bed roughness (Ryser et al., 2014; Maier et al., 2019). Comparing the internal velocity with surface velocities allowed other researchers to infer (or at least estimate) basal velocities, which could then be used to compare seasonal or intra-seasonal changes in surface, internal, and/or basal dynamics (Hooke et al., 1992; Harper et al., 1998; Amundson et al., 2006; Willis et al., 2003; Gudmundsson et al., 1999). Some studies, usually the first ones, were interested also in determining whether basal ice travels faster than overlaying ice or not (an early debated phenomenon called extrusion flow Perutz, 1950; Sharp, 1953; Mathews, 1959; Hooke et al., 1987).

In this chapter, we will do a quick review on the field techniques used to measure glacier deformation and other related field methods. We will provide a resume of the previous studies of interest for this PhD. We will finish with an overview on methods to infer deformation and velocities from borehole inclinometry and how to simply estimate uncertainties with the type of sensors used in chapters 6 and 7.

5.2 Field techniques

5.2.1 General principles

Borehole inclinometry consists in measuring the internal deformation of a glacier through surveying the change in tilt of one or several vertical boreholes drilled, ideally, from the surface to the base. The amount of information that can be extracted from borehole inclinometry depend on the technique used, the density of boreholes, and the quality of the instrumentation (e.g. measuring frequency, in-depth density of measurements, accuracy) and the borehole itself (verticality, borehole diameter, depth). As we will see later, different techniques can provide a series of snapshots of the internal deformation, with good spatial coverage, or on the contrary, allow for observing sub-daily changes in deformation with lower spatial density. The information extracted also depends on the spatial arrangement of boreholes on the surface of the glacier. Boreholes close to each other (at least at distances lower than an ice-thickness) can help isolate the influence of local differences in the subglacial hydrology network (Willis et al., 2003), or in bed roughness (Maier et al., 2019), while boreholes located further from each other can provide a more general picture of the ice flow. Boreholes along a main flow line provide invaluable information about the principal component of ice flow, while boreholes drilled transverse to the main flow direction allow for better constraining the internal three dimensional flow of a glacier (Raymond and Harrison, 1975; Copland et al., 1997; Willis et al., 2003).

Good quality drilling helps ensure that the borehole stay vertical and reach the bed more easily. In such a case, borehole inclinometry can be used to observe the complex deformation that takes place above a glacier's bed, and provide a more accurate measure of basal velocity. Further complications arise when working in temperate glaciers. First and foremost, temperate glaciers do not freeze, except close to the surface if ambient temperatures are below zero. The direct consequence of these is that unless close to the surface, we will have to wait for creep to close the borehole and ensure the coupling between the sensors and the glacier. If working in a valley glacier, it is common to find rocks and stones in the ice that complicate drilling (Flusin and Bernard, 1909; Mathews, 1959; **?**; Roldan-Blasco et al.). The deeper the boreholes reach, and the longer the survey period, the stronger the strains they will be subjected to. Thus, it is not uncommon for borehole derived studies to start failing (i.e. for boreholes to become unreachable) from the bottom up to the top (Hooke and Hanson, 1986; Doyle et al., 2018; Maier et al., 2019; Roldan-Blasco et al.). For the same reason it is particularly useful in low strains environments, such as rock glaciers (e.g. Arenson et al., 2002). We will later see the influence of these problems in our assessments of glacier deformation in Glacier d'Argentière, in chapters 6 and 7.

5.2.2 Repeated inclinometry

Repeated inclinometry is the oldest technique for determining the internal deformation of a glacier. It consists in measuring the shape of a borehole during different times over the course of a field campaign. Inclinometry readings can be obtained by lowering a tiltmeter that, following the shape of the borehole, measures its inclination and orientation, i.e. the tilt and azimuth, at a certain spatial interval. As borehole tends to close, there are different ways of keeping it open for future surveys. The borehole can be cased in a metal (typically aluminium) tube (e.g. Miller, 1957; Mathews, 1959) for easier operation of the tiltmeter. An important source of uncertainty comes from the degree of coupling between the tube and the surrounding ice, which difficulties identifying if the measured change in tilt is the same as that of the glacier. Another variation of this technique can be found in Raymond (1971). This alternative installs a cable in an uncased borehole, which guides the tiltmeter as it moves

through the borehole. Following field surveys then redrill the borehole along the cable and measure it again.

Since the tiltmeter has to travel the borehole twice, one descending and one ascending, repeated inclinometry provides two sets of readings per borehole per survey, which minimizes the measuring error. Copland et al. (1997) surveyed three boreholes up to 7 times, providing therefore 14 sets of measurements per borehole. Apart from the (potential) low error in the inclinometry measurement, repeated inclinometry provides observations with good in-depth spatial density, typically every one or two meters. Material wise, it can be argued that it is not expensive, since except for the casing or cables, which stay trapped in the ice, the rest of the instruments are recovered after every borehole is measured. On the other hand, it is field work intensive since drilling and measuring deformation can take hours per borehole. As a result, the time interval between surveys are of the order of weeks or months. Some studies have used this technique to characterize the flow over a great portion of the glacier, installing a dense network of boreholes along and across flow to study temporal and spatial differences in internal dynamics (e.g. Raymond and Harrison, 1975; Harper et al., 1998; Willis et al., 2003).

5.2.3 Englacial tiltmeters

A more modern technique is the use of permanently installed sensors, called tiltmeters, that measure continuously the borehole deformation. Other sensors can be added to provide complementary information, such as piezometers to record water pressure or calorimeters to measure the temperature of the ice.

Tiltmeters are usually designed *ad-hoc*, and are typically found in two versions. The most complete design measures the tilt and azimuth, either with two orthogonal accelerometers Ryser et al. (2014); Maier et al. (2019, 2021), or with an accelerometer and a magnetometer (Lee et al., 2019; Roldan-Blasco et al.). The first accelerometer allows the sensor to measure its tilt, while the second one allows for computing the azimuth with respect to a machine 'zero' direction. The magnetometer allows computing the azimuth with respect to the magnetic north. The simplest design just measures the tilt using a single triaxial accelerometer, such that the direction of tilt change is typically assumed as the flow direction at the instruments location. Examples of this latter design can be found in Gudmundsson et al. (1999) and in the tiltmeters installed in 2021 on the right side of Glacier d'Argentière, explain in chapter 7. Special attention must be given to instrument construction and calibration, since once installed there will be no way to retrieve them and modify them.

Englacial tiltmeters can be considered complementary to repeated inclinometry. First, they record glacier deformation at high temporal frequency, of the order of hours, see tables 5.1 and 5.2. As long as the sensors are connected to an external power source, they operate autonomously, reducing the amount of field trips necessary. Moreover, if communication networks are available, wireless data transmission reduces even further the density of field trips with respect to repeated inclinometry. With respect to the spatial density of sensors, on one hand the advent of cheap microcontrollers rends the material cost down and facilitates reasonable spatial density, see in Table 5.2 how the distance between sensors has been generally decreasing with time. On the other hand, the time spent building and calibrating the sensors is pretty high, which limits the deployment of large number of boreholes.

5.3 Surveys of temperate glaciers

In this section we provide a couple of tables that resume borehole inclinometry surveys in temperate glaciers, and surveys with englacial tiltmeters in polythermal glaciers. Thus, we have left out of this review those studies carried out in ice-sheets using repeated inclinometry (e.g. Dahl-Jensen and Gundestrup, 1987), or carried out in cold glaciers (e.g. Hooke, 1973; Hooke and Hanson, 1986) or rock glaciers (e.g. Arenson et al., 2002). Column *Study* shows the original paper in which the study appears. Sometimes the same inclinometry study stems several research papers, such as Harper et al. (1998, 2001) or Maier et al. (2019, 2022), in which case we show the first. Column *# BH* denotes the number of boreholes instrumented, even though some of them could not be properly studied (see for instance our case in chapter 6). *Location* describes how the boreholes where arranged with respect to the main flow direction (along, or transverse to it), and where on the glacier (center means centerline, margin means at or between the center and one or both lateral margins). *Duration* reflects the duration of the survey considered in the analysis of each study, not necessarily the time during which individual boreholes were studied. Δt shows either the average time between repeated inclinometry measurements, or the frequency with which englacial tiltmeters record their tilt. Δz gives the distance between repeated inclinometry measurements or the maximum and minimum distances between consecutive tiltmeters. In *Notes* we provide accessory information. Some compromises had to be made to be able to resume in this table the different information given in the original works, and another reviewer may choose to compile the information differently. Therefore, we advise to check the source material for the specific details regarding these studies.

Study	Glacier	Technique	#BH	Location	Depth m	Bed	Duration	dt	dz m	Notes
Perutz (1950)	Jungfraujoch (Switzerland)	Repeated	1	-	-	Yes	14 months	14 months	12	First study with repeated inclinometry
Sharp (1953)	Malaspina Gl. (USA)	Repeated	1	Center	305	No	1 year	3-5 weeks, 1 year	15	Only half the thickness was bored
Miller (1957)	Taku Glacier (USA)	Repeated	1	Center	75	No	38 months	4 - 15 months	1.5-6	Only 1/4 of the thickness was bored
Mathews (1959)	Salmon Glacier (USA)	Repeated	1	Center-ish	495	Yes	94 days	94 days	15-30	5 other boreholes were uninstrumented
Meier (1960)	Saskatchewan Glacier (Canada)	Repeated	1	Center	45 - 75	No	2 years	1 year	7.6	A very good example of how ungrateful borehole driling can be on temperate glaciers
Savage and Paterson (1963)	Athabasca Glacier (USA)	Repeated	4	Along 2 lines per side	314-206	Yes	3 years	1 year	15-7.5	Ice blocked three boreholes during the survey
Shreve and Sharp (1970)	Blue Glacier (USA)	Repeated	6	5 along center, 1 at margin	119-224	Yes	5 years	1 year	7.5	Only 1 borehole reached lower than 80% thickness
Hooke and Holmlund (1987)	Storglaciären (Sweden)	Repeated	1	Center	126	Yes	2 months	1 - 2 weeks	1 m	Observe extrusion flow during summer.
Hooke et al. (1992)	Storglaciären (Sweden)	Repeated	3	Center and margin	130 - 162	Yes	3 years	1 - 2 weeks	1 m	The profile of deformation changed during summer.
Copland et al (1997)	Haut Glacier d'Arolla (Switzerland)	Repeated	25	Across glacier	250 - 25	Yes	3 weeks	2 - 3 weeks	1 m	Short time between surveys yield too high uncertainties
Harper et al. (1998)	Worthington Glacier (USA)	Repeated	28	Along and across	180 - 200	Yes	60 - 70 days	1 - 30 days	2 m	Good 3D field of deformation. Most boreholes reached 10 m from the bed.

Table 5.1: A review of inclinometry surveys in temperate glaciers with any technique, and in polythermal glaciers with englacial tiltmeters. Part 1 of 2. More details in the text.

Study	Glacier	Technique	#BH	Location	Depth m	Bed	Duration	dt	dz m	Notes
Gudmundsson et al. (1999)	Unteraargletscher (Switzerland)	Englacial	1	Center	260	No	2 years	6 h	25 - 85 m	First study with englacial tiltmeters
Willis et al. (2003)	Haut Glacier d'Arolla (Switzerland)	Repeated and englacial	7	Along center and margin	30 - 130	Yes	15 months	15 months	1	Highly spatial variability in seasonal evolution of velocities
Keller and Blatter (2012)	Rhonegletscher (Switzerland)	Englacial	1	-	119	Yes	27 months	5 min - 8h	20	Other borehole was installed in Gornergletscher, with 1 tiltmeter
Ryser et al. (2014)	Greenland Ice Sheet	Englacial	4	Center	700 - 620	Yes	1 year	10 min	1 - 100	Kink in du/dz close to the base due to bed bumps and sticky/slippery patches
Doyle et al (2018)	Store Glacier (West Greenland)	Englacial	1	Center	611	Yes	2 months	1 h	4 - 150	Only 5 tiltmeters, most of them close to each other at the bed.
Maier et al. (2019)	Greenland Ice Sheet	Englacial	9	Margin	640 - 688	Yes	2 years	2 - 4 h	10 - 20	Kink in du/dz close to the base due to hard-bed sliding over obstacles
Leet et al. (2019)	Jarvis Gl. (USA)	Englacial	2	Margin	18 - 72	Yes	1 year	6 h	1 - 9	Found high enhancement factor (possibly anisotropy)
Roldan-Blasco et al (in prep)	Glacier d'Argentière (France)	Englacial	5	Along center	235	Yes	13 months	30 min	1 - 20	See chapter 6
Roldan-Blasco et al (in prep)	Glacier d'Argentière (France)	Englacial	4	Along margin	160-190	Yes	9 months	30 min	1 - 40	See chapter 7.2

Table 5.2: A review of inclinometry surveys in temperate glaciers with any technique, and in polythermal glaciers with englacial tiltmeters. Part 2 of 2. More details in the text.

5.4 Tilt data analysis

5.4.1 Models of deformation

The goal of inclinometry is, ultimately, the determination of the velocity gradient tensor $\mathbf{L}$. As we mentioned earlier in chapter 2.2.2, $\mathbf{L}$ has nine independent components, one for the derivative of each component of the velocity vector with respect to each direction in a three dimensional space. However, borehole inclinometry only constrains, at maximum, three of such components (one per direction), with an additional constrain is given by mass conservation. Thus, the rest of the components must be either ignored (the most common method), obtained with a different technique such as numerical modeling (see chapter 6) or interpolating from surface strains (Hooke, 1973; Hooke and Hanson, 1986). We will briefly review different methods found in glaciological literature to retrieve the internal deformation. We will assume the orthonormal reference system indicated in chapter 2.2.2 with x the main flow direction and z the vertical upwards, and velocity vector $\mathbf{u} = (u, v, w)$.

The simplest of these methods neglects all components other than horizontal shear in the flow direction, du/dz. We can relate the temporal change in tilt with du/dz (Lüthi et al., 2002; Ryser et al., 2014; Doyle et al., 2018; Maier et al., 2019) as,

$$\frac{du}{dz} = \frac{1}{dt}\frac{dx}{dz} \approx \frac{1}{\Delta t}\Delta \arctan\theta, \tag{5.1}$$

where Δt is a given time period and $\Delta \arctan\theta$ is the change in the arc tangent of tilt during that time period. If the tilt is obtained with repeated inclinometry, Δt is typically the time difference between measurements. In the case of englacial tiltmeters, the higher frequency of data acquisition allows for using smaller Δt for seasonal and sub-seasonal studies of deformation (see Ryser et al., 2014; Maier et al., 2021, and chapters 6 and 7). If tilt can be decomposed into tilt in the $X-Z$ and $Y-Z$ planes, this equation is usually applied separately to compute $\partial u/\partial x$ and dv/dz, respectively (Maier et al., 2019). Otherwise, all tilt is assumed to be contained in the $X-Z$ plane (Gudmundsson et al., 1999, and chapters 6 and 7), a reasonable approximation if we expect symmetric flow.

In case of non-zero along-flow extension or compression, the tilt of the borehole will be affected: along-flow extension will increase the tilt, while compression will dampen it (Nye, 1953; Shreve and Sharp, 1970; Hooke, 2005; Keller and Blatter, 2012). Similarly, if there is significant vertical flow the shape of the borehole will change, and so it must be taken into account. If we assume two-dimensional steady flow, the deformation can be computed as (Hooke, 2005)

$$\frac{\partial u}{\partial z} = \frac{\partial}{\partial t}\tan\theta - 2\frac{\partial u}{\partial x} + w\frac{\partial}{\partial z}\tan\theta. \tag{5.2}$$

The first term on the right hand side is the same as in Eqn. (6.1), the second represents the effect of $\partial u/\partial x$ and dw/dx, and the latter term is the advection term, as differential vertical flow will also change the shape of the borehole. Note that the total derivative of the velocity are now partial derivatives. Eqn. (5.2) requires *a priori* knowledge of the $\partial u/\partial x$ and w, which are usually unknown. A more complex expression is given by Keller and Blatter (2012), who provide an analytical solution of tilt evolution intended for englacial tiltmeter analysis. If we neglect the change in shape due to vertical movement

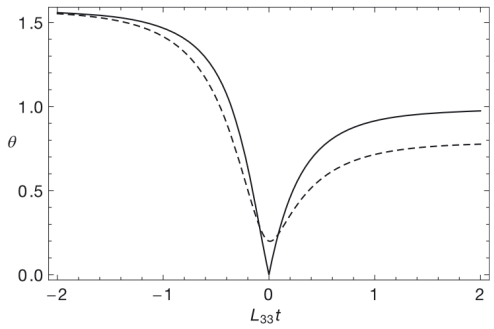

Figure 5.1: Temporal change in tilt θ (in rad) under two different conditions. The solid curve has $\partial u/\partial z = 3\partial w/\partial z$, and $\theta_0 = 0$ (tiltmeter contained in the X - Z plane). The dashed line has $\partial u/\partial z = 2\partial w/\partial z$, and is initially off the vertical plane, such that its minimum tilt is $\theta_0 = 0.2$ rad. Extracted from Keller and Blatter (2012).

(last term in Eqn. (5.2)), we have

$$\begin{aligned} \theta(t) &= \arctan\sqrt{\zeta(t)}, \\ \text{with } \zeta(t) = e^{-2tL_{33}}&\left(\frac{L_{13}}{L_{33}}\tan\theta_0\cos\phi_0 - \frac{L_{13}^2}{2L_{33}} + \tan^2\theta_0\sin^2\phi_0\right) \\ &+ e^{-4tL_{33}}\left(\tan\theta_0\cos\phi_0 - \frac{L_{13}}{2L_{33}}\right)^2 + \frac{L_{13}^2}{4L_{33}^2}. \end{aligned} \tag{5.3}$$

We keep the original notation for simplicity, and remind that $L_{13} = \partial u/\partial z$ and $L_{33} = \partial w/\partial z$.

Since englacial tiltmeters provide accurate tilt curves, this solution can be easily inverted to estimate best fitting $\partial u/\partial z$, $\partial u/\partial x$ and $\partial w/\partial z$ (Keller and Blatter, 2012; Ryser et al., 2014; Maier et al., 2019, and chapters 6). Under the same $\partial u/\partial x$, the deformation of the borehole will increase if $\partial u/\partial x > 0 > \partial w/\partial z$, and it will be dampened if $\partial u/\partial x < 0 < \partial w/\partial z$. An advantage of Keller and Blatter (2012) solution over Eqn. (5.2) is that Eqn. (5.3) also takes into account out-of-plane tilting, which happens in two-dimensional flow when the tiltmeters are not installed in the $X-Z$ plane. We use this model later in chapter 6 to estimate normal strain-rates in Glacier d'Argentière.

To finish this section we will mention the numerical scheme used in Gudmundsson et al. (1999). In their analysis of deformation in Unteraargletscher (Switzerland), Gudmundsson et al. (1999) proposed an algorithm that traced the movement of a lagrangian vector (representing the tiltmeter) subjected to a known flow field. Thus, we can represent any velocity gradient tensor and observe how the tilt and azimuth of a tiltmeter evolves with time. Conversely, we can explore a variety of flow conditions (tune the parameters of the model) to find the best fitting combination and obtain reasonable estimates of deformation (Gudmundsson et al., 1999).

5.4.2 Computation of internal and basal velocity

The deformation velocity $u_d(z)$ is typically computed by integration of $\partial u/\partial z$ between the bed and a depth z. If we have a series of N observations of du/dz, we can use the trapezoidal rule to obtain the deformation velocity between the deepest measurement ($k = 0$) and the uppermost measurement ($k = N$) as

$$u_d(z_N) \approx \sum_{k=1}^{N} \frac{\partial u/\partial z_{k-1} + \partial u/\partial z_k}{2}\,(z_k - z_{k-1}). \tag{5.4}$$

Where sub-index k indicates the observation number. In case of insufficient vertical resolution the velocity computed with this method will have high uncertainties (Gudmundsson et al., 1999; Doyle et al., 2018).

Provided that surface velocity u_s is measured, the basal speed u_b can be computed as the residual component of u_s,

$$u_b = u_s - u_d(z_N). \tag{5.5}$$

By virtue of this definition, u_b combines sliding (i.e. the basal speed at the ice-bed interface) with the deformation velocity between the bed and the deepest measurement of $\partial u/\partial z$. If the borehole does not reach the bed, some assumptions can be made to estimate the basal velocity. For instance, we can fit a polynomial function to $u_d(z)$ and extrapolate the values up to the base to obtain the deformation velocity through the whole ice thickness, and then inferr the basal velocity like Hooke and Hanson (1986) did. Another option is given in Gudmundsson et al. (1999), who instead of computing the velocity in Unteraargletscher (Switzerland) from inclinometry, assumed the distribution of horizontal and vertical velocities (based on observations and reasonable assumptions), and tuned the values of $u(x,z)$, and $w(x,z)$ until the synthetic tilt curves matched the observed ones. Finally, we can solve this problem by ignoring it and accepting that the retrieved basal velocity is a mix of sliding and deformation above the bed as done by Hooke et al. (1992).

5.4.3 Estimating the uncertainty in deformation derived with englacial tiltmeter

In this section we use uncertainty propagation to estimate the uncertainty in du/dz and u_d computed from englacial tiltmeters and Eqn. (6.1), as we later use in chapter 6. Starting from Eqn. (6.1), we can estimate the error in the deformation,

$$\epsilon_{du/dz} = \frac{1}{\Delta t}\frac{d\tan\theta}{d\theta}\epsilon_\theta = \frac{1}{\Delta t}(1+\tan^2\theta)\epsilon_\theta. \tag{5.6}$$

Where ϵ_θ is the maximum error we can expect in the tilt, and the other variables are as defined in Eqn. (6.1). We bound the computation of the error to the values as $\theta = 0$ and $\theta = \pi/4$ (i.e. we study the error for vertical tiltmeters, and tiltmeters at 45°),

$$\epsilon_0 = \frac{1}{\Delta t}\epsilon_\theta,\ \epsilon_{\pi/4} = 2\epsilon_0. \tag{5.7}$$

The error in the velocity can be roughly estimated as just the product of the deformation error with the thickness h over which we integrate the tilt data,

$$\epsilon_{ud} = \epsilon_{du/dz}h. \tag{5.8}$$

We show the ϵ_0 and $\epsilon_{\pi/4}$ curves for $\epsilon_\theta = 0.01° = 0.00017$ rad in Figure 5.2. An estimation of the error in the deformation velocity for the two extreme cases considered is shown 5.3. Since not all tiltmeters are at either 0 or 45°, the real line should be in between the two. However, it must be remarked that these error bounds are unrealistically high, since it is unlikely that the worst case scenario of maximum error in the tilt data is always applicable.

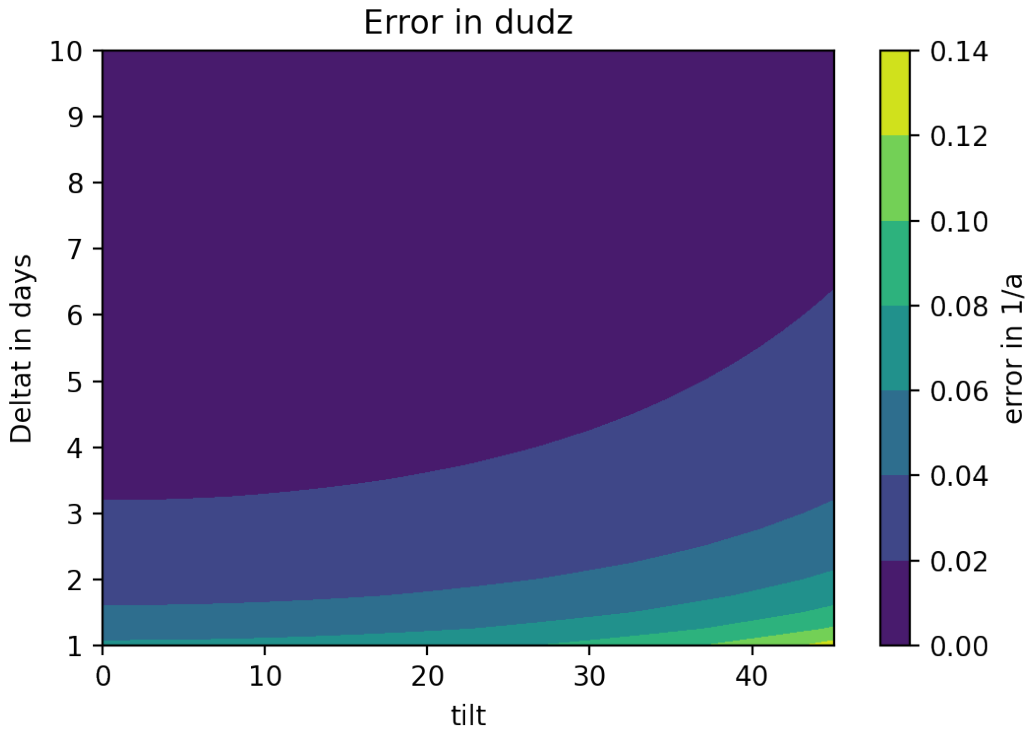

Figure 5.2: Error in the deformation. If we take the deformation every few days ($\Delta t \geq 4$,for instance) our machine error should be quite, quite low.

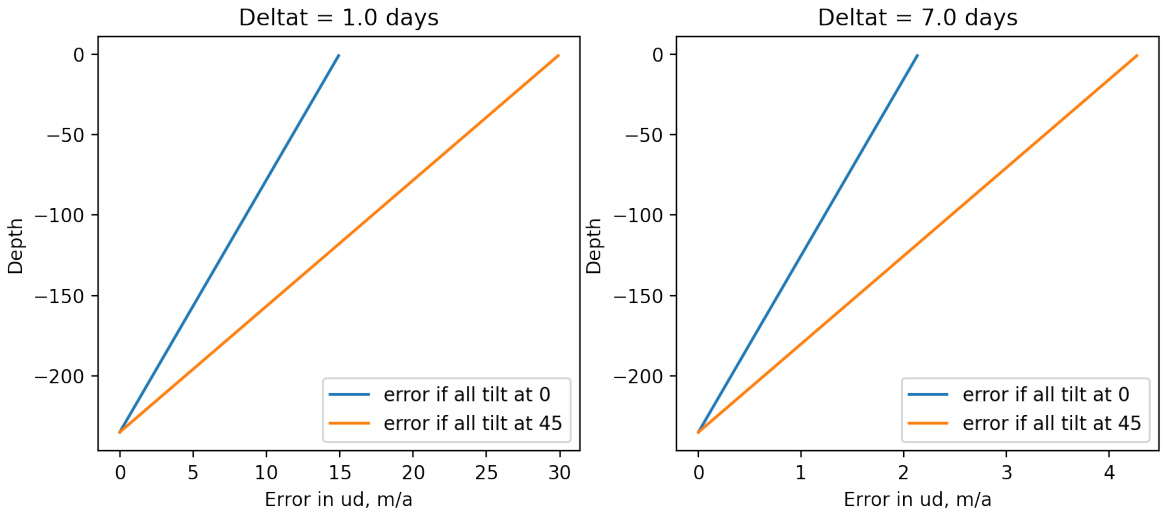

Figure 5.3: Cumulative machine error in the velocity, which is basically multiplying the dudz error by the thickness. The real value will be in between the two lines, since for half the thickness of the glacier, the tilt is almost at zero, therefore the error is minimized.

Chapter 6

Deformation, sliding and creep in Glacier d'Argentière during 2020

I had to remain on the glacier all summer. One night, the shelter where I was sleeping was blown down by a squall: I was only slightly injured, but two weeks of records were lost

Adapted from Didier Hantz' account of a borehole campaign in 1981 on Glacier d'Argentière.

Abstract

Glacier internal deformation is controlled by the ice rheology which is described by the Glen's law through two material parameters, the creep factor A and the flow law exponent n. There is great uncertainty in the values of these parameters as a result of scarce observations at the natural scale. One of the techniques that has been used to study ice deformation and constrain material properties is borehole inclinometry. We present here the results of an inclinometry study carried out at the ablation zone of Glacier d'Argentière, a temperate glacier in the French Alps. We monitored glacier deformation during 2020 with borehole-installed tiltmeters that record tilt change every 30 minutes. We are able to reconstruct the deformation rates profile with depth and the deformation velocity. Complementing our dataset with GPS-derived surface velocity, we are able to indirectly observe the basal velocity during the studied period. We infer the rheological parameters by comparing our observations with the deformation rates retrieved with a three-dimensional model solving the Stokes equation. We demonstrate that the yearly-averaged deformation rates profile has limited sensitivity to the flow law exponent n and instead mainly reflects an increase in the creep factor A with depth which could be explained with depth-increasing interstitial water content. The depth-averaged creep factor is found to be 1.5 times higher than the recommended one for temperate ice. We further show that internal ice deformation exhibits seasonal variability, such that surface velocity changes cannot be attributed solely to changes in basal conditions. At longer timescales, surface velocity variability is better explained with changes in the deformation rates, while shorter velocity variability (weeks or days) is better explained with changes in basal velocity. Further work remains to be conducted in order to confirm if the observed creep enhancement is due to depth-increasing water content, and to determine the causes behind the seasonal changes in internal deformation and basal velocity.

6.1 Introduction

Internal deformation of glaciers is a fundamental component of ice flow models, and for many mountain glaciers accounts for a high portion of total ice flow (e.g. Mathews, 1959; Paterson, 1970; Shreve and Sharp, 1970; Harper et al., 2001). However, ice deformation quantification at the natural scale is complicated due to the strong dependency on ice material properties and stress (Glen, 1955). The values of rheological parameters retrieved through laboratory experiments differ within different experiments (Cuffey and Paterson, 2010), and from those retrieved with large-scale observations (Cuffey and Paterson, 2010; Gillet-Chaulet et al., 2011; Millstein et al., 2022).

Direct observation of glacier internal deformation rates is most commonly carried out with borehole inclinometry (e.g. Hooke, 1973; Hooke et al., 1987; Gudmundsson et al., 1999; Lüthi et al., 2002; Willis et al., 2003; Ryser et al., 2014; Doyle et al., 2018; Maier et al., 2019, 2021). This technique consists in the drilling of boreholes whose deformation is then repeatedly measured, either by measuring the change of the borehole shape with time (repeated inclinometry, e.g. Perutz, 1949; Shreve and Sharp, 1970; Hooke, 1973; Hooke and Hanson, 1986) or with englacial tiltmeters which record the progressive change of inclination of the sensor (Gudmundsson et al., 1999; Lüthi et al., 2002; Willis et al., 2003; Amundson et al., 2006; Ryser et al., 2014; Keller and Blatter, 2012; Doyle et al., 2018; Lee et al., 2019; Maier et al., 2019).

Borehole inclinometry provides information about the interaction between the bed topography, the stress distribution and the internal deformation rates (Raymond, 1971; Hooke and Hanson, 1986; Ryser et al., 2014; Maier et al., 2019). Several bed-reaching borehole surveys (Ryser et al., 2014; Doyle et al., 2018; Maier et al., 2019) have shown that deformation rates dependency with depth becomes increasingly complex as we approach the bed due to basal boundary effects, with deformation maxima not located at the ice-bed interface but a certain distance above it. Some of these observations can be explained either with a combination of sticky and slippery patches over overdeepenings (Ryser et al., 2014), or with flow over a bumpy bed (Maier et al., 2019), as expected from boundary layer theory applied to hard-bed sliding (Kamb, 1970; Gudmundsson, 1997b). Borehole surveys in temperate valley glaciers detected intra-annual changes in deformation rates patterns, generally attributed to stress redistribution resulting from changes in the subglacial hydrological network (Hooke et al., 1992; Willis et al., 2003). The extent to which the detected changes in deformation rates are spatially representative of the glacier is unclear. For instance, Willis et al. (2003) found that seasonal changes in deformation rates varied greatly at distances lower than an ice thickness, suggesting that a complex subglacial hydrology system with spatially and temporally heterogeneous water pressure distribution was the cause of the disparity in deformation rates between nearby boreholes.

With the deformation rates profile known, good constrains on the stress distribution allows to directly estimate *in-situ* material parameters, such as creep factor, creep enhancement and flow exponent (Mathews, 1959; Hooke, 1973; Dahl-Jensen and Gundestrup, 1987), or at least provide constrains on them (e.g. Maier et al., 2019). Additionally, measuring the deformation rates in a glacier provides, coupled with surface velocities, an indirect measure of the basal velocity (e.g. Harper et al., 1998; Gudmundsson et al., 1999; Ryser et al., 2014; Maier et al., 2019, 2021). Given the scarce observations of ice rheology at the natural scale and basal velocities, ice flow models tend to use inversion methods to estimate the best material parameters that allow best matching the surface velocity (Vincent and Moreau, 2016; Zekollari et al., 2019; Millan et al., 2022). The problem is however largely undetermined due to multiple solutions leading to the same surface velocity field. Additional uncertainty arises from basal slip quantification, which is commonly inverted assuming known material parameters (Morlighem et al., 2013; Derkacheva et al., 2021; Maier et al., 2022), and sometimes inverted to-

gether with ice rheology (e.g. Hill et al., 2018).

In this paper, we look at deformation data of Glacier d'Argentière (French Alps) to determine its internal dynamics and measure the basal speed during 2020. We do so with a combination of observations, with the novelty of using several tiltmeter arrays permanently installed in boreholes drilled along the main flow line of the ablation area during late 2019 and 2020. This dataset constitutes the first annual record of internal deformation rates in temperate glaciers measured with tiltmeters, with previous studies (e.g. Willis et al., 2003; Amundson et al., 2006; Keller and Blatter, 2012) involving observations over much shorter time periods and with lower sensor density with depth, and other records of similar length and with high sensor density being obtained in polythermal glaciers (Ryser et al., 2014; Maier et al., 2019; Lee et al., 2019). We first describe the study site and the measurement methods. We then analyse the observation in terms of material parameters using a three dimensional ice flow model and finally provide the observed time series of both deformation and basal velocities. We finish by discussing our findings and show how our observations are consistent or not with expectations from current knowledge.

6.2 Field site and instrumentation

6.2.1 Glacier d'Argentière

Glacier d'Argentière is a temperate glacier located in the Mont Blanc range, French Alps (45°10 N, 6°10 E). The glacier rests on hard bedrock (Vivian and Bocquet, 1973) and extends for 9 km within an altitude range of 1600 m to 3400 m, separated by an icefall at an altitude of 2300 m. The dynamics of the glacier, especially in the vicinity of the drilling site, have been continuously studied since the 1970's, and since 2018 (Gimbert et al., 2021a) there is an extensive network of instruments deployed on the glacier, e.g. GPS stations, a weather station, and the cavitometer, a bicycle wheel located in a subglacial cavity under the icefall that directly measures basal velocity (Vincent and Moreau, 2016). Surface dynamics shows a seasonal pattern typical of mountain glaciers, with low velocity between September and April, followed by a period of sustained high velocity between May and August (Vincent and Moreau, 2016; Gimbert et al., 2021a; Vincent et al., 2022a). High subglacial runoff is observed during the summer period, and melt season acceleration as well as late summer deceleration is paired with fast increase and decrease of subglacial runoff, respectively.

6.2.2 Field campaign

The drilling site is located in the central part of the ablation area, between 600 and 800 m upstream of the icefall. The thickness at the center flow line of this area is about 250 - 230 m, see Figure 6.1, panel (a) and Table 6.1. The average surface speed at this location is about 47 m a^{-1} (Vincent et al., 2022a). A DEM of basal topography (black lines in Figure 6.1, panel (a)) is available with a mean uncertainty of ± 10 m (Vincent et al., 2009), and shows an over-deepening where most of the boreholes are located.

Drilling operations took place between the 12th and the 14th September, 2019. The boreholes were done with a custom-built hot water driller operating at 70°C, that drills a water-filled borehole with a 10 cm diameter at an average speed of 60 m/h. Insufficient weight of the driller head, fast drilling speeds, and intraglacial debris affected the verticality of the boreholes. In several occasions, which we attributed mostly to the presence of rocks inside the glacier (Hantz and Lliboutry, 1983), the driller head would stop advancing, enlarging the size of the borehole at the location until drilling could be resumed. On a few occasions it was not enough to resume drilling and a new location had to be chosen. There

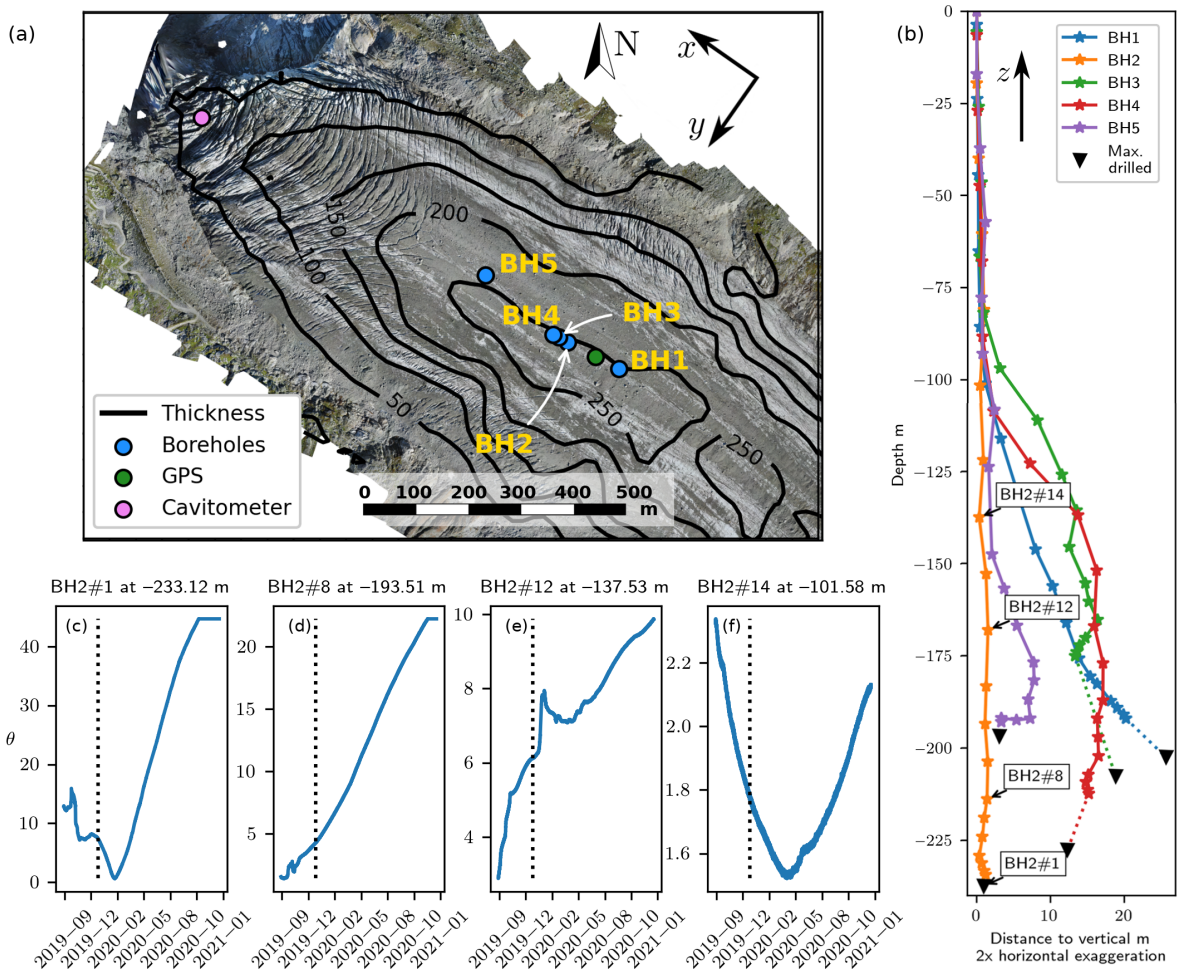

Figure 6.1: **I should add the discharge meter and the AWS** Panels showing the location of the instruments used in this study, the estimated shapes of the boreholes and some unfiltered tilt curves, and the reference system used in the study. Panel (a) shows a map of the ablation area of Glacier d'Argentière (projection EPSG:27572) with ice thickness (black contours), and instrument locations as of late September 2019. Panel (b) shows the estimated initial shape, drilled depth (black triangles) and instrumented depth (every star is a tiltmeter) of the five boreholes. Panels (c) to (f) show the tilt θ (continuous lines) recorded at four example inclinometers in BH2, between installation and January 1st 2021. In the event of sensor failure or cable snapping the data logger records the last value, hence why the curves at the end of BH2#1 and BH2#8 are flat after November 2020. The dotted vertical lines mark the 1st of January 2020, the day when we start our analysis.

Borehole	Tiltmeters	Borehole depth	Instrumented depth	Local thickness	Not instrumented
BH1	18	208	194	253±10	59±10
BH2	19	238	234	237±20	3±20
BH3	17	216	174	235±20	61±20
BH4	19	237	211	234±20	23±20
BH5	17	194	190	234±10	44±10

Table 6.1: Resume of the boreholes instrumentation and depths after installation. All distances are in m. The 'Not instrumented' column is the difference between 'Instrumented depth' and 'Local thickness', giving the estimated distance between the last tiltmeter and the bed. Local thickness for BH1 and BH5 uses GPR data (Vincent et al., 2009). Local thickness values for BH2, BH3 and BH4 are considered 20 m lower than the thickness of Vincent et al. (2009), based on the observations of Sergeant et al. (2020) in a profile close to BH4.

were instances of sudden borehole drainage, indicating that the borehole was connected with a water pathway or a crevasse. The position of the final completed and instrumented boreholes (BH1, BH2, BH3, BH4, BH5) are given in blue dots in Figure 6.1 (a). We give an estimate of the initial shape of the boreholes (Figure 6.1 (b)) calculated with tilt and azimuth data approximately one month after installation. The actual shapes are 3D curves, so we instead show the estimated horizontal distance between each inclinometer and a vertical line starting at the surface. Since not all boreholes could be instrumented in their entirety, we also show the estimated depth of each borehole with a black triangle.

6.2.3 Description of the tiltmeters

The deformation rates sensors are made of a custom printed circuit board (PCB) equipped with a high end triaxial gravity sensor (Muratta SCL3000) and a triaxial magnetic sensor (ST LSM303). Sensors are respectively connected to a micro controller (Atmega 328P) through an SPI and I2C Bus, and then soldered to the PCB. PCB production and components soldering operation was subcontracted, and then each microcontroller was programmed and calibrated in the laboratory. To withstand the pressure exerted by moving ice and water pressure the PCB was casted with an epoxy compound inside a 25mm OD aluminum tube, which we call tiltmeter. The gravity sensors are used to determine the position of the sensor with respect to its own reference system, from which we can derive the tilt θ, the angle with respect to the vertical, with an estimated accuracy of 0.01°. Lab calibration showed that tilt readings at more than $45°$ become progressively unreliable. The magnetic sensors don't provide good absolute measures of the orientation with respect to the north as a result of being very sensitive to parasite magnetic fields. For this reason, we decide not to use them except for roughly estimating the boreholes' initial shapes.

The tiltmeters are grouped together in chains of 20, more densely concentrated towards the bottom of the glacier, see Figure 6.1, panel (b). For any borehole i, we name each tiltmeter j as BHi#j starting at 1 for the deepest tiltmeter, i.e. BH2#5 is the fifth deepest tiltmeter installed in the second borehole. The piezometers were located in the last 15 m of the sensor chain. The sensors are connected to a surface unit composed of a Campbell scientific data logger (CR300), two 12V 55Ah gel batteries and a solar panel that allows for autonomous data acquisition. Communication between tiltmeters and the surface unit is done through Modbus communication protocol over half duplex RS485 serial buses. All sensors acquired data every 30 minutes.

The performance of the tiltmeter arrays varied between boreholes. The sensor array in BH1 stopped working after a few days and did not provide useful data. In BH2, all sensors recorded data for more than one year until late October 2020, when the cable snapped at an estimated depth of 220 meters,

losing the deepest 6 tiltmeters. BH3 and BH4 were drilled close to BH2, with BH3 being the shortest borehole of the whole campaign. Both BH3 and BH4 show a very crooked shape in their deepest tiltmeters, suggesting problems during drilling that affects the quality of the measurements, either by having non-vertical tiltmeters that are then too sensitive to normal strains (Keller and Blatter, 2012), or poor sensor-ice mechanical coupling as a result of too wide borehole diameter. All sensors in BH3 and BH4 worked during 2020. The sensors in BH5 stopped functioning soon after it was installed. The number of tiltmeters installed in each borehole depends on borehole depth. We provide a resume of borehole length and instrumentation in Table 6.1. Ice thickness at BH2, BH3 and BH4 is based on Sergeant et al. (2020), which suggests that DEM derived ice thickness in the vicinity of BH4 (Vincent et al., 2009) is underestimated by about 20 m. Due to BH2 reaching the bed and showing good quality data, that we attribute to the almost vertical shape of the borehole, most of the results presented in this paper correspond to BH2.

Deformation data during the first months is compromised by insufficient mechanical coupling between the tiltmeters and the ice. We illustrate this with a few representative unfiltered tilt curves in panels (c) to (f) of Figure 6.1. The tilt is given in positive values. Most sensors show an early period of noisy and seemingly random behaviour, followed by a much longer period of steady tilt evolution. The time at which the transition between noisy and steady tilt change happens varies from sensor to sensor, but for most of the tiltmeters it happens before the 1st of January 2020, marked with the vertical dotted lines. Some sensors, like BH2#1 or BH2#14 attain their minimum tilt after September 2019, indicating they were initially tilting against the flow, therefore correcting their position with time. Others, like BH#8 have their minimum at, or just after, installation. Other sensors like BH2#12 show more erratic even after the January 1st 2020, possibly indicating bad mechanical coupling to the ice. Note the difference in tilt magnitude at the different depths in Figure 6.1: BH2#1 has a total change of tilt of about 60°, BH2#8 of about 25°, while BH#14 tilt change is lower than 5°. To avoid accounting for the early behaviour in some sensors, we start our analysis the first of January 2020, 15 weeks after installation. We removed high frequency noise by smoothing the tilt data using an exponential filter with a one day time constant. This filtering mostly affects short term observations, and has a negligible effect on long term (i.e. weekly or monthly averages) analysis.

6.2.4 GNSS Network and surface velocity

We used multi-frequency Leica GR25 receivers and Leica AS10 antennas that continuously registered GPS signals at a 1 s sampling interval. The GPS antennas are mounted on the aluminum masts initially anchored up to 6 m deep in the ice. Regular (weekly to every few months) field visits ensure the upright position of the antenna masts and continuous power supply.

GPS phase observables were processed in kinematic mode using TRACK software (Chen, 1999) that incorporates double-differencing techniques to eliminate phase biases caused by drifts in the satellite and receiver clock oscillators (Chen, 1999; Herring et al., 2018). The position of survey sites was determined with respect to a reference station that sits on the bedrock approximately 3 km apart. On such a short baseline, the ionospheric errors cancel in a single differencing such that L1 and L2 can be treated as two independent observables (Schaffrin and Bock, 1988; King, 2004). In addition, Glacier d'Argentière appears to have a poor scattering environment that causes large phase residuals at elevations up to 25°above the horizon; therefore, we used a 25°elevation cutoff angle as opposed to commonly used 10°(Herring et al., 2018). The average root-mean-square (RMS) residual of the position time series at each 30 s epoch is ± 5 mm, and the epoch-to-epoch standard deviation of horizontal and vertical position estimates is approximately ± 3 mm and ± 5 mm, respectively.

We calculated horizontal velocities from the position time series smoothed using a Gaussian low-pass filter with an 18-hour sliding window. This window length was chosen by referencing to the unfiltered 4-hour static-derived velocities (King, 2004), and it appears to work best to attenuate high-frequency noise in the position time series and retrieve short-term variations in the glacier velocity. Since estimation of the actual velocity uncertainties associated with the filtered positions is impossible, we determined it empirically by deploying during two weeks another station on the moraine, approximately half a km apart from the boreholes and 3 km away from the reference station. We estimate the uncertainty in the surface velocity is ± 0.5 mm h^{-1}, equivalent to ± 4.4 m a^{-1}.

6.3 Methods

6.3.1 Internal deformation rates computed from observations

We approximate the internal deformation rates du/dz from the temporal evolution of the tilt θ, (Lüthi et al., 2002; Ryser et al., 2014; Doyle et al., 2018; Maier et al., 2019),

$$\frac{du}{dz} = \frac{1}{dt}\frac{dx}{dz} \approx \frac{1}{\Delta t}\Delta \arctan\theta, \tag{6.1}$$

where Δt is a given time period and $\Delta \arctan\theta$ is the change in the arc tangent of tilt during that time period. We use a three dimensional reference system with x the main along flow direction, and z the upwards vertical with origin at the surface (see panels (a) and (b) of Figure 6.1). Velocities in x, y and z directions are denoted by u, v and W, respectively. In our particular implementation, we calculate at every Δt the least squares linear approximation of $\arctan\theta(t)$, such that the slope gives directly du/dz. For this method we consider that all θ is in the direction of flow. We also consider that the only non-zero component of the velocity gradient tensor is du/dz. This hypothesis will be later tested with a three dimensional numerical model of the glacier. For every tilt value we use $\Delta t = 1$ day. The estimated maximum uncertainty for the daily averaged deformation rates are, for most of the sensors lower than 0.1 a^{-1}, more details in the supporting information S7. We test the validity of neglecting the flow gradient tensor components du/dx and dw/dz in our analysis of the tilt curves using the analytical solution of tilt evolution given in Keller and Blatter (2012) for steady flow contained in a vertical plane undergoing shear du/dz and extension (or compression) in the along-flow and vertical directions, du/dx, dw/dz. We will also use this model to test the error made upon considering that all tiltmeters are in the flow directions **to be done**.

The deformation velocity between two tiltmeters i and j is computed by numerically integrating the deformation rates,

$$u_d(t,i,j) = \int_{z_i}^{z_j} \frac{du}{dz} dz \approx \sum_{j+1}^{i} \frac{1}{2\Delta t} \left(\Delta \arctan\theta(z_i) + \Delta \arctan\theta(z_{i-1})\right)(z_i - z_{i-1}). \tag{6.2}$$

6.3.2 Modeled deformation rates

Our observations allow us to infer the strain-rate tensor. However, determining the rheology of the ice at Glacier d'Argentière requires constraining the stress tensor τ_{ij}. For this purpose we use a three dimensional numerical model of Glacier d'Argentière, similar to the model used by Gimbert et al. (2021a) and Vincent et al. (2022a), using the FEM Elmer/Ice (Gagliardini et al., 2013). The model solves the Stokes equation without approximation for a glacier geometry given by the measured bedrock

and surface topography and is used to extract the stress and deformation rates profile along the boreholes. Ice rheology is given by the Glen's flow law:

$$\dot{\varepsilon}_{ij} = A\tau_E^{n-1}\tau_{ij}, \tag{6.3}$$

where $\dot{\varepsilon}_{ij}$ and τ_{ij} are respectively the components of the strain rate (a^{-1}) and deviatoric stress tensors (MPa), A is the creep factor (a^{-1} MPa^{-n}), $\tau_E = \frac{1}{2}\tau_{ij}\tau_{ij}$ the effective stress (MPa) and n the Glen's exponent.

We assume a stress-free surface boundary condition and a basal boundary condition given by a Weertman (1957) type friction law,

$$A_s\tau_b^m = u_b, \tag{6.4}$$

where τ_b is the basal shear stress (MPa), m an exponent taken equal to 3, A_s is the friction coefficient at the bed (m a^{-1} MPa^{-m}) taken constant in time, uniform in space, and u_b the sliding velocity (m a^{-1}). We run several simulations to test the sensitivity of the deformation rates profile to different rheologies. We run a set of simulations with different Glen's flow law exponents $n = 3, 4, 5$ and constant and uniform creep factor A. The value of A is chosen such that the numerically computed total deformation velocity at the initial location of BH2 is equal to the deformation velocity u_d averaged for the 1st January to 15th October 2020 period. We run as well a simulation with $n = 3$ and depth-inverted creep factor $A = A(z)$, such that the computed deformation rates du/dz is as close to the observations as possible.

In addition, we compare the high-order Elmer/Ice model to a simplified plane-strain model, commonly referred as Shallow Ice Approximation (SIA). Assuming that all deformation is a result of linearly increasing shear stress due to gravity on an inclined valley τ_{xz}, we obtain the following deformation rates profile at the center line of the glacier (Nye, 1965),

$$\frac{du}{dz} = 2A(f\rho_i g\alpha|z|)^n. \tag{6.5}$$

Ice density is given by ρ_i, g is gravitational acceleration, α is the average slope of the glacier, and shape factor f takes into account the reduction in stress at the center line due to lateral drag. We will consider two cases, $f = 1$ (no reduction in stress at the center), and $f = 0.646$, the suitable value for a parabolic valley with a half-width to thickness ratio of 2 (Nye, 1965), a reasonable approximation of the cross section of Glacier d'Argentière at the studied site, see supplementary information S1.

6.3.3 Analytical model of boundary layer flow

Some studies of ice flow around hard beds show that a boundary layer with important flow gradients develop around the bed bumps (Kamb, 1970; Gudmundsson, 1997a,b), with maximum deformation rates attained a certain distance above the bed, not inmediately at the ice-bed interface. Similar conclusions have been derived by Ryser et al. (2014) and Maier et al. (2019) upon analyzing deformation rates profiles. In our case, our Elmer/Ice model parameterizes this near-bed process with the friction law, and therefore it cannot be used to provide an accurate description of the flow close to Glacier d'Argentière's bed. For this purpose, we will compare our observations with an analytically derived deformation rate profile close to the bed.

We simulate the flow around bed bumps using the analytical solution for the two dimensional flow of a linear medium sliding over a sinusoidal bed of low roughness given by Gudmundsson (1997b). We compute the analytical solution for the first 10 m above the bed, using local slope $\varepsilon = 0.5$, glacier

thickness $h = 250$ m, and wavenumber $k = 1$, and neglecting regelation. The obtained flow gradient are used to generate one year of synthetic tilt curves, using the forward model of tilt evolution presented in Gudmundsson et al. (1999). We then compute the corresponding averaged deformation rates using Eqn. (6.1), and compare the behaviour with our observations. The results are given in the supplementary materials.

6.4 Results

6.4.1 Observed deformation rates profile

Deformation rates profiles at BH2, BH3 and BH4 averaged between the 1st January and the 15th October 2020, are shown in Figure 6.2. The shaded region cover the range of monthly-averaged deformation rates, computed using Eqn. (6.1). Starting with BH2, we divide our profile in three parts. The upper part, spanning the uppermost 100 m, has very noisy deformation rates (e.g. BH2#19, BH3#17 to 16, BH4#19 to 16) except at a few tiltmeters (such as BH2#18). In this layer, we expect negligible shearing deformation rates and thus weak contribution to the internal dynamics of the glacier. The middle part, which we consider from -100 m until -219 m, has much higher deformation rates, which we attribute mainly to shearing. Deformation rates increases non-linearly towards the bed, from less than 0.01 a^{-1} at -100 m to 0.64 a^{-1} at -219 m in BH2#6. The lowest part is the basal layer, which registers the highest deformation rates of the profile and extends from -219 m until -235 m (the bed). The profile at this part breaks the depth-increasing trend of the deformation rates profile. We observe a sudden decrease in deformation rates of roughly 0.25 a^{-1} around between -220 and -230 m, followed by a more than three times increase in du/dz between -230 m and -235 m. The decrease represents a 40% of the deformation rates at BH2 over 10 m (from 0.64 a^{-1} at BH2#6 to 0.40 a^{-1} at BH2#4). We hypothesize that this behaviour indicates the presence of the boundary layer expected in hard bed sliding, with the maximum deformation rate being in the vicinity of BH2#1. The thickness of such boundary layer is approximately 18 m at BH2 if we consider it starts at BH2#6 (3 m between the bed and BH2#1, and 15 m between BH2#1 and BH2#6). This profile is consistent with sliding over a rough hard bed, as we show in S7. The averaged profile in BH3 and BH4 is, in general terms, similar to that of BH2.

We comment now a few outliers and particularities of the profiles given in Figure 6.3. The high and noisy deformation rates recovered in a few tiltmeters of the upper part of the glacier (e.g. BH2#19, BH3#17, BH4#19) is most probably due to the tiltmeter remaining almost vertical under negligible deformation rates. As such, small changes in θ over a short period of time (due to environmental unaccounted factors such as rain entering the borehole) yield, relative to the low θ recorded by the sensor, very high deformation rates. Therefore we omit BH2#19, BH3#15 to BH3#17 and BH4#16 to BH4#19 in our analysis. In the middle part of the glacier, we find strong temporal variability in BH3#6 and BH4#8, at -160 m and -181 m respectively. The recorded tilt at BH3#6 shows strong changes from June 2020 onwards suggesting decoupling from the ice, and the tiltmeter at BH4#8 is always tilting at more than 45°, which is beyond the range of tilt in which the tiltmeters provide reliable data. Moreover, these tiltmeters were located at those points where we estimated sudden changes in the direction of the borehole (see the estimated deviation with respect to the vertical in Figure 6.1 (b)) such that we can expect an enlarged borehole section and bad sensor-ice coupling. In the lowest part of the glacier, the deformation rates measured at tiltmeters BH4#1 to BH4#6 is consistently lower than at BH2. However, when comparing the tilt curves provided in the supporting informations S5, we observe that the tilt curves captured by BH4#1 to BH4#6 are not smooth and continuously increasing as those in BH2. Indeed, between BH4#1 and BH4#6 we see weeks long periods with almost no change in tilt,

which results in very low deformation rates. Therefore, it is unclear whether the differences in the lowermost deformation rates between BH2 and BH4 are due to differences in the strain field, or an artifact of poor drilling conditions at the bottom of BH4 (recall that the last 20 m of BH4 could not be instrumented after drilling). Given that BH2 presents the least noisy data, reached the bed, and that it is the only borehole where the whole thickness was instrumented, we focus on BH2 for the rest of the paper.

6.4.2 Comparison with a modeled deformation rates profile

We now try to reproduce with our three dimensional Elmer/Ice model of Glacier d'Argentière the mean $du/dz(z)$ profile at BH2. Simulations with constant creep factor and different values of the Glen's law exponent yield deformation rates profiles with much less curvature than observed, represented by the blue continuous curves in of Figure 6.3 (a). The modeled deformation rates profiles at constant A show poor sensitivity to the flow exponent ($n = 3$, $n = 4$ and $n = 5$). In Figure 6.3 (b) we show the shear stress components (τ_{xz}, τ_{yz}, τ_{xy}) and the effective deviatoric stress (τ_E) for the simulation with depth dependent creep factor, to be compared to the SIA (Eqn. (6.5)). The full stress tensor as well as the results for the other simulations can be found in the supporting information S6, but it is rather insensitive to changes in the rheological parameters. It can be seen that ice flow is dominated by along flow shear in the deeper half of the glacier ($\tau_{xz} \approx \tau_E$), and by a mix of shear and extension or compression in the upper half of the glacier (τ_{xz}, τ_{yz} and τ_{xy} are clearly lower than τ_E, but non-zero). The across flow horizontal shear τ_{xy} is always lower than along flow shear, except close to the surface where they attain similar values. This distribution of stresses allows us to validate the use of equation (6.1) for computing du/dz. In the middle and lower part of the ice column τ_{xz} dominates over the other shear components, and over the upper part of the ice column du/dz is negligible, such that the influence of other stress components on du/dz will be low as well in absolute terms. With regards to the stress given by the plane strain model (SIA), the dotted lines in Figure 6.3 (b), we see that despite not being able to reproduce the depth distribution of simulated stresses, the basal drag τ_b (identical to the value of τ_E at the bottom of the ice column) predicted by Eqn. (6.5) for a glacier of similar cross section as Glacier d'Argentière (blue dotted line) is almost identical to the basal drag computed by the Elmer/Ice model. If the shape factor is not accounted for (the green dotted line), τ_b is overestimated by more than 50%.

The only configuration that provides a good match between observations and the numerical results is the depth-dependent creep factor, whose deformation rates profile is plotted for the case $n = 3$ in dashed lines in panel (a) of Figure 6.3. To find the creep factor as a function of depth, we infer A by inverting Glen's law (Eqn. (6.3)) with the observed mean du/dz at BH2 and the numerical stress tensor,

$$A(z) = 2\frac{du}{dz}\tau_{E,num}^{-2}\tau_{xz,num}^{-1}. \tag{6.6}$$

We then approximate $A(z)$ by a piece wise linear function. Given that changing the creep factor slightly modifies the overall stress balance, we run the numerical model repeatedly, updating at each iteration the $A(z)$ inferred with the numerical solution of the previous iteration, until the modeled stress field converges. The results are shown in Figure 6.3: the deformation rates profile is given in dashed lines in panel (a), and the inferred creep factor is given in panel (c), stars and continuous black line, bottom horizontal axis. The deformation rates recovered in the boundary layer is not reproduced by the numerical model.

Focusing on panel (c) of Figure 6.3, we see that in the upper half of the glacier $A(z)$ is close to

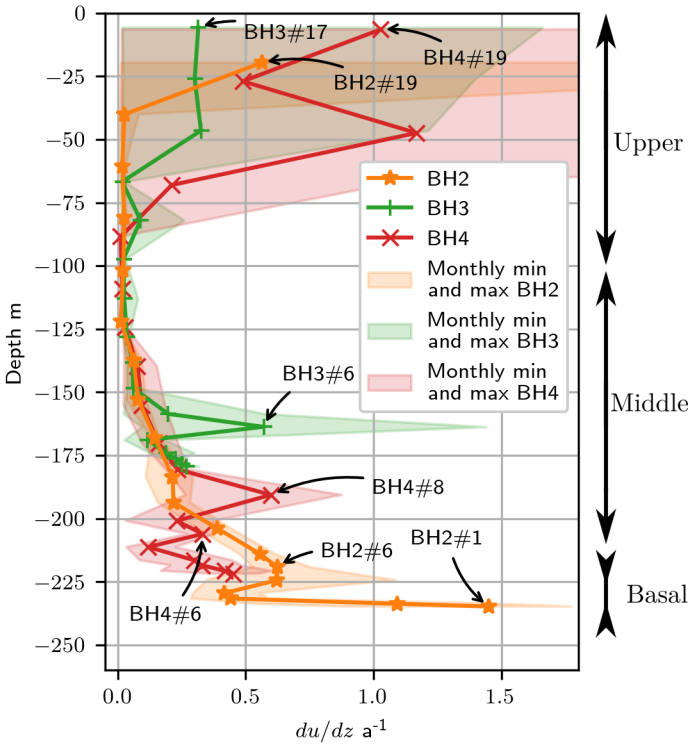

Figure 6.2: Deformation rates profiles with monthly minima and maxima at BH2, BH3 and BH4. The continuous lines show the average measured deformation rates at each borehole for the period between the 1st January and the 15th October, and the shadowed region the range between monthly averaged minima and maxima deformation rates values. Every symbol represents a tiltmeter. We point with arrows some tiltmeters to help understand the main text.

78 MPa^{-3}a^{-1} (see dotted line), the value proposed by Cuffey and Paterson (2010) for temperate ice and $n = 3$. From -140 m down to the bed A increases non linearly, such that A becomes closer to the value proposed by Paterson (1994) (dashed line).

6.4.3 Seasonal evolution of velocity

In this section we study temporal changes in deformation at Glacier d'Argentière, the inferred basal velocity and the relationship between deformation velocity and surface velocity and water discharge.

Figure 6.4 shows the hydrology (panel (a), precipitation and discharge) and the timeseries of velocities (panel (b)) at Glacier d'Argentière, during the 2020 February - Mid October period. Discharge and precipitation are shown in daily averages. The given velocities are the surface velocity at the GPS station u_s in green, the deformation velocity at BH2 u_d in blue, the inferred basal velocity u_b in black, and the basal speed measured at the cavitometer u_{cav} in red. The continuous solid lines on the lower panel show weekly averages of each velocity, while the semitransparent curves represent daily velocities.

Surface and deformation velocity have similar seasonal behaviour: both accelerate between February and May, then stay at higher values until September, and decline until mid October. This pattern is broken at the daily and weekly scale by short-term accelerations. Some of these accelerations are detected simultaneously by the GPS and the tiltmeters, see for instance the accelerations in early July and early, mid and late August. Others, specially fast surface accelerations (late March, mid May, mid July, late August) are not observed in both datasets. As a result, the inferred basal velocities at BH2,

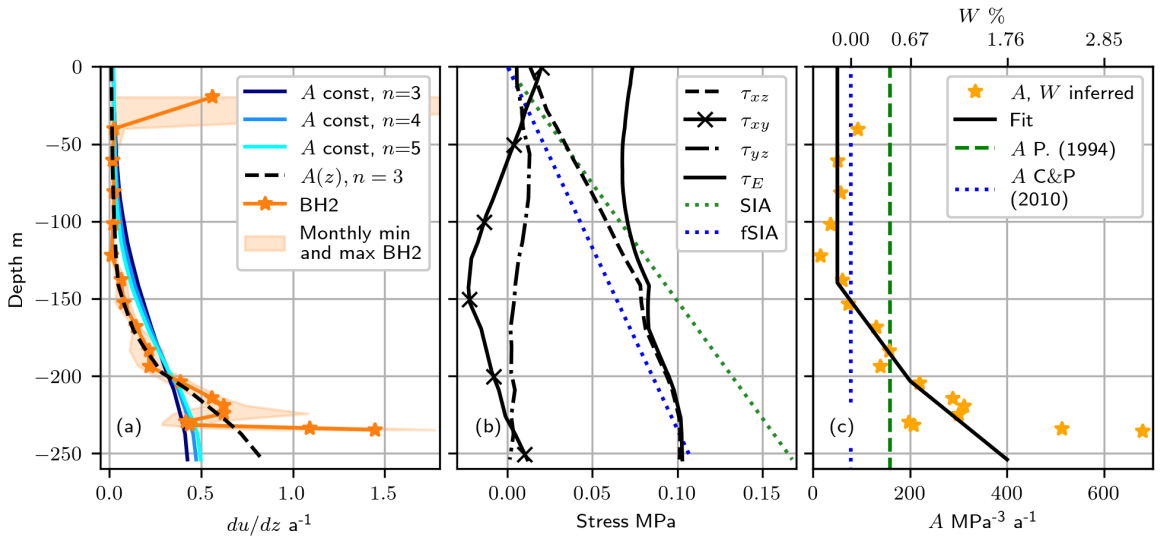

Figure 6.3: Observed and computed deformation rates profile at BH2 and other results from the numerical simulations. Panel (a) compares the observed profile at BH2 with the numerically computed deformation rates profiles. The numerical profiles are selected for four representative scenarios, with uniform creep factor $A = A_0$ and $n = 3$, $n = 4$, and $n = 5$, and with depth-variable creep factor $A = A(z)$ and $n = 3$. Panel (b) shows the vertical profile of effective and shear stress, as well as a comparison with the stress given by the SIA assuming shape factor $f = 1$ for the green dotted line, and $f = 0.646$ (Nye, 1965, parabolic channel with $W = 2$). Panel (c) shows the creep factor (bottom horizontal axis) inferred as a result of constraining the simulation with the average deformation rates profile at BH2, and the inferred water content inferred from the observed creep (top horizontal axis). The green dashed line marks the value of A for temperate ice proposed by Paterson (1994), and the blue dotted line marks the value of A proposed by Cuffey and Paterson (2010).

which is the residual component of the surface velocity, shows dual behaviour. On one hand, seasonal changes in surface velocities seem unrelated to basal velocities. On the other, short changes in surface velocities must be explained with basal accelerations. Average velocities during the February - Mid October period are $\bar{u}_s = 47$ m a^{-1}, $\bar{u}_d = 32$ m a^{-1}, $\bar{u}_b = 18$ m a^{-1} and $\bar{u}_{cav} = 55$ m a^{-1}. The basal speed at the cavitometer u_{cav} is markedly different from the basal velocity at BH2. At the seasonal scale, u_{cav} has strong seasonality, with a clear maximum in early July.

We explore in better detail the relationship between velocities, to discern how correlated deformation and surface velocities are. For that, we compute the correlation between deformation rates du/dz and surface velocity u_s using eight different averaging periods: from eight-weeks to one-week averages, one week decreasing each time. For each length of the averaging period, we perform a linear regression between du/dz and u_s and compute the correlation R^2 and the p-value. We show a resume of the regressions in Figure 6.5, where colors show the correlation coefficient (R^2, see the color bar) and the text shows the p-value. Longer averaging periods mean there are less points to compare data to, thus outliers become more important and some correlations may become, while strong, less significant. This is particularly well seen when comparing eight-weeks averages with seven-weeks averages: the eight-weeks averages have only one data-point less than the seven-weeks one, just enough for some correlations to become non-significant. The individual regressions are given in S10.

We find strong significant correlation ($R^2 > 0.5, p < 0.05$) between deformation rates and surface velocities in several of the tiltmeters below -200 m for several averaging periods. The correlation between du/dz and u_s decreases if we compare shorter averaging periods, but the spatial pattern of significant correlation is, for the most part, preserved, i.e. most of the tiltmeters below -200 m tend to record stronger deformation rates when surface velocities are high, and lower deformation

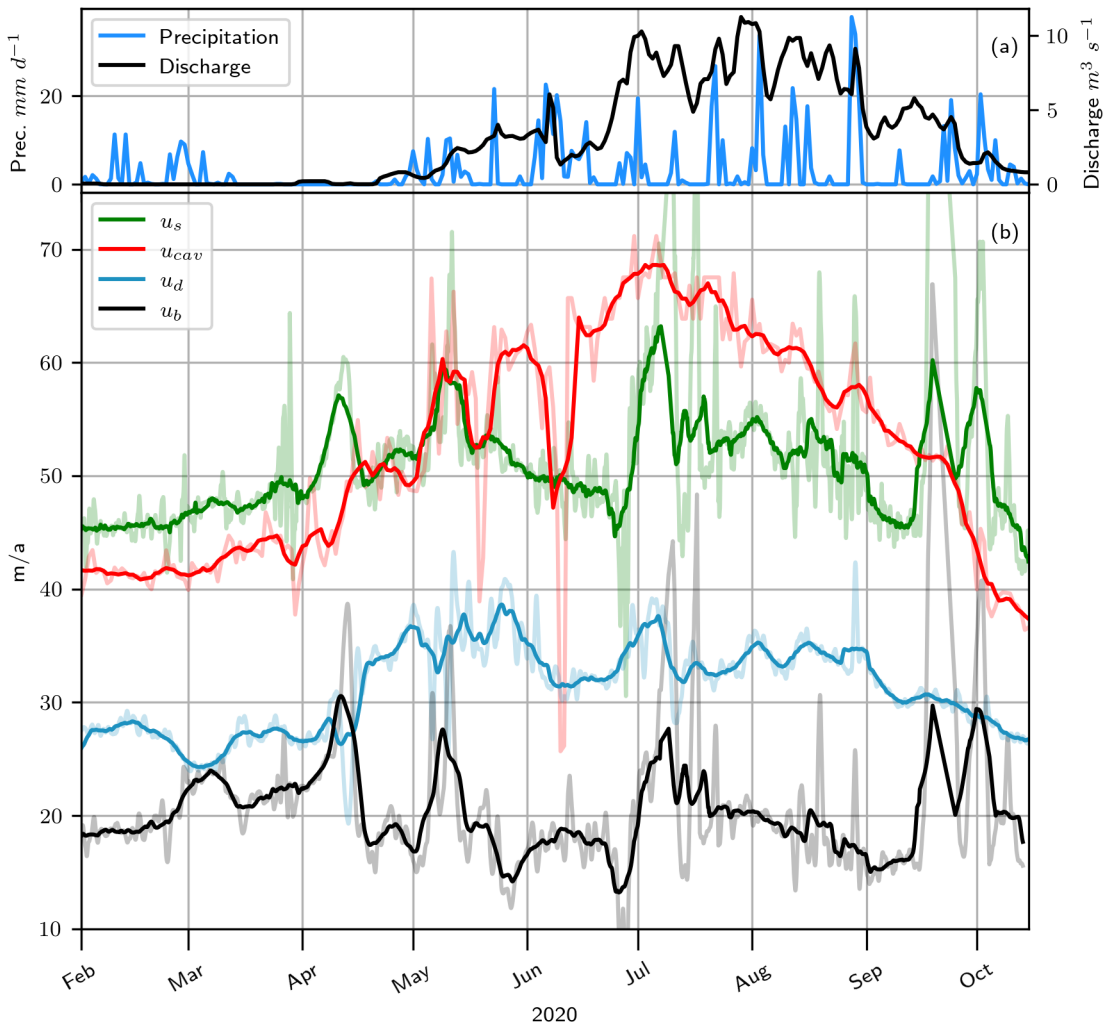

Figure 6.4: Timeseries of surface velocity u_s, sliding velocity at the cavitometer u_{cav}, deformation velocity at BH2 u_d and inferred basal velocity at BH2 u_b. Solid lines show weekly averages of the velocities, while the semitransparent lines in the background show daily values.

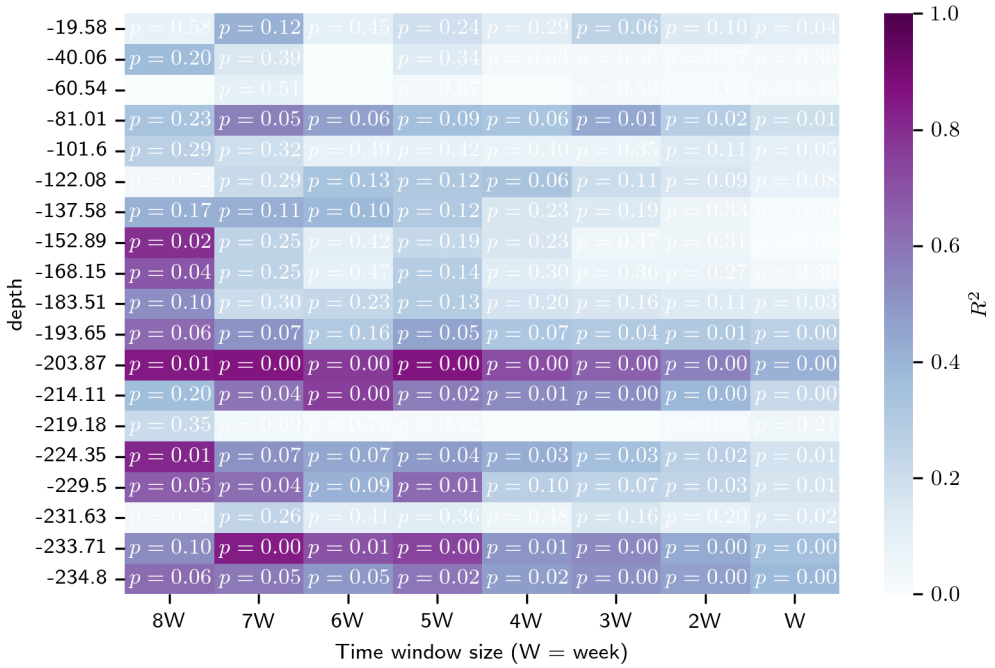

Figure 6.5: In-depth distribution of the correlations between deformation rates at BH2 du/dz with surface velocity u_s averaged at different averaging periods, computed with linear regressions. Color shows the R^2 and the text the p-value of the regressions.

rates when surface velocities are low. The strongest value in each averaging period (darkest colors in each column) is always located at -204 m (BH2#8). Depending on the size of the averaging period, the correlation between deformation rates and surface velocities appear high or low. This is seen for $BH\#10, BH\#11$ and $BH\#12$, between -183 and -152 m, who are only correlated with surface velocities if we consider eight weeks averages.

6.5 Discussion

6.5.1 Evaluating the deformation profile

Implications for rheological parameters

The observed deformation could not be reproduced with the numerical model that used uniform creep factor and common values of the Glen's law exponent. Moreover, since the retrieved stress tensor was largely independent on n and A, it seems that the spatial distribution of stresses within Glacier d'Argentière is set by the glacier geometry, and not by rheological parameters. Indeed, direct application of the SIA to the averaged deformation observed in BH2, BH3 and BH4 provides an apparent exponent of $n = 4.73$, much softer than typically considered when modelling mountain glaciers (Vincent and Moreau, 2016; Zekollari et al., 2019; Millan et al., 2022), and softer as well than the $m = 3.38 \pm 0.42$ found by Gimbert et al. (2021c) in their long term assessment of sliding at Glacier d'Argentière, if we assume that sliding is solely due to creep around bed obstacles, and not regelation.

In the case of temperate ice, this depth increasing creep factor may be due to interstitial water content W (Duval, 1977; Adams et al., 2021). We test this hypothesis with the formula proposed by Duval (1977). We adapt it considering $A = 78$ MPa^{-3}a^{-1} (Cuffey and Paterson, 2010) when $W = 0$, i.e. we

assume no water content in the upper half of the glacier, obtaining

$$W = \frac{1}{2.34}\left(\frac{A}{78} - 1\right), \tag{6.7}$$

for W in % and A in MPa^{-3} a^{-1}. The inferred water content values are given in the top horizontal axis of Figure 6.3 (c). Discarding the negative values as artifacts of our chosen parameterization of Duval's model, we see that the expected water content above -219 m ranges between 0 and 1.5%, increasing down to the bed. Below this depth, the rapid increase in creep factor at the basal layers is explained with up to $W > 3\%$ at the base. These values of W are comparable to those observed in temperate ice (Pettersson et al., 2004), and depth-increasing water content have been previously reported in a few temperate glaciers (Vallon et al., 1976; Murray et al., 2000; Benjumea et al., 2003; Hubbard et al., 2003; Murray et al., 2007).

There are two comments to be made to this result. Firstly, Lliboutry and Duval (1985) report no relationship of W with depth through analysis of an ice core obtained in Glacier d'Argentière in a location close to our boreholes (Hantz and Lliboutry, 1983). However, the engineers and researchers that performed the measurements deem them untrustworthy (Paul Duval, personal communication) except perhaps for the higher values of W (Michel Vallon, personnal communication). We wanted to discuss this dataset since these measurements have appeared before in well cited compilations of observations of interstitial water content (e.g. Pettersson et al., 2004; Cuffey and Paterson, 2010). Secondly, our inversion for the water content is based on the work of Duval (1977), for shearing of temperate ice in tertiary creep with water contents up to 0.8%. Recently, Adams et al. (2021) found in similar experiments that ice under secondary creep with $W > 0.6\%$ is linear viscous, which corresponds roughly to the ice below -200 m. However, it is unclear if the results for secondary creep apply for the case of Glacier d'Argentière which is most likely deforming under tertiary creep (Lliboutry and Duval, 1985).

Other factors could explain the inferred depth-increasing creep. One possibility is depth-decreasing grain size (Cuffey and Paterson, 2010). In this sense, Vallon et al. (1976) reported no discernible change in grain size in the accumulation zone of La Mer de Glace, and a marked decrease in grain size at its bed close to the tongue. If the texture of Glacier d'Argentière and la Mer de Glace are comparable (both glaciers are next to each other), grain size does not seem to explain creep enhancement, except perhaps for the increased deformation near the base. Given that we expect the ice at these depths to undergo tertiary creep, we discard anisotropy as an explanation for the inferred creep enhancement (Lliboutry and Duval, 1985).

Limitations of the numerical model

The results are based on the implicit assumption that the numerical stress tensor is representative of the actual stress at Glacier d'Argentière. We consider that the distribution of stresses has a few features that can be expected in a valley glacier. Firstly, the drag at the base coincides with the expected drag if we take into account the valley shape, the thickness at the studied site and the surface slope. Secondly, the numerical model considers significant extension and compression stresses in the upper part of the glacier, that then become negligible close to the base. Such results are also realistic, and comparable with the assumption oftentimes made in glacier modeling that τ_{xx}, τ_{yy} and τ_{zz} decrease linearly towards the bed (Hooke, 2005).

Since we didn't find significant changes in the stress tensor when considering different rheologies, we question the choice of the boundary conditions. The model is run in a steady state, such that

using a friction law like Weertman (1957), which cannot accurately reproduce intra-annual changes in velocity (Lliboutry and Duval, 1985) is not that problematic. A more important choice is the uniform friction parameter A_s. A similar comparison between basal conditions was carried out in Vincent et al. (2022a), see Figure S3 of the supporting information (Vincent et al., 2022b). The results using uniform A_s and inverted viscosity were comparable with those presented in the main text that used inverted A_s and uniform viscosity, suggesting that the numerical results presented in this paper are not that dependent on the spatial distribution of the friction parameter.

Identification of the boundary layer

The shape of the deformation profile and the retrieved values of du/dx close to the bed suggested a boundary layer below -219 m. It is likely a result of the observations being part of basal processes at the meso-scale, either due to a combination of slippery and sticky patches as in Ryser et al. (2014) (our numerical model assumes uniform slippery bed and thus does not consider this origin) or due to sliding over a bump as in Maier et al. (2019) (see S7). We qualitatively confirmed the vialibility of the second option with our upslope simulated profile in Figure S12. There a few caveats to our synthetic profiles of deformation, which we address now. The modeled profiles are meant for linear ice, i.e. with Glen's law exponent $n = 1$, and they depend on the location at the bed that we consider, as well as the initial conditions and the parameters we used for the analytical model of Gudmundsson (1997b). Indeed, the analytical model assumes low roughness, given by $\varepsilon \ll 1$, while we used $\varepsilon = 0.5$ since otherwise we retrieve negligible deformation rates. However, the influence of a hard rough bed over deformation rates profiles with comparable shapes as those found by us has been shown before by Ryser et al. (2014) and Maier et al. (2019), in relatively simple experiments and considering non-linear ice. Thus, we conclude that it is likely that the observed profile close to the bed corresponds to the basal boundary layer (perhaps indicating that the base of the borehole is located in the lee side of a bump), and that our estimated deformation at this location is influenced by the neglected components of the velocity gradient.

6.5.2 Seasonal changes in velocity

We saw in Figure 6.4 that the deformation velocity changes through time, and that its temporal evolution is, as we observed in Figure 6.5, similar to the surface velocity at several time-scales. We interpret that the correlations between du/dz and u_s show that surface velocity is partly controlled by deformation velocity, specially at the lower part of the bed. Lower correlation at shorter time-scales could reflect that short term changes in surface velocities are a result of basal accelerations, with deformation velocity controlling seasonal (monthly to multimonthly) changes in glacier dynamics.

We estimate the increase in deformation velocity during the melt season is 20%, from roughly 28 m a^{-1} before the melt season, to 35 m a^{-1}, which are attained or surpassed for more than one month between May and the end of September.

Assuming that these observations at BH2 are representative of its surroundings, we will consider two possible origins for the 20% difference between winter and summer. First we will study seasonal changes in stress, and then seasonal changes in the creep factor through evolving water content. In any case we can't discard a combination of the described mechanisms, operating at different timescales to provide the observed deformation.

Local versus global control on ice deformation

The summer increase in deformation can originate from an increase in drag at the base (Hooke et al., 1992; Maier et al., 2021), which, applying Glen's flow law with $n = 3$, yields an increase in stress of the order of $\Delta\tau = \Delta\dot{\varepsilon}^{1/3} \approx 6\%$. We will consider two origins for this seasonally evolving stress, increased ice-bed contact area as a result of channelization (Hooke et al., 1992; Willis et al., 2003), and ice flow over increasingly steep bed bumps (Maier et al., 2021).

Nanni et al. (2021) estimated that during May 2019 the subglacial water at our study site transitions from a distributed system to a channelized one, with a main subglacial drainage channel running very close to the position of our boreholes. The transition happened at the beginning of the melt season, which usually takes place in May (Vincent and Moreau, 2016). The combination of these observations with the pressure record at BH2 (see Figure S9), suggests a very active, well connected subglacial system between, at least, May and August, with the greatest variability during June. This conclusion is exactly the opposite conclusion given in Vincent et al. (2022a), where it was estimated that cavities occupy an extensive portion of the bed along the central flow line during summer. However, Vincent et al. (2022a) used the cavitometer velocity as a proxy for the basal velocity at the ablation zone (see Figure 6.4) which behaves very differently from the basal velocity at BH2.

Both Nanni et al. (2021) and Vincent et al. (2022a) are not necessarily observing contradictory behaviours. The central part of glacier d'Argentière could undergo some channelization during the melt season, until July, in the sense of having a main drainage axis in the central part of the glacier. This flow concentration does not mean that there are no cavities in the system, as they can appear at (relatively) low sliding velocities over realistic beds (Helanow et al., 2021). At the end of June, the system must switch state. Between July and September, the high deformation velocity, decrease in basal velocity, and high discharge point out to channelization during this period, with increased ice-bed coupling and drainage efficiency. The collapse of channels during September could be indicated by the progressive decline in deformation velocity. This is supported by the two big surface accelerations that happen in the second half of September and beginning of October, coincidental with strong storms. By this time, the hydrology system is not efficient anymore, and the system cannot deal with punctual strong water input. **these two last sentences will have to be reviewed once we use the new dataset of Anuar**

We cannot discard, also, that the seasonal changes in deformation rates are local due to differences in bed topography. Following the short analysis of the profile close to the bed, we could estimate that from March to August the bottom of BH2 is going over the stoss side of an increasingly steep bump. This cannot explain, however, why surface velocities are well correlated with boreholes in the deeper part of Glacier d'Argentière.

Change in water content

Here we test the extent with which the expected production of water from the glacier deformation is sufficient to cause seasonal changes in water content that would explain seasonal changes in internal deformation. We discarded the percolation of surface water through the ice as an origin of such changes in water content, because Glacier d'Argentière can be considered impermeable above -100 m (Hantz and Lliboutry, 1983).

Using Duval (1977) and assuming an average water content $W = 0.7\%$, roughly the average value retrieved between -150 and -235 m (see Figure 6.3). If we consider internal generation due to strain heating, we must consider as well the evacuation of the water at the end of the high strain period

to return to winter values. For the evacuation, we assume that ice permeability below 100 m is not negligible and consider the upper limit for clean, coarse ice given by Raymond and Harrison (1975), $q_{clear} = 0.008$ m a^{-1}. Assuming that the changes happen during a three month period Δt_w (decreasing during September, October and November), the necessary flux is $\Delta w/(100\Delta t_w) \approx 0.0056$ m a^{-1}, of the same order as expected. The last remaining question is if that ice water content can actually be produced. For that, we will compute the upper limit of water production through strain heating using maximum values of stress and strain. We consider just above the boundary layer, all strain given by $du/dz = 1$ a^{-1}, the maximum value during summer at BH2#6, and $\sigma_{xz} = \sigma_E = 0.1$ MPa, the expected stress at the base. For a latent fusion heat of $L_f = 0.336$ MJ/kg, the water generation due to ice shearing horizontally is (Cuffey and Paterson, 2010)

$$\dot{b}_E = \frac{\sigma_{xz} du/dz}{2L_f} = 0.15 \text{ kg a}^{-1} \text{ m}^{-3}. \tag{6.8}$$

Relative to the mass of ice, this is equivalent to $W = \dot{b}_E/(\rho_i) = 0.00017$, or 0.017%. The maximum strain heating produced is one order of magnitude lower than required.

In conclusion, the observations at the seasonal scale cannot be explained neither with the transport of surface water through the ice due to the presence of impermeable bubbly ice close to the surface, nor with strain heating due to insufficient water generation.

6.6 Conclusions

We have measured internal deformation along the central line of the ablation area of an alpine temperate glacier. Our data provided good spatial resolution at three different boreholes, which allows us to reconstruct the deformation profile and its evolution during most of 2020, including the melt season in its entirety. A complementary numerical model was used to improve our understanding of the stress conditions at our site, and an analytical model provided additional insights on the shape of our profile near the base. We identify three different behaviours along the ice thickness. The upper 100 m of ice shows negligible deformation, with the stress field being a mix of shearing and normal stresses. The deformation between -100 m and -219 m is characterized by depth-increasing deformation due to a combination of depth-increasing horizontal shearing and creep factor. Reasonable levels of depth-increasing water content can explain the inferred creep factor. Complementary evidence should clear out if the enhanced creep is a result of water content or other factor such as ice texture. The deepest part of the ice column is identified with the boundary layer expected in hard bed sliding. Our data shows seasonally evolving deformation in Glacier d'Argentière, with internal acceleration between the beginning of the melt season in May 2020 and a decrease starting in September 2020. The evolution of the deformation velocity is well correlated to the evolution of the surface velocity at multimonthly and multiweekly periods. Short surface accelerations seem related to changes in basal speed, which stays relatively low during periods of sustained fast surface velocity. It is yet unclear if the observed dynamics are local or representative of the global behaviour of Glacier d'Argentière, as they could reflect the seasonal evolution of the subglacial hydrology system or differences in local basal topography.

All data used in this article and the code to process it can be accessed through the long-term repository SAUSSURE, in *address*

Contributions JP. Roldán-Blasco processed most of the tilt data. L. Piard designed the tiltmeters, directed the field campaign and performed early analysis on the data. A. Gilbert built the numerical model. L. Piard, A. Gilbert, F. Gimbert, C. Vincent and O. Gagliardini participated in the inclinometry field campaign and together with JP. Roldán-Blasco analysed the data, while A. Togaibekov and A. Walpersdorf provided the GPS measurements and velocity timeseries. N. Maier assisted in the modeling of deformation. All authors contributed to the discussion.

Chapter 7

Inclinometry on the right side of Glacier d'Argentière, 2021

7.1 Introduction

The preliminary results of the 2019 inclinometry campaign were considered a partial success. On the positive side, it was proven that the method for determining the internal deformation worked. The sensors were reliable, at least for computing the tilt, and the temporal evolution of deformation was an interesting phenomenon that deserved more attention. The basal velocity was successfully retrieved at BH2, and it showed that our initial ideas about the dynamics at Glacier d'Argentière maybe were not as accurate as we could have expected. On the negative side, the across borehole spatial coverage was insufficient. As chapter 6 discusses, it did not allow us to precisely determine if the deformation profile and its temporal evolution were local features of the flow field, or representative of the ablation zone. Likewise, having only one bed-reaching borehole limited our conclusions regarding the basal motion, which was one of the driving questions of the whole project. Having the necessary human and economical resources at our disposal, it was decided that the campaign should be repeated again in late summer 2021. The timing was on the limit. Earlier in the year was impossible, as it takes a lot of time to properly build, assemble and calibrate the sensors. Later in 2021 was difficult, as the closer to winter, the more difficult it is to work on the glacier, specially due to the decreasing light and deteriorating meteorology. Doing it in 2022 was unfeasible for administrative issues, and also, because then the dataset would arrive too late for my PhD. In such a case it was likely that we wouldn't be able to profit from my expertise acquired while working on the first campaign, and it could also (potentially) be too late to improve the results of the 2019 campaign. As the reader will have noticed, there is no mention of the 2021 campaign in chapter 6. We'll soon see why...

7.2 Changes in the instrumentation and field campaign

The field methods were improved with respect to the first campaign:

- To avoid drilling problems, the drilling speed was reduced by half.
- The boreholes were drilled in two groups of two, so as to compare the data within each group, and between groups. If two boreholes only a few meters apart showed very similar deformation

Borehole	Tiltmeters	Piezo.	Depth	Thickness	Not instrumented	Days
BH11	20	No	188	±20	±20	106
BH12	25	Yes	191	±20	±20	137
BH13	20	No	164	±20	±20	5
BH14	20	Yes	162	±20	±20	248

Table 7.1: Resume of the 2021 borehole campaign on the right side of Glacier d'Argentière. The 'Not instrumented' column is the difference between 'Borehole depth' and 'Local thickness', giving the estimated distance between the last tiltmeter and the bed. Local thickness uses GPR data (Vincent et al., 2009). All distances are in m. The 'Days' column gives number of days between installation and the first permanent tiltmeter failure recorded in the borehole, typically that of the first tiltmeter, and most probably due to cable snapping.

profiles, then we could be sure that the retrieved deformation was at least representative of that position.

- The boreholes would be carefully measured after drilling to ensure their verticality, and only instrumented if they did not deviate much from the vertical, and reached the bed.
- The distribution of tiltmeters was also altered. No tiltmeters were put in the uppermost 50 m of the whole array, and the density was increased towards the base. We compare the 2019 and 2021 tiltmeter distributions in Figure 7.1.
- We discarded the use of magnetometers, given that they were considered unreliable. Five tiltmeters with magnetometers that we retrieved from the 2019 campaign were installed in BH12, named BH12#21, BH12#22, BH12#23, BH12#24 and BH12#25.
- There was one piezometer per group of boreholes, one in BH12 and one in BH14.

The field campaign started the 21 of September, 2021. Drilling along the center line was much more difficult that anticipated, and no boreholes could be completed the first two days of the campaign. The boreholes were then moved to the right side of the glacier, where the ice was expected to be much cleaner of debris, but about 80 m thinner. The final and the planned positions of the boreholes are shown in Figure 7.2. All boreholes reached the bed. We provide a resume of the campaign in Table 7.1.

The boreholes were quite vertical, but lasted different periods. BH11 stopped working the 7th January 2022, and 1/3 of the data is compromised due to non-steady movement of the tiltmeters during November as seen in Figure 7.3. BH12 lost tiltmeters BH12#1 through BH12#15 and BH12#21 to BH12#25, which correspond to the lower 30% of the glacier thickness, the 17 of February, 2022. BH13 had some malfunctioning component and did not work as expected, failing the 28th September, 2021. BH14 tilt records have almost no gaps until the 27th May, 2022. From this date onward, the records show intermittent data gaps, with permanent failure of BH14#1 to BH14#12 since the beginning of June 2022. For all these reasons, I will only describe the tilt evolution recorded at BH14, from the 15th October 2021 to the 27th May 2022.

7.3 Results

7.3.1 Tilt curves

We show the three sets of tilt curves in Figures 7.3 though 7.5. The estimated depth at each tiltmeter is written inside every legend. The top left shows BHj#1, the one at the bottom of the borehole, and most likely a few 2 to 3 meters above the bed. The bottom right is BHj#20. We will describe now a few features of the tilt recorded at boreholes 12 and 14.

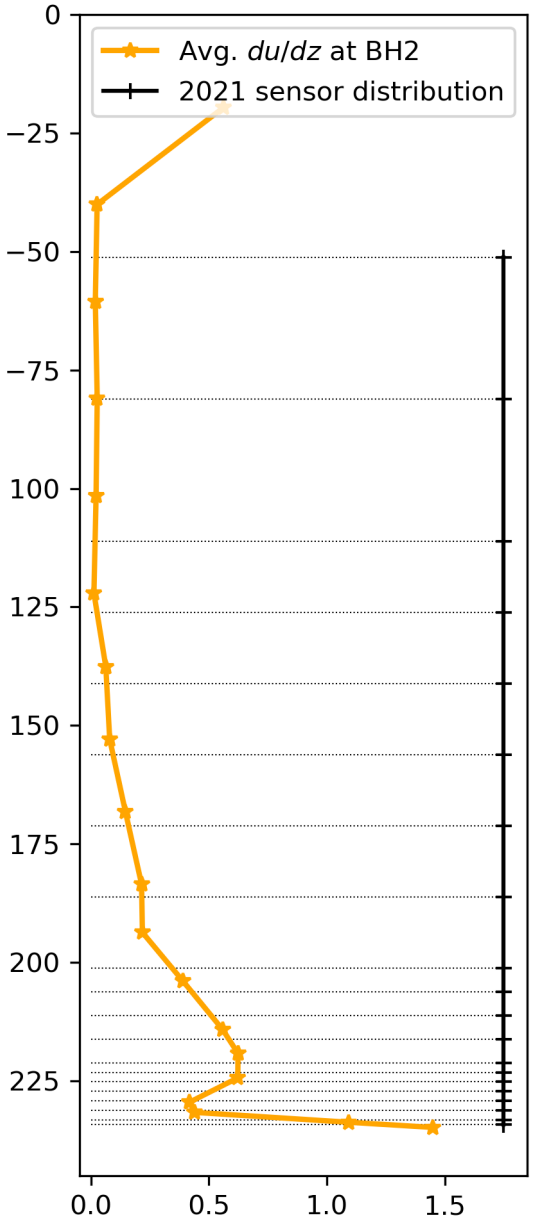

Figure 7.1: New distribution of sensors for the 2021 campaign. **I have to merge this graph with the map**

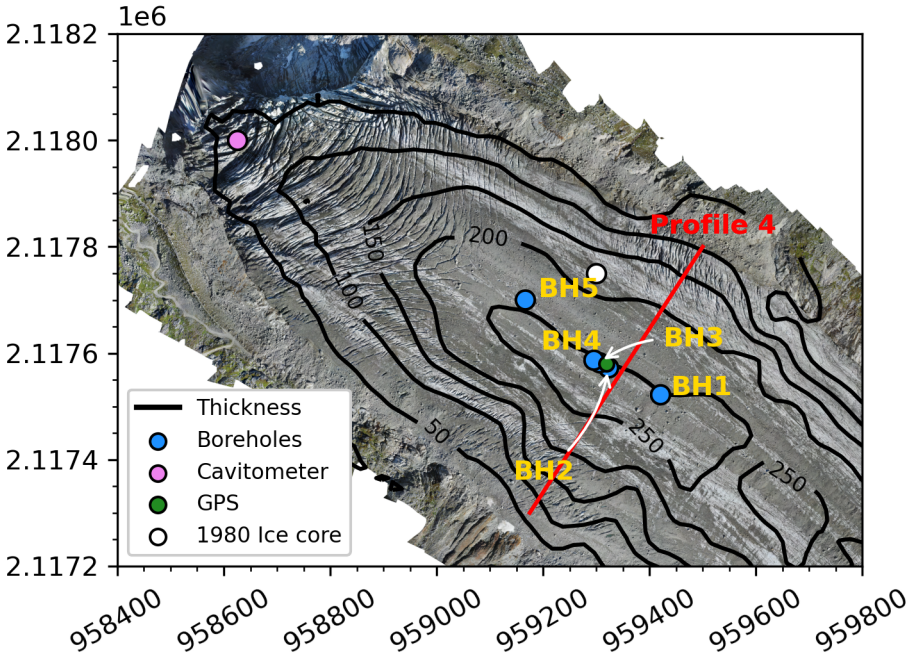

Figure 7.2: Have to be updated when somebody gives me the GPS coordinates of the new boreholes :)

BH12#1 must have some malfunction, since its tilts varies rapidly between 70°and 0°. It will be diretly discarded. Sensors between -188 m and -169 m, corresponding to tiltmeters BH12#2 to BH12#8 and BH12#21 to BH12#25, record an absolute tilt change of between 5°and 8°, showing a layer approximately 20 m thick with similar deformation rates. From -165 m (BH12#9) up to -135#m (BH12#15), the tilt curves do not show any particular period of fast tilt change, and register an absolute tilt change of around 2°and 3°. Above -135 m, where tiltmeters worked until June 2022, tilt curves are slightly more complicated.

250 upstream, the behaviour of the tilt sensors is not very much different. BH14#1 and BH14#2 don't have the smooth tilt evolution that was observed in BH2, and rather show several periods of fast tilt change (whenever we see a peak in the tilt curve). Tilt evolution is relatively stable between BH14#3 and BH14#11, indicating the presence of a 30 m thick layer of ice that deforms at the same rate. These tiltmeters record a change in tilt $\Delta\theta$ of about 12°to 8 °, and except for BH14#11, they were installed in the flow direction, such that the minimum tilt was attained at (or shortly after) installation. From BH14#12 ($z = -122.5$ m) upwards the tilt curves become more complicated and less smooth. This could indicate either poor coupling, or changes in the stress tensor. BH14#20 stayed outside of the glacier, so it will not be included in the analysis.

7.3.2 Averaged deformation profile

The method for computing the du/dz profiles and their normalized standard deviation is the same as done for BH2.

Figure 7.6 show the computed deformation profile at BH12 between the 1st October 2021 and the 17th February 2022 (left panel), and the deformation profile at BH14, averaged between the 1st November 2021 and the 9th June 2022, on the right panel.

Both profiles can be divided in two parts. The upper part is characterised by low deformation with high temporal variability, as shown by the standard deviation, which is larger than 0.6 for most of the

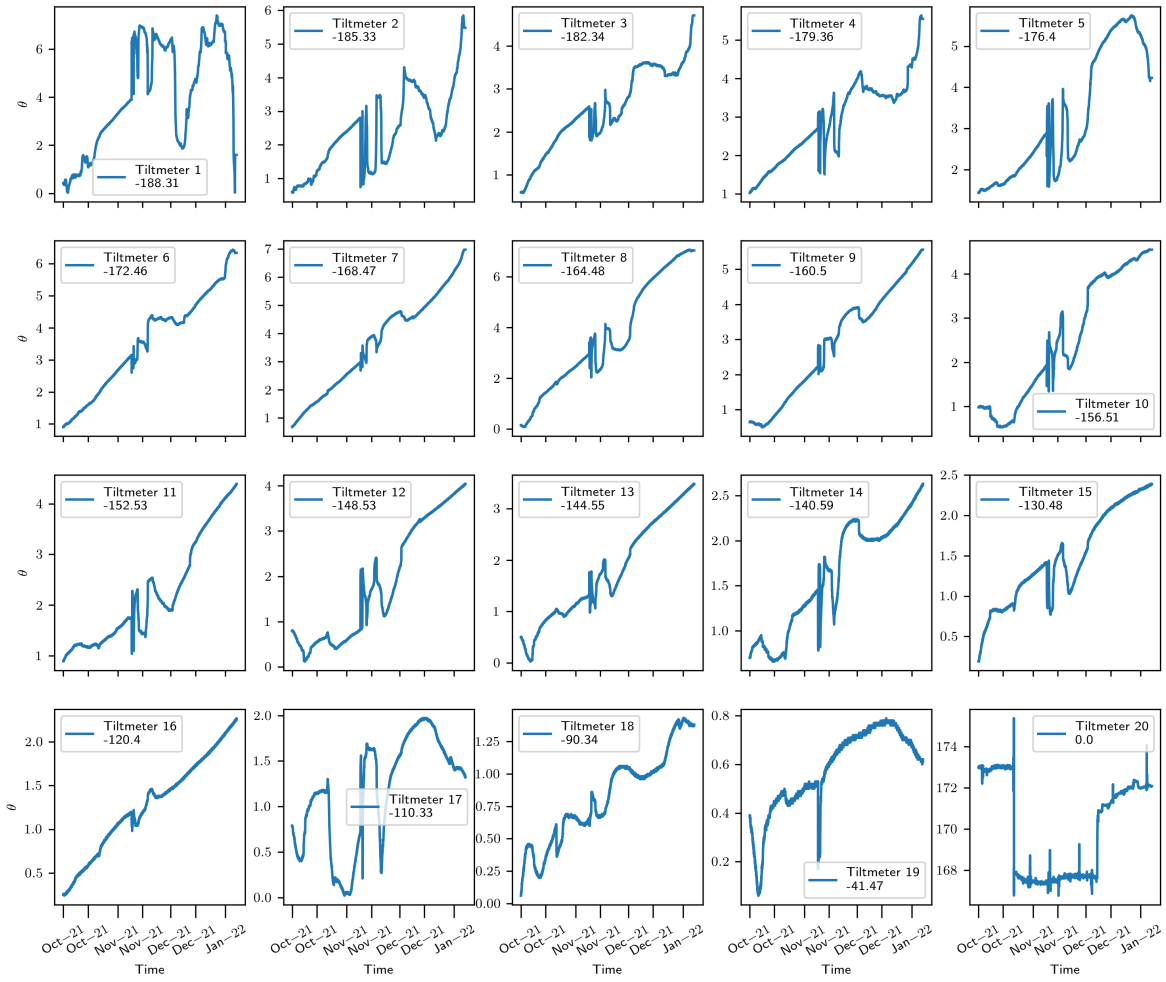

Figure 7.3: Tilt curves at BH11. Note that the timeseries ends in January 2022.

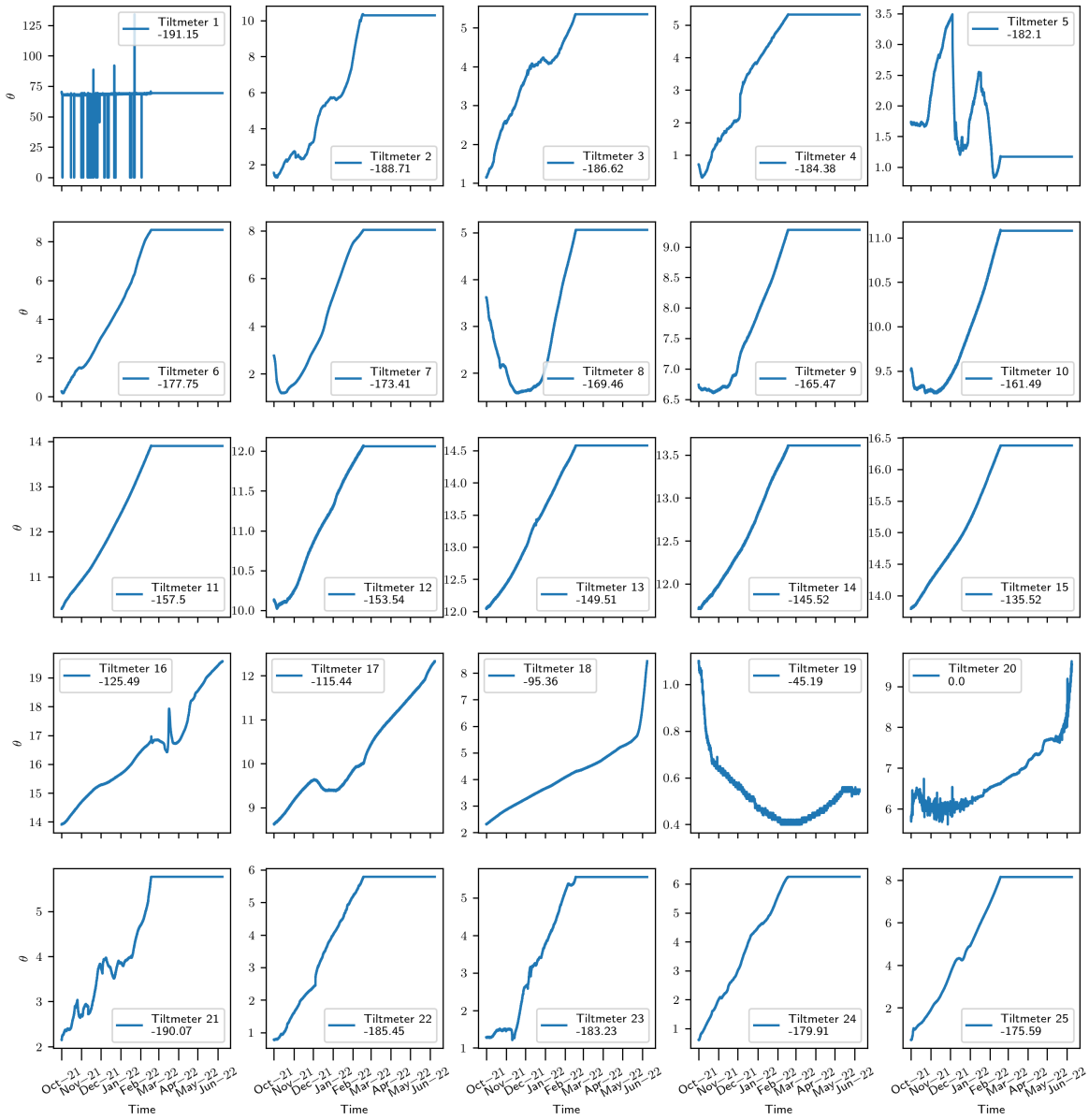

Figure 7.4: Tilt curves at BH12. Note that tiltmeters 21 to 25 are located in between tiltmeter 1 and tiltmeter 7

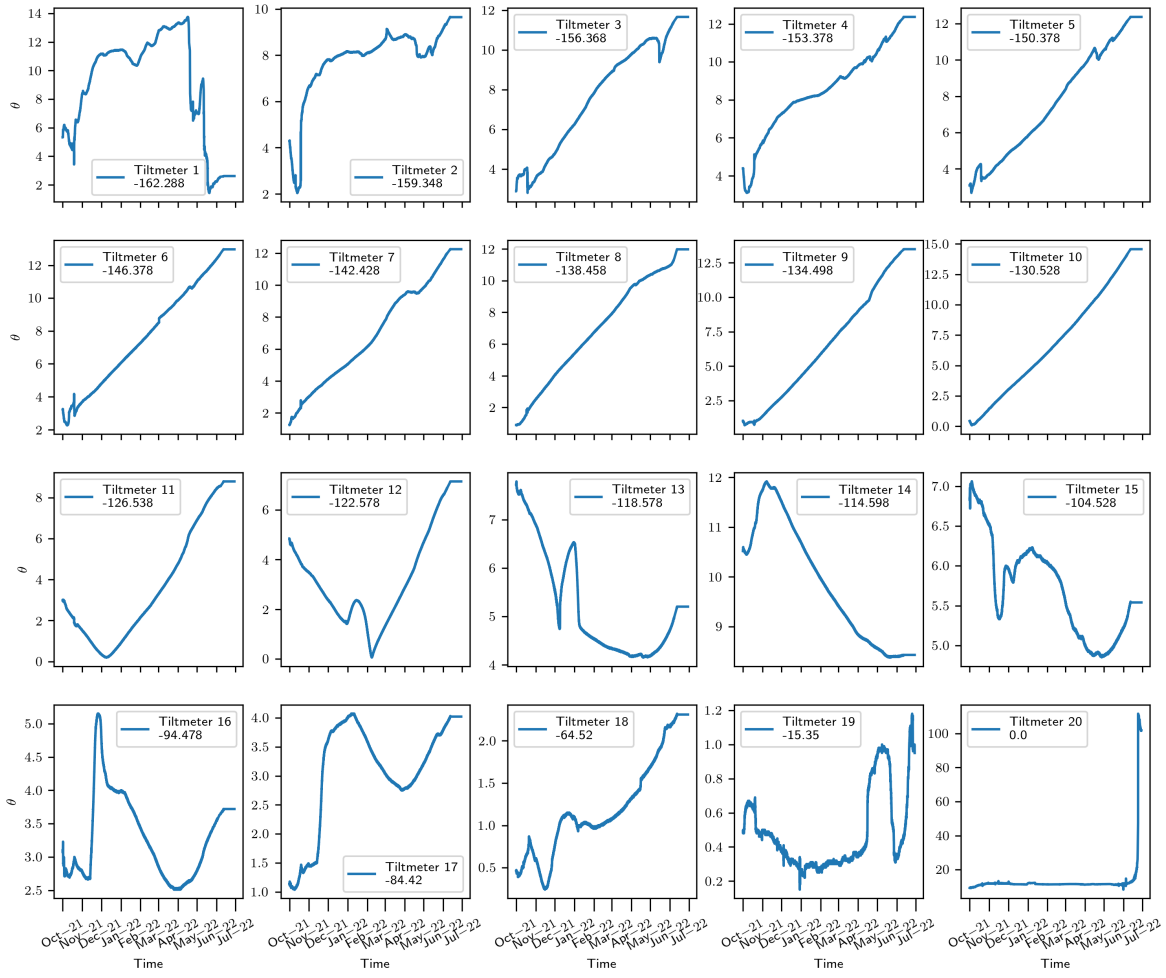

Figure 7.5: Tilt curves at BH14.

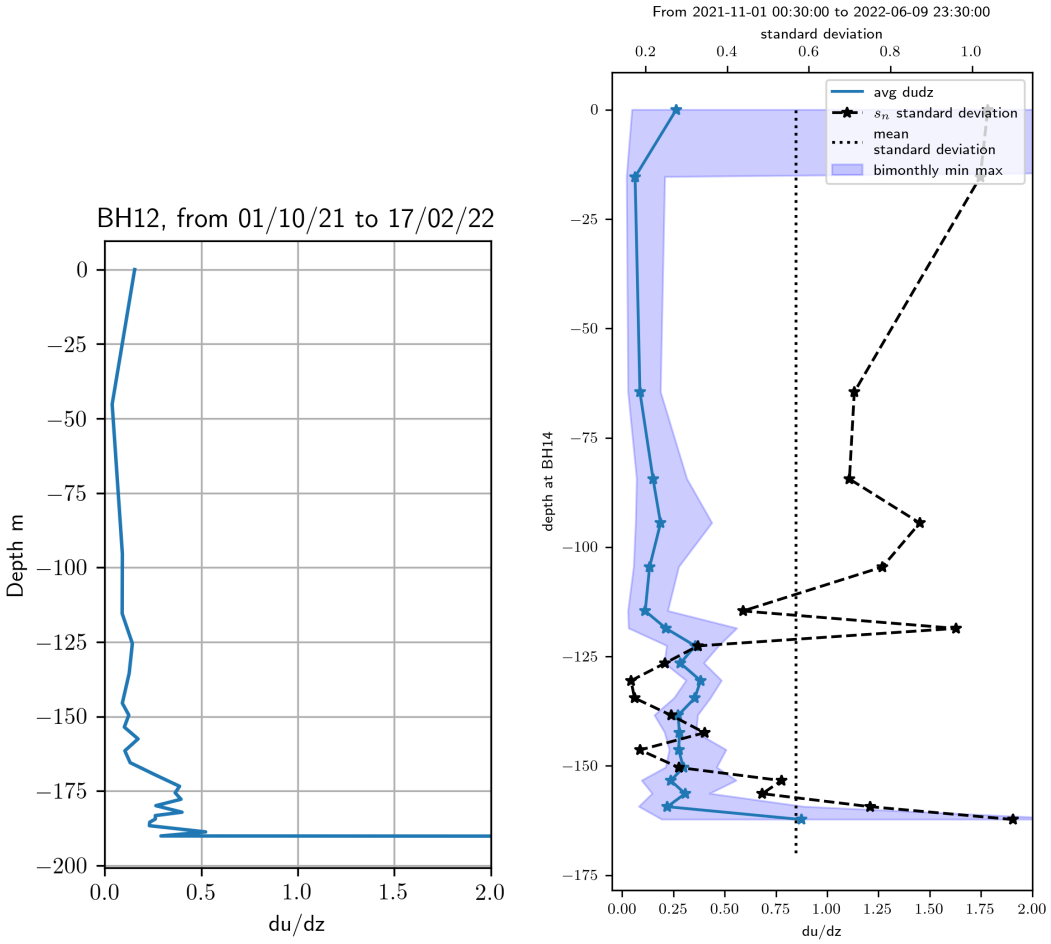

Figure 7.6: Deformation profiles at BH12 and BH14 with the standard deviation at every tiltmeter. **hacer mas pequenyo, meter la std en BH12, poner los graficos a escala**

sensors. It covers the uppermost 175 m in BH12, and the uppermost 125 m in BH14. The lower part with a layer of relatively stable deformation rates of 0.3 to 0.4 m a^{-1}. This part is approximately 20 m thick in BH12, and 30 m thick in BH14. We cannot know for certain what happens immediately above the bed. The wildly variable tilt recorded by BH12#1 (shown in Figure 7.4) could be due to being in contact with the bed. In the case of BH14, we can see in Figure **??**BH14#1, and BH14#2 record high deformation, and have higher temporal variability than the rest of the tiltmeters located in the layer of stable deformation. Recalling the discussion about the boundary layer at BH2 (in chapter 6, this behaviour at BH14 can be a reflection of a deformation state dominated by $\dot{\varepsilon}_{xx}$ and $\dot{\varepsilon}_{zz}$ (and perhaps $\dot{\varepsilon}_{yy}$), and not by shearing.

7.3.3 Bimonthly changes in deformation and velocity

We show in Figure 7.7 the differences in du/dz between the average of the full studied period, and the average du/dz every two-months period. Because the total time is made of 7 months, the last period comprises only 1 month, between the 3rd May and the 9th June.

It seems like there is a mild seasonality in deformation, with slightly larger deformation after March than in the precedent months. The magnitude of the changes in the middle part (up to 0.1 a^{-1}) are of the same order than in the middle part of BH2, see Figure **??**.

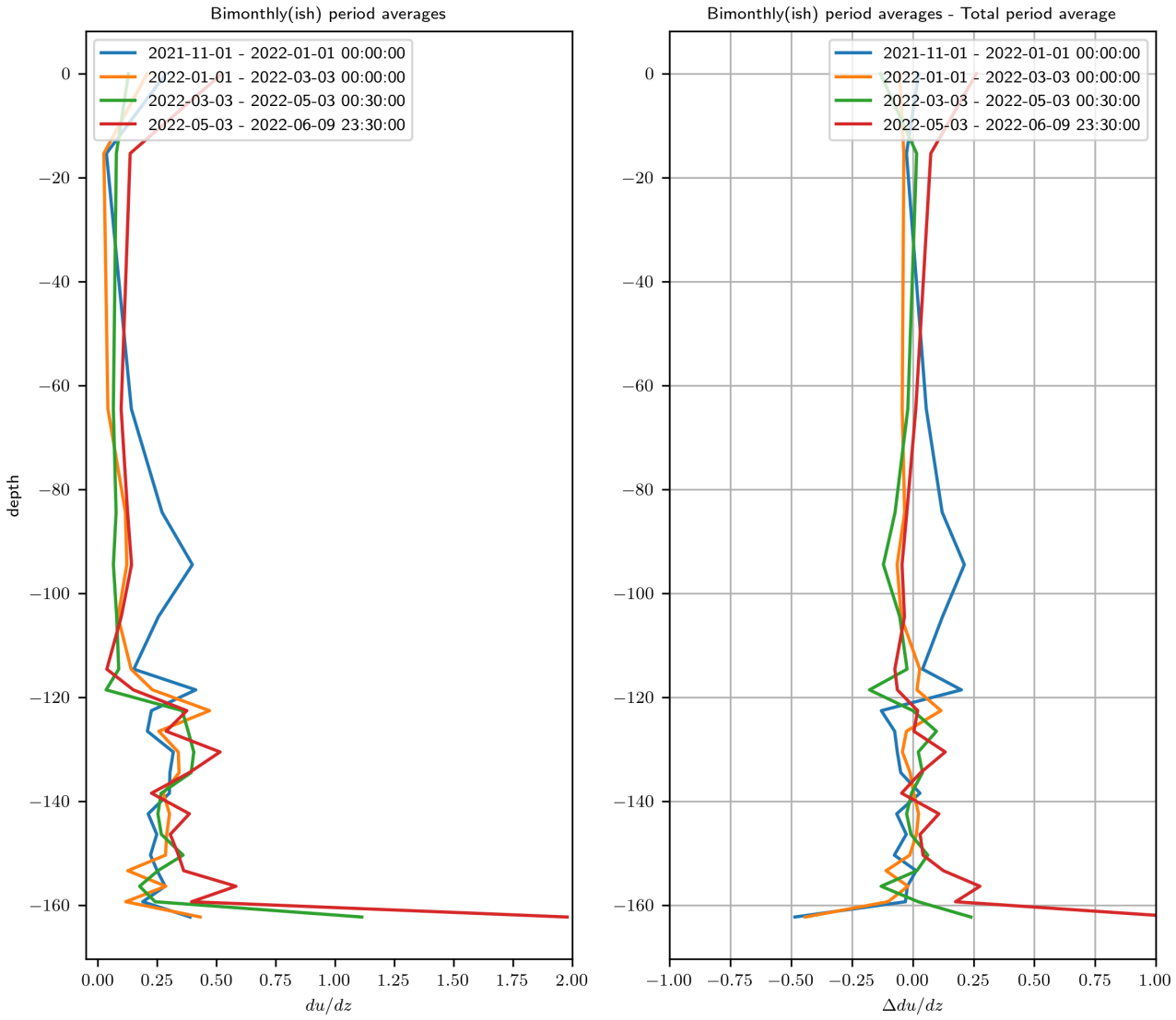

Figure 7.7: Left panel shows the deformation profile at BH14 averaged during different time periods. Right panel shows the difference of the profiles on the left with respect to the deformation averaged between 1st November, 2021 and 9th June, 2022.

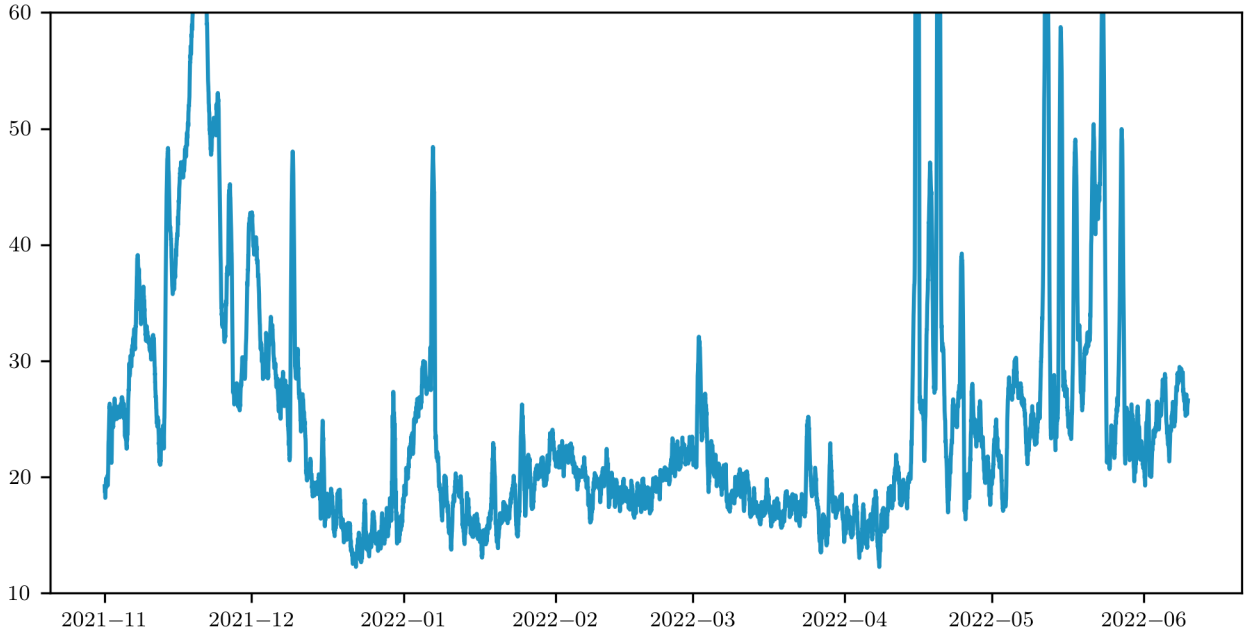

Figure 7.8: Deformation velocity at BH14 including all sensors.

Next, we integrate the deformation data as explained in chapter 5. We show the internal deformation in Figure 7.8. We included all sensors, but the mild seasonality can still be seen whether we include BH14#1 and BH14#2 or not.

7.4 To do

- Have a map of Argentière with the position of the new boreholes
- Include thickness and numerical stress tensor. Once I know the GPS position of the boreholes, of course...
- Compare u_d with all and only from 3 in figure 7.8

Chapter 8

Next steps

Whether you turn to the right or to the left, your ears will hear a voice behind you, saying, 'This is the way; walk in it.'
Isaiah 30:21 *The Old Testament*.

8.1 Overview

Research never stops, as more often than not, answering a scientific question opens the door for a whole lot of new scientific questions that open yet an even bigger set of new scientific questions in a fractal-like dynamic. This PhD does not escape to such behaviour, as I will explain in this chapter. I will present three projects that have been partially resolved, but still remain unfinished. These have been worked by a diverse group of researchers, and my contribution have ranged from almost total to almost bystander. They will be shown in chronological order.

Bibliography

HydrologieSous Glaciaire$_{A}rgentiere_{H}antz_{a}nd_{L}iboutry_{D}ocenFrancais_{1}983.pdf$.

Avant-Après: L'âge sans glace, L'obs, https://www.nouvelobs.com/planete/20190628.OBS3872/avant-apres-regardez-comme-les-glaciers-francais-ont-fondu-en-150-ans.html, accessed: 18/10/2022.

Adams, C. J., Iverson, N. R., Helanow, C., Zoet, L. K., and Bate, C. E.: Softening of Temperate Ice by Interstitial Water, Frontiers in Earth Science, 9, 1–11, doi: 10.3389/feart.2021.702761, 2021.

Allison, E. A.: The spiritual significance of glaciers in an age of climate change, Wiley Interdisciplinary Reviews: Climate Change, 6, 493–508, doi: 10.1002/wcc.354, 2015.

Amundson, J. M., Truffer, M., and Lüthi, M. P.: Time-dependent basal stress conditions beneath Black Rapids Glacier, Alaska, USA, inferred from measurements of ice deformation and surface motion, Journal of Glaciology, 52, 347–357, doi: 10.3189/172756506781828593, 2006.

Arenson, L., Hoelzle, M., and Springman, S.: Borehole deformation measurements and internal structure of some rock glaciers in Switzerland, Permafrost and Periglacial Processes, 13, 117–135, doi: 10.1002/ppp.414, 2002.

Benjumea, B., Macheret, Y. Y., Navarro, F. J., and Teixidó, T.: Estimation of water content in a temperate glacier from radar and seismic sounding data, Annals of Glaciology, 37, 317–324, doi: 10.3189/172756403781815924, 2003.

Bolibar, J., Rabatel, A., Gouttevin, I., Zekollari, H., and Galiez, C.: Nonlinear sensitivity of glacier mass balance to future climate change unveiled by deep learning, Nature Communications, 13, 1–11, doi: 10.1038/s41467-022-28033-0, 2022.

Bouhassira, E.: Clark Glacier Commemorated at Funeral in Oregon, retrieved on 18/10/2022. From Columbia Climate School - GlacierHub Blog, https://news.climate.columbia.edu/2020/10/27/clark-glacier-funeral-oregon/, 2020.

Brondex, J., Gagliardini, O., Gillet-Chaulet, F., and Durand, G.: Sensitivity of grounding line dynamics to the choice of the friction law, Journal of Glaciology, 63, 854–866, doi: 10.1017/jog.2017.51, 2017.

Brondex, J., Gillet-Chaulet, F., and Gagliardini, O.: Sensitivity of centennial mass loss projections of the Amundsen basin to the friction law, Cryosphere, 13, 177–195, doi: 10.5194/tc-13-177-2019, 2019.

Budd, W. and Jacka, T.: A review of ice rheology for ice sheet modelling, Cold Regions Science and Technology, 16, 107–144, doi: 10.1016/0165-232X(89)90014-1, URL https://linkinghub.elsevier.com/retrieve/pii/0165232X89900141, 1989.

Budd, W. F., McInnes, B. J., and Smith, I.: Derivation of Ice Sliding Properties from The Numerical Modelling of Surging Ice Masses, Journal of Glaciology, 23, doi: 10.1017/s0022143000030136, 1979.

Carey, M., Jackson, M., Antonello, A., and Rushing, J.: Glaciers, gender, and science: A feminist glaciology framework for global environmental change research, Progress in Human Geography, 40, 770–793, doi: 10.1177/0309132515623368, 2016.

Chandler, D., Hubbard, B., Hubbard, A., Murray, T., and Rippin, D.: Optimising ice flow law parameters using borehole deformation measurements and numerical modelling, Geophysical Research Letters, 35, 3–7, doi: 10.1029/2008GL033801, 2008.

Chandler, D. M., Wadham, J. L., Nienow, P., Doyle, S. H., Tedstone, A. J., Telling, J., Hawkings, J., Alcock, J. D., Linhoff, B., and Hubbard, A.: Rapid development and persistence of efficient subglacial drainage under 900 m-thick ice in Greenland, Earth and Planetary Science Letters, 566, 116 982, doi: 10.1016/j.epsl.2021.116982, URL https://doi.org/10.1016/j.epsl.2021.116982, 2021.

Chen, G.: GPS kinematic positioning for the airborne laser altimetry at Long Valley, California, Phd, Massachusetts Insitute of Technology, 1999.

Christmann, J., Müller, R., and Humbert, A.: On nonlinear strain theory for a viscoelastic material model and its implications for calving of ice shelves, Journal of Glaciology, 65, 212–224, doi: 10.1017/jog.2018.107, 2019.

Clarke, G. K.: A short history of scientific investigations on glaciers, Journal of Glaciology, 33, 4–24, doi: 10.3189/S0022143000215785, URL https://www.cambridge.org/core/product/identifier/S0022143000215785/type/journal_articlehttp://doi.wiley.com/10.1029/JZ068i015p04513, 1987.

Cohen, D.: Rheology of basal ice at Engabreen, Norway, Ph.D. thesis, 1999.

Cohen, D.: Rheology of ice at the bed of engabreen, Norway, Journal of Glaciology, 46, 611–621, doi: 10.3189/172756500781832620, 2000.

Cohen, D., Iverson, N. R., Hooyer, T. S., Fischer, U. H., Jackson, M., and Moore, P. L.: Debris-bed friction of hard-bedded glaciers, Journal of Geophysical Research: Earth Surface, 110, doi: 10.1029/2004JF000228, 2005.

Compagno, L., Jouvet, G., Bauder, A., Funk, M., Church, G., Leinss, S., and Lüthi, M. P.: Modeling the re-appearance of a crashed airplane on gauligletscher, Switzerland, Frontiers in Earth Science, 7, 1–8, doi: 10.3389/feart.2019.00170, 2019.

Copland, L., Harbor, J., Minner, M., and Sharp, M.: The use of borehole inclinometry in determining basal sliding and internal deformation at Haut Glacier d'Arolla, Switzerland, Annals of Glaciology, 24, 331–337, doi: 10.3189/S0260305500012404, URL https://www.cambridge.org/core/product/identifier/S0260305500012404/type/journal_article, 1997.

Cuffey, K. and Paterson, W.: Physics of Glaciers, June 2006, 2010.

Dahl-Jensen, D. and Gundestrup, N. S.: Constitutive properties of ice at Dye 3, Greenland, International Association of Hydrological Sciences Publication, pp. 31–43, URL http://hydrologie.org/redbooks/a170/iahs_170_0031.pdf, 1987.

d'Emosson SA, E.: Fiche technique prises d'eau d'Argentière, retrieved on 02/11/2022. From https://emosson.ch/amenagements/prises-deau-dargentiere.

Derkacheva, A., Gillet-Chaulet, F., Mouginot, J., Jager, E., Maier, N., and Cook, S.: Seasonal evolution of basal environment conditions of Russell sector, West Greenland, inverted from satellite observation of surface flow, Cryosphere, 15, 5675–5704, doi: 10.5194/tc-15-5675-2021, 2021.

Doyle, S. H., Hubbard, B., Christoffersen, P., Young, T. J., Hofstede, C., Bougamont, M., Box, J. E., and Hubbard, A.: Physical Conditions of Fast Glacier Flow: 1. Measurements From Boreholes Drilled to the Bed of Store Glacier, West Greenland, Journal of Geophysical Research: Earth Surface, 123, 324–348, doi: 10.1002/2017JF004529, 2018.

Duval, P.: The role of the water content on the creep rate of polycrystalline ice, IAHS Publ, 118, 29–33, 1977.

Flusin, G. and Bernard, M.: Forages glaciaires à grande profondeur (Appareil et Méthode de MM . Blumcke et Hess). Rapport de la mission scientifique envoyée en 1906 sur le Hintereisferner (Oetztai), Tech. rep., Études Glaciologiques, tome 1, Tirol autrichien. Massif des Grandes Rousses, 1909.

Forbes, J. D.: Occasional papers on glaciers, Edinburgh Simpkin, pp. https://news.ge/anakliis–porti–aris–qveynis–momava, 1959.

Fowler, A. C.: A Theoretical Treatment of the Sliding of Glaciers in the Absence of Cavitation, 298, 32 117, URL https://doi.org/10.1098/rspa.1986.0090, 1979.

Fowler, A. C.: A sliding law for glaciers of constant viscosity in the presence of subglacial cavitation., Proceedings - Royal Society of London, Series A, 407, 147–170, doi: 10.1098/rspa.1986.0090, 1986.

Fowler, A. C.: Sliding with Cavity Formation, Journal of Glaciology, 33, 255–267, doi: 10.3189/s0022143000008820, 1987.

Fowler, A. C.: Weertman, Lliboutry and the development of sliding theory, Journal of Glaciology, 56, 965–972, doi: 10.3189/002214311796406112, 2011.

Francou, B. and Vincent, C.: Les glaciers à l'epreuve du climat, IRD Éditions, 2010 edn.

Gagliardini, O., Cohen, D., Råback, P., and Zwinger, T.: Finite-element modeling of subglacial cavities and related friction law, Journal of Geophysical Research: Earth Surface, 112, doi: 10.1029/2006JF000576, 2007.

Gagliardini, O., Gillet-Chaulet, F., and Montagnat, M.: A review of anisotropic polar ice models: from crystal to ice-sheet flow models, Low Temperature Science, 68, 149–166, URL http://citeseerx.ist.psu.edu/viewdoc/download?doi=10.1.1.496.2886&rep=rep1&type=pdf, 2009.

Gagliardini, O., Zwinger, T., Gillet-Chaulet, F., Durand, G., Favier, L., de Fleurian, B., Greve, R., Malinen, M., Martín, C., Råback, P., Ruokolainen, J., Sacchettini, M., Schäfer, M., Seddik, H., and Thies, J.: Capabilities and performance of Elmer/Ice, a new-generation ice sheet model, Geoscientific Model Development, 6, 1299–1318, doi: 10.5194/gmd-6-1299-2013, URL https://www.geosci-model-dev.net/6/1299/2013/, 2013.

Gilbert, A., Gimbert, F., Thøgersen, K., Schuler, T. V., and Kääb, A.: Consistent Framework for Coupling Basal Friction with Subglacial Hydrology on Hard-bed Glaciers, Submitted to Geophysical Research Letters, Submitted.

Gillet-Chaulet, F., Hindmarsh, R. C., Corr, H. F., King, E. C., and Jenkins, A.: In-situ quantification of ice rheology and direct measurement of the Raymond Effect at Summit, Greenland using a phase-sensitive radar, Geophysical Research Letters, 38, 1–6, doi: 10.1029/2011GL049843, 2011.

Gimbert, F., Gilbert, A., Gagliardini, O., Vincent, C., and Moreau, L.: Do Existing Theories Explain Seasonal to Multi-Decadal Changes in Glacier Basal Sliding Speed?, Geophysical Research Letters, 48, 1–10, doi: 10.1029/2021GL092858, 2021a.

Gimbert, F., Nanni, U., Roux, P., Helmstetter, A., Garambois, S., Lecointre, A., Walpersdorf, A., Jourdain, B., Langlais, M., Laarman, O., Lindner, F., Sergeant, A., Vincent, C., and Walter, F.: A multi-physics experiment with a temporary dense seismic array on the argentière Glacier, French Alps: The RESOLVE project, Seismological Research Letters, 92, 1185–1201, doi: 10.1785/0220200280, 2021b.

Gimbert, F., Nanni, U., Roux, P., Helmstetter, A., Garambois, S., Lecointre, A., Walpersdorf, A., Jourdain, B., Langlais, M., Laarman, O., Lindner, F., Sergeant, A., Vincent, C., and Walter, F.: A multi-physics experiment with a temporary dense seismic array on the argentière Glacier, French Alps: The RESOLVE project, Seismological Research Letters, 92, 1185–1201, doi: 10.1785/0220200280, 2021c.

Glen, J. W.: The creep of polycrystalline ice, Proceedings of the Royal Society of London. Series A. Mathematical and Physical Sciences, 228, 519–538, doi: 10.1098/rspa.1955.0066, 1955.

Goldberg, D. N., Schoof, C., and Sergienko, O. V.: Stick-slip motion of an Antarctic Ice Stream: The effects of viscoelasticity, Journal of Geophysical Research: Earth Surface, 119, 1564–1580, doi: 10.1002/2014JF003132, 2014.

Gudmundsson, G. H.: Basal-flow characteristics of a non-linear flow sliding frictionless over strongly undulating bedrock, Journal of Glaciology, 43, 80–89, doi: 10.1017/s0022143000002835, 1997a.

Gudmundsson, G. H.: Basal-flow characteristics of a linear medium sliding frictionless over small bedrock undulations, Journal of Glaciology, 43, 71–79, doi: 10.1017/s0022143000002823, 1997b.

Gudmundsson, G. H., Bauder, A., Lüthi, M., Fischer, U. H., and Funk, M.: Estimating rates of basal motion and internal ice deformation from continuous tilt measurements, Annals of Glaciology, 28, 247–252, doi: 10.3189/172756499781821751, 1999.

Hallet, B.: A Theoretical Model of Glacial Abrasion, Journal of Glaciology, 23, 39–50, doi: 10.3189/S0022143000029725, URL https://www.cambridge.org/core/product/identifier/S0022143000029725/type/journal_article, 1979.

Hallet, B.: Glacial Abrasion and Sliding: their Dependence on the Debris Concentration in Basal Ice, Annals of Glaciology, 2, 23–28, doi: 10.3189/172756481794352487, 1981.

Hansen, D. D. and Zoet, L. K.: Experimental constraints on subglacial rock friction, Annals of Glaciology, 60, 37–48, doi: 10.1017/aog.2019.47, 2019.

Hantz, D. and Lliboutry, L.: Waterways, Ice Permeability at Depth, and Water Pressures at Glacier D'Argentière, French Alps, Journal of Glaciology, 29, 227–239, doi: 10.3189/S0022143000008285, 1983.

Harper, J. T., Humphrey, N. F., and Pfeffer, W. T.: Three-dimensional deformation measured in an Alaskan glacier, Science, 281, 1340–1342, doi: 10.1126/science.281.5381.1340, 1998.

Harper, J. T., Humphrey, N. F., Pfeffer, W. T., Huzurbazar, S. V., Bahr, D. B., and Welch, B. C.: Spatial variability in the flow of a valley glacier: Deformation of a large array of boreholes, Journal of Geophysical Research: Solid Earth, 106, 8547–8562, doi: 10.1029/2000jb900440, 2001.

Helanow, C., Iverson, N. R., Zoet, L. K., and Gagliardini, O.: Sliding Relations for Glacier Slip With Cavities Over Three-Dimensional Beds, Geophysical Research Letters, 47, doi: 10.1029/2019GL084924, 2020.

Helanow, C., Iverson, N. R., Woodard, J. B., and Zoet, L. K.: Slip laws for bed-bedded glaciers derived from actual bed topography, Science Advances, pp. 2–10, 2021.

Helmstetter, A., Nicolas, B., Comon, P., and Gay, M.: Basal icequakes recorded beneath an alpine glacier (Glacier d'Argentière, Mont Blanc, France): Evidence for stick-slip motion?, Journal of Geophysical Research: Earth Surface, 120, 379–401, doi: 10.1002/2014JF003288, 2015.

Herman, F., Beyssac, O., Brughelli, M., Lane, S. N., Leprince, S., Adatte, T., Lin, J. Y., Avouac, J. P., and Cox, S. C.: Erosion by an Alpine glacier, Science, 350, doi: 10.1126/science.aab2386, 2015.

Herring, T. A., King, R. W., Floyd, M. A., Mcclusky, S. C., and Sciences, P.: GAMIT Reference manual 10.6, June, Department of Earth, Atmospheric, and Planetary Sciences, Massachusetts Institute of Technology, URL http://geoweb.mit.edu/gg/docs/GAMIT_Ref.pdf, 2018.

Hill, E. A., Hilmar Gudmundsson, G., Rachel Carr, J., and Stokes, C. R.: Velocity response of Petermann Glacier, northwest Greenland, to past and future calving events, Cryosphere, 12, 3907–3921, doi: 10.5194/tc-12-3907-2018, 2018.

Hooke, R. L.: Structure and Flow in the Margin of the Barnes Ice Cap, Baffin Island, N.W.T., Canada, Journal of Glaciology, 12, 423–438, doi: 10.3189/s0022143000031841, 1973.

Hooke, R. L.: Principles of Glacier Mechanics, Cambridge University Press, 2 edn., doi: 10.1017/CBO9780511614231, 2005.

Hooke, R. L., Holmlund, P., and Iverson, N. R.: Extrusion Flow Demonstrated by Bore-Hole Deformation Measurements Over a Riegel, Storglaciären, sweden, Journal of Glaciology, 33, 72–78, doi: 10.3189/S0022143000005372, URL https://www.cambridge.org/core/product/identifier/S0022143000005372/type/journal_article, 1987.

Hooke, R. L., Calla, P., Holmlund, P., Nilsson, M., and Stroeven, A.: A 3 year record of seasonal variations in surface velocity, Storglaciaren, Sweden, Journal of Glaciology, 35, 235–247, doi: 10.3189/s0022143000004561, 1989.

Hooke, R. L., Pohjola, V. A., Jansson, P., and Kohler, J.: Intra-seasonal changes in deformation profiles revealed by borehole studies, Storglaciaren, Sweden, Journal of Glaciology, 38, 348–358, doi: 10.1017/S0022143000002239, 1992.

Hooke, R. L. B. and Hanson, B.: Borehole deformation experiments, Barnes Ice Cap, Canada, Cold Regions Science and Technology, 12, 261–276, doi: 10.1016/0165-232X(86)90039-X, 1986.

Hubbard, B. P., Hubbard, A., Mader, H. M., Tison, J. L., Grust, K., and Nienow, P. W.: Spatial variability in the water content and rheology of temperate glaciers: Glacier de Tsanfleuron, Switzerland, Annals of Glaciology, 37, 1–6, doi: 10.3189/172756403781815474, 2003.

Iken, A.: The Effect of the Subglacial Water Pressure on the Sliding Velocity of a Glacier in an Idealized Numerical Model, Journal of Glaciology, 27, 407–421, doi: 10.3189/S0022143000011448, URL https://www.cambridge.org/core/product/identifier/S0022143000011448/type/journal_article, 1981.

Iken, A. and Bindschadler, R. A.: Combined measurements of Subglacial Water Pressure and Surface Velocity of Findelengletscher, Switzerland: Conclusions about Drainage System and Sliding Mechanism, Journal of Glaciology, 32, 101–119, doi: 10.3189/S0022143000006936, URL https://www.cambridge.org/core/product/identifier/S0022143000006936/type/journal_article, 1986.

Iverson, N. R., Cohen, D., Hooyer, T. S., Fischer, U. H., Jackson, H., Moore, P. L., Lappegard, G., and Kohler, J.: Effects of basal debris on glacier flow, Science, 301, 81–84, doi: 10.1126/science.1083086, 2003.

Iverson, N. R., Helanow, C., and Zoet, L. K.: Debris-bed friction during glacier sliding with ice-bed separation, Annals of Glaciology, 60, 30–36, doi: 10.1017/aog.2019.46, 2019.

Jaquet, S. and l'afp: Des funérailles en montagne pour le Pizol, un glacier suisse disparu, retrieved on 18/10/2022. From RTS, https://www.rts.ch/info/sciences-tech/environnement/10727637-des-funerailles-en-montagne-pour-le-pizol-un-glacier-suisse-disparu.html, 2019.

Joughin, I., Smith, B. E., and Schoof, C. G.: Regularized Coulomb Friction Laws for Ice Sheet Sliding: Application to Pine Island Glacier, Antarctica, Geophysical Research Letters, 46, 4764–4771, doi: 10.1029/2019GL082526, 2019.

Jouvet, G. and Funk, M.: Modelling the trajectory of the corpses of mountaineers who disappeared in 1926 on Aletschgletscher, Switzerland, Journal of Glaciology, 60, 255–261, doi: 10.3189/2014JoG13J156, 2014.

Kääb, A., Leinss, S., Gilbert, A., Bühler, Y., Gascoin, S., Evans, S. G., Bartelt, P., Berthier, E., Brun, F., Chao, W. A., Farinotti, D., Gimbert, F., Guo, W., Huggel, C., Kargel, J. S., Leonard, G. J., Tian, L., Treichler, D., and Yao, T.: Massive collapse of two glaciers in western Tibet in 2016 after surge-like instability, Nature Geoscience, 11, 114–120, doi: 10.1038/s41561-017-0039-7, 2018.

Kamb, B.: Sliding motion of glaciers: Theory and observation, Reviews of Geophysics, 8, 673–728, doi: 10.1029/RG008i004p00673, 1970.

Karlsson, N. B., Colgan, W. T., Binder, D., Machguth, H., Abermann, J., Hansen, K., and Pedersen, A.: Ice-penetrating radar survey of the subsurface debris field at Camp Century, Greenland, Cold Regions Science and Technology, 165, 102 788, doi: 10.1016/j.coldregions.2019.102788, URL https://doi.org/10.1016/j.coldregions.2019.102788, 2019.

Keller, A. and Blatter, H.: Measurement of strain-rate components in a glacier with embedded inclinometers, Journal of Glaciology, 58, 692–698, doi: 10.3189/2012JoG11J234, 2012.

King, M.: Rigorous GPS data-processing strategies for glaciological applications, Journal of Glaciology, 50, 601–607, doi: 10.3189/172756504781829747, 2004.

Larour, E., Seroussi, H., Adhikari, S., Ivins, E., Caron, L., Morlighem, M., and Schlegel, N.: Slowdown in Antarctic mass loss from solid Earth and sea-level feedbacks, Science, 364, doi: 10.1126/science.aav7908, 2019.

Lee, I. R., Hawley, R. L., Bernsen, S., Campbell, S. W., Clemens-Sewall, D., Gerbi, C. C., and Hruby, K.: A novel tilt sensor for studying ice deformation: Application to streaming ice on Jarvis Glacier, Alaska, Journal of Glaciology, 66, 74–82, doi: 10.1017/jog.2019.84, 2019.

Lipovsky, B. P., Meyer, C. R., Zoet, L. K., McCarthy, C., Hansen, D. D., Rempel, A. W., and Gimbert, F.: Glacier sliding, seismicity and sediment entrainment, Annals of Glaciology, 60, 182–192, doi: 10.1017/aog.2019.24, 2019.

Lliboutry, L.: Contribution à la théorie du frottement du glacier sur son lit., C. R. Hebd. Se´ances Acad. Sci., 247, 318–320, 1958.

Lliboutry, L.: General Theory of Subglacial Cavitation and Sliding of Temperate Glaciers, Journal of Glaciology, 7, 21–58, doi: 10.3189/S0022143000020396, URL https://www.cambridge.org/core/product/identifier/S0022143000020396/type/journal_article, 1968.

Lliboutry, L.: The Dynamics of Temperate Glaciers from the Detailed Viewpoint, Journal of Glaciology, 8, 185–205, doi: 10.3189/S002214300003118X, URL https://www.cambridge.org/core/product/identifier/S002214300003118X/type/journal_article, 1969.

Lliboutry, L.: Permeability, Brine Content and Temperature of Temperate Ice, Journal of Glaciology, 10, 15–29, doi: 10.3189/s002214300001296x, 1971.

Lliboutry, L. and Duval, P.: Various isotropic and anisotropic ices found in glaciers and polar ice caps and their corresponding rheologies, International Journal of Rock Mechanics and Mining Sciences Geomechanics Abstracts, 22, 198, doi: 10.1016/0148-9062(85)90267-0, URL https://linkinghub.elsevier.com/retrieve/pii/0148906285902670, 1985.

Luckhurst, T.: Iceland's Okjokull glacier commemorated with plaque, retrieved on 18/10/2022. From BBC, https://www.bbc.com/news/world-europe-49345912, 2019.

Lüthi, M., Funk, M., Iken, A., Gogineni, S., and Truffer, M.: Mechanisms of fast flow in Jakobshavn Isbræ, West Greenland: Part III. Measurements of ice deformation, temperature and cross-borehole conductivity in boreholes to the bedrock, Journal of Glaciology, 48, 369–385, doi: 10.3189/172756502781831322, 2002.

MacAyeal, D. R., Sergienko, O. V., and Banwell, A. F.: A model of viscoelastic ice-shelf flexure, Journal of Glaciology, 61, 635–645, doi: 10.3189/2015JoG14J169, 2015.

Maier, N., Humphrey, N., Harper, J., and Meierbachtol, T.: Sliding dominates slow-flowing margin regions, Greenland Ice Sheet, Science Advances, 5, eaaw5406, doi: 10.1126/sciadv.aaw5406, URL https://advances.sciencemag.org/lookup/doi/10.1126/sciadv.aaw5406, 2019.

Maier, N., Humphrey, N., Meierbachtol, T., and Harper, J.: Deformation motion tracks sliding changes through summer, western Greenland, Journal of Glaciology, pp. 1–10, doi: 10.1017/jog.2021.87, URL https://www.cambridge.org/core/product/identifier/S0022143021000873/type/journal_article, 2021.

Maier, N., Gimbert, F., and Gillet-Chaulet, F.: Threshold response to melt drives large-scale bed weakening in Greenland, Nature, 607, 714–720, doi: 10.1038/s41586-022-04927-3, URL https://www.nature.com/articles/s41586-022-04927-3, 2022.

Marshall, H. P., Harper, J. T., Pfeffer, W. T., and Humphrey, N. F.: Depth-varying constitutive properties observed in an isothermal glacier, Geophysical Research Letters, 29, 2–5, doi: 10.1029/2002GL015412, 2002.

Mathews, W. H.: Vertical Distribution of Velocity in Salmon Glacier, British Columbia, Journal of Glaciology, 3, 448–454, doi: 10.3189/S0022143000017184, URL https://www.cambridge.org/core/product/identifier/S0022143000017184/type/journal_article, 1959.

McCarthy, C., Savage, H., and Nettles, M.: Temperature dependence of ice-on-rock friction at realistic glacier conditions, Philosophical Transactions of the Royal Society A: Mathematical, Physical and Engineering Sciences, 375, doi: 10.1098/rsta.2015.0348, 2017.

McConnell, J. R., Wilson, A. I., Stohl, A., Arienzo, M. M., Chellman, N. J., Eckhardt, S., Thompson, E. M., Pollard, A. M., and Steffensen, J. P.: Lead pollution recorded in Greenland ice indicates European emissions tracked plagues, wars, and imperial expansion during antiquity, Proceedings of the National Academy of Sciences of the United States of America, 115, 5726–5731, doi: 10.1073/pnas.1721818115, 2018.

Millan, R., Mouginot, J., Rabatel, A., and Morlighem, M.: Ice velocity and thickness of the world's glaciers, Nature Geoscience, 15, 124–129, doi: 10.1038/s41561-021-00885-z, URL https://www.nature.com/articles/s41561-021-00885-z, 2022.

Miller, M.: Phenomena associated with the deformation of a glacier bore-hole, Extrait Des Comptes Rendus Et Rapports- Assemblée Générale de Toronto, URL http://ks360352.kimsufi.com/redbooks/a046/04641.pdf, 1957.

Millstein, J. D., Minchew, B. M., and Pegler, S. S.: Ice viscosity is more sensitive to stress than commonly assumed, Communications Earth Environment, 3, 1–7, doi: 10.1038/s43247-022-00385-x, 2022.

Morland, L. W.: Glacier Sliding Down an Inclined Wavy Bed, Journal of Glaciology, 17, 447–462, doi: 10.1017/S0022143000013733, URL https://www.cambridge.org/core/product/identifier/S0022143000013733/type/journal_article, 1976a.

Morland, L. W.: Glacier Sliding Down an Inclined Wavy Bed With Friction, Journal of Glaciology, 17, 463–477, doi: 10.3189/S0022143000013745, URL https://www.cambridge.org/core/product/identifier/S0022143000013745/type/journal_article, 1976b.

Morlighem, M., Seroussi, H., Larour, E., and Rignot, E.: Inversion of basal friction in Antarctica using exact and incomplete adjoints of a higher-order model, Journal of Geophysical Research: Earth Surface, 118, 1746–1753, doi: 10.1002/jgrf.20125, 2013.

Murray, T., Stuart, G. W., Fry, M., Gamble, N. H., and Crabtree, M. D.: Englacial water distribution in a temperate glacier from surface and borehole radar velocity analysis, Journal of Glaciology, 46, 389–398, doi: 10.3189/172756500781833188, 2000.

Murray, T., Booth, A., and Rippin, D. M.: Water-content of Glacier-ice: Limitations on estimates from velocity analysis of surface ground-penetrating radar surveys, Journal of Environmental and Engineering Geophysics, 12, 87–99, doi: 10.2113/JEEG12.1.87, 2007.

Nanni, U.: Resolving subglacial hydrology network dynamics through seismic observations on an Alpine glacier, Ph.D. thesis, Université Grenoble Alpes, 2020b.

Nanni, U., Gimbert, F., Vincent, C., Gräff, D., Walter, F., Piard, L., and Moreau, L.: Quantification of seasonal and diurnal dynamics of subglacial channels using seismic observations on an Alpine glacier, Cryosphere, 14, 1475–1496, doi: 10.5194/tc-14-1475-2020, 2020a.

Nanni, U., Gimbert, F., Roux, P., and Lecointre, A.: Observing the subglacial hydrology network and its dynamics with a dense seismic array, Proceedings of the National Academy of Sciences of the United States of America, 118, 1–7, doi: 10.1073/pnas.2023757118, 2021.

Nye, J. F.: The flow law of ice from measurements in glacier tunnels, laboratory experiments and the Jungfraufirn borehole experiment, Proceedings of the Royal Society of London. Series A. Mathematical and Physical Sciences, 219, 477–489, doi: 10.1098/rspa.1953.0161, URL https://royalsocietypublishing.org/doi/10.1098/rspa.1953.0161, 1953.

Nye, J. F.: The Flow of a Glacier in a Channel of Rectangular, Elliptic or Parabolic Cross-Section, Journal of Glaciology, 5, 661–690, doi: 10.3189/s0022143000018670, 1965.

Nye, J. F.: A calculation on the sliding of ice over a wavy surface using a N ew tonian viscous approxim ation, Proc. Roy. Soc. A, 1969.

Oppenheimer, M., B. G. J. H. R. v. d. W. A. M. A. A.-E. R. C. M. C.-J. R. D. T. G. J. H. F. I. B. M. B. M. and Sebesvari, Z.: Sea Level Rise and Implications for Low-Lying Islands, Coasts and Communities. In: IPCC Special Report on the

Ocean and Cryosphere in a Changing Climate, IPCC Special Report on the Ocean and Cryosphere in a Changing Climate, pp. 321–445, doi: 10.1017/9781009157964.006., 2019.

Paterson, W. S. B.: The Sliding Velocity of Athabasca Glacier, Canada, Journal of Glaciology, 9, 55–63, doi: 10.3189/S0022143000026794, URL https://www.cambridge.org/core/product/identifier/S0022143000026794/type/journal_article, 1970.

Paterson, W. S. B.: The physics of glaciers, Pergamon Oxford, OX, England ; Tarrytown, N.Y., U.S.A, 3rd ed. edn., 1994.

Pattyn, F.: Antarctic subglacial conditions inferred from a hybrid ice sheet/ice stream model, Earth and Planetary Science Letters, 295, 451–461, doi: 10.1016/j.epsl.2010.04.025, 2010.

Pattyn, F. and Morlighem, M.: The uncertain future of the Antarctic Ice Sheet, Science, 367, 1331–1335, doi: 10.1126/science.aaz5487, URL https://science.sciencemag.org/content/367/6484/1331, 2020.

Perutz, M. F.: Report on Problems Relating to the Flow of Glaciers, Journal of Glaciology, 1, 47–51, doi: 10.3189/s0022143000007541, 1947.

Perutz, M. F.: Direct Measurement of the Velocity Distribution in a Vertical Profile Through a Glacier, Journal of Glaciology, 1, 382–383, doi: 10.3189/s0022143000012594, 1949.

Perutz, M. F.: Direct Measurement of the Velocity Distribution in a Vertical Profile Through a Glacier, Journal of Glaciology, 1, 382–383, doi: 10.3189/S0022143000012594, URL https://www.cambridge.org/core/product/identifier/S0022143000012594/type/journal_article, 1950.

Pettersson, R., Jansson, P., and Blatter, H.: Spatial variability in water content at the cold-temperate transition surface of the polythermal Storglaciären, Sweden, Journal of Geophysical Research: Earth Surface, 109, n/a–n/a, doi: 10.1029/2003jf000110, 2004.

Preunkert, S., McConnell, J. R., Hoffmann, H., Legrand, M., Wilson, A. I., Eckhardt, S., Stohl, A., Chellman, N. J., Arienzo, M. M., and Friedrich, R.: Lead and Antimony in Basal Ice From Col du Dome (French Alps) Dated With Radiocarbon: A Record of Pollution During Antiquity, Geophysical Research Letters, 46, 4953–4961, doi: 10.1029/2019GL082641, 2019.

Rabatel, A. and Biron, R.: SmartStake: an autonomous measurement station for high resolution glacier ablation monitoring, retrieved on 09/11/2022. From https://a2photonicsensors.com/smartstake-monitor-glacier-ablation/.

Rada, C. and Schoof, C.: Channelized, distributed, and disconnected: Subglacial drainage under a valley glacier in the Yukon Subglacial drainage controls on basal sliding View project Channelized, distributed, and disconnected: subglacial drainage under a valley glacier in the Yu, The Cryosphere, 12, 2609–2636, doi: 10.5194/tc-12-2609-2018, URL https://doi.org/10.5194/tc-12-2609-2018, 2018.

Raymond, C.: Flow in a Transverse Section of Athabasca Glacier, Alberta, Canada, Journal of Glaciology, 10, 55–84, doi: 10.3189/s0022143000012995, 1971.

Raymond, C. F. and Harrison, W. D.: Some Observations on the Behavior of the Liquid and Gas Phases in Temperate Glacier Ice, Journal of Glaciology, 14, 213–233, doi: 10.3189/s0022143000021717, 1975.

Rémy, F. and Testut, L.: Mais comment s'écoule donc un glacier ? Aperçu historique, Comptes Rendus - Geoscience, 338, 368–385, doi: 10.1016/j.crte.2006.02.004, 2006.

Ritz, C., Edwards, T. L., Durand, G., Payne, A. J., Peyaud, V., and Hindmarsh, R. C.: Potential sea-level rise from Antarctic ice-sheet instability constrained by observations, Nature, 528, 115–118, doi: 10.1038/nature16147, URL http://dx.doi.org/10.1038/nature16147, 2015.

Roeoesli, C., Helmstetter, A., Walter, F., and Kissling, E.: Meltwater influences on deep stick-slip icequakes near the base of the Greenland Ice Sheet, Journal of Geophysical Research: Earth Surface, 121, 223–240, doi: 10.1002/2015JF003601, 2016.

Roldan-Blasco, J. P., Piard, L., Gilbert, A., F., G., et al.: deformation paper.

Röthlisberger, H.: Water Pressure in Intra- and Subglacial Channels, Journal of Glaciology, 11, 177–203, doi: 10.3189/s0022143000022188, 1972.

Ryser, C., Lüthi, M. P., Andrews, L. C., Hoffman, M. J., Catania, G. A., Hawley, R. L., Neumann, T. A., and Kristensen, S. S.: Sustained high basal motion of the Greenland ice sheet revealed by borehole deformation, Journal of Glaciology, 60, 647–660, doi: 10.3189/2014JoG13J196, URL https://www.cambridge.org/core/product/identifier/S0022143000203018/type/journal_article, 2014.

Schaer, J.-P.: Le rôle d 'Agassiz en glaciologie ou la réussite d 'un entrepreneur scientifique ambitieux, Comité Français d'Histoire de la Géologie - Troisième série, 2001.

Schaffrin, B. and Bock, Y.: A unified scheme for processing GPS dual-band phase observations, Bulletin Géodésique, 62, 142–160, doi: 10.1007/BF02519222, 1988.

Schoof, C.: The effect of cavitation on glacier sliding, Proceedings of the Royal Society A: Mathematical, Physical and Engineering Sciences, 461, 609–627, doi: 10.1098/rspa.2004.1350, 2005.

Schulson, E. M. and Duval, P.: Creep and fracture of ice, doi: 10.1017/CBO9780511581397, 2009.

Schweizer, J. and Iken, A.: The role of bed separation and friction in sliding over an undeformable bed, Journal of Glaciology, 38, 77–92, doi: 10.1017/S0022143000009618, 1992.

Seligman, R.: Joint Meeting of the British Glaciological Society, the British Rheologists' Club and the Institute of Metals, Journal of Glaciology, 1, 231–240, doi: 10.3189/002214349793702827, URL https://www.cambridge.org/core/product/identifier/S0022143000009795/type/journal_article, 1949.

Sergeant, A., Chmiel, M., Lindner, F., Walter, F., Roux, P., Chaput, J., Gimbert, F., and Mordret, A.: On the Green's function emergence from interferometry of seismic wave fields generated in high-melt glaciers: Implications for passive imaging and monitoring, Cryosphere, 14, 1139–1171, doi: 10.5194/tc-14-1139-2020, 2020.

Sharp, R. P.: Deformation of a Vertical Bore Hole in a Piedmont Glacier, Journal of Glaciology, 2, 182–184, doi: 10.3189/S0022143000025685, URL https://www.cambridge.org/core/product/identifier/S0022143000025685/type/journal_article, 1953.

Shreve, R. and Sharp, R.: Internal Deformation and Thermal Anomalies in Lower Blue Glacier, Mount Olympus, Washington, U.S.A., Journal of Glaciology, 9, 65–86, doi: 10.3189/S0022143000026800, URL https://www.cambridge.org/core/product/identifier/S0022143000026800/type/journal_article, 1970.

Solomina, O. N., Bradley, R. S., Jomelli, V., Geirsdottir, A., Kaufman, D. S., Koch, J., McKay, N. P., Masiokas, M., Miller, G., Nesje, A., Nicolussi, K., Owen, L. A., Putnam, A. E., Wanner, H., Wiles, G., and Yang, B.: Glacier fluctuations during the past 2000 years, Quaternary Science Reviews, 149, 61–90, doi: 10.1016/j.quascirev.2016.04.008, 2016.

Thøgersen, K., Gilbert, A., Schuler, T. V., and Malthe-Sørenssen, A.: Rate-and-state friction explains glacier surge propagation, Nature Communications, 10, 1–8, doi: 10.1038/s41467-019-10506-4, URL http://dx.doi.org/10.1038/s41467-019-10506-4, 2019.

Thompson, A. C., Iverson, N. R., and Zoet, L. K.: Controls on Subglacial Rock Friction: Experiments With Debris in Temperate Ice, Journal of Geophysical Research: Earth Surface, 125, 1–18, doi: 10.1029/2020JF005718, 2020.

Thorsteinsson, T.: An analytical approach to deformation of anisotropic ice-crystal aggregates, Journal of Glaciology, 47, 507–516, doi: 10.3189/172756501781832124, 2001.

Togaibekov, A., Walpersdorf, A., and Gimbert, F.: Short-term surface velocity variations of the Argentière glacier monitored with a high-resolution continuous GNSS network, i, 5194, 2022.

Tsai, V. C., Smith, L. C., Gardner, A. S., and Seroussi, H.: A unified model for transient subglacial water pressure and basal sliding, Journal of Glaciology, pp. 1–11, doi: 10.1017/jog.2021.103, 2021.

Turrel, M.: Louis Lliboutry, le champollion des glaces, 2017.

Vallon, M., Petit, J.-R., and Fabre, B.: Study of an Ice Core to the Bedrock in the Accumulation zone of an Alpine Glacier, Journal of Glaciology, 17, 13–28, doi: 10.3189/s0022143000030677, 1976.

Vincent, C.: Influence of climate change over the 20th Century on four French glacier mass balances, Journal of Geophysical Research Atmospheres, 107, ACL 4–1–ACL 4–12, doi: 10.1029/2001JD000832, 2002.

Vincent, C. and Moreau, L.: Sliding velocity fluctuations and subglacial hydrology over the last two decades on Argentière glacier, Mont Blanc area, Journal of Glaciology, 62, 805–815, doi: 10.1017/jog.2016.35, 2016.

Vincent, C., Soruco, A., Six, D., and Meur, E. L.: Glacier thickening and decay analysis from 50 years of glaciological observations performed on Glacier d'Argentière, Mont Blanc area, France, Annals of Glaciology, 50, 73–79, doi: 10.3189/172756409787769500, 2009.

Vincent, C., Garambois, S., Thibert, E., Lefèbvre, E., Le Meur, E., and Six, D.: Origin of the outburst flood from Glacier de Tête Rousse in 1892 (Mont Blanc area, France), Journal of Glaciology, 56, 688–698, doi: 10.3189/002214310793146188, 2010.

Vincent, C., Gilbert, A., and Walpersdorf, A.: Evidence of seasonal uplift in the Argentière glacier (Mont Blanc area, France), 2022a.

Vincent, C., Gilbert, A., and Walpersdorf, A.: Supporting Information for Evidence of seasonal uplift in the Argentière glacier (Mont Blanc area, France), 2022b.

Vivian, R. and Bocquet, G.: Subglacial Cavitation Phenomena Under the Glacier D'Argentière, Mont Blanc, France, Journal of Glaciology, 12, 439–451, doi: 10.3189/S0022143000031853, URL https://www.cambridge.org/core/product/identifier/S0022143000031853/type/journal_article, 1973.

Weertman, J.: On the Sliding of Glaciers, Journal of Glaciology, doi: 10.3189/s0022143000024709, 1957.

Weertman, J.: The Theory of Glacier Sliding, Journal of Glaciology, 5, 287–303, doi: 10.3189/s0022143000029038, 1964.

Weertman, J.: General theory of water flow at the base of a glacier or ice sheet, Reviews of Geophysics, 10, 287–333, doi: 10.1029/RG010i001p00287, 1972.

Werder, M. A., Hewitt, I. J., Schoof, C. G., and Flowers, G. E.: Modeling channelized and distributed subglacial drainage in two dimensions, Journal of Geophysical Research: Earth Surface, 118, 2140–2158, doi: 10.1002/jgrf.20146, 2013.

WGMS: Fluctuations of Glaciers Database, Zurich, Switzerland, data retrieved from World Glacier Monitoring Service (WGMS), https://doi.org/10.5904/wgms-fog-2022-09, 2022.

Wiens, D. A., Anandakrishnan, S., Winberry, J. P., and King, M. A.: Simultaneous teleseismic and geodetic observations of the stick-slip motion of an Antarctic ice stream, Nature, 453, 770–774, doi: 10.1038/nature06990, 2008.

Willis, I., Mair, D., Hubbard, B., Nienow, P., Fischer, U. H., and Hubbard, A.: Seasonal variations in ice deformation and basal motion across the tongue of Haut Glacier d'Arolla, Switzerland, Annals of Glaciology, 36, 157–167, doi: 10.3189/172756403781816455, 2003.

Zekollari, H., Huss, M., and Farinotti, D.: Modelling the future evolution of glaciers in the European Alps under the EURO-CORDEX RCM ensemble, Cryosphere, doi: 10.5194/tc-13-1125-2019, 2019.

Zoet, L. K. and Iverson, N. R.: Experimental determination of a double-valued drag relationship for glacier sliding, Journal of Glaciology, 61, 1–7, doi: 10.3189/2015JoG14J174, URL https://www.cambridge.org/core/product/identifier/S0022143000203535/type/journal_article, 2015.

Zoet, L. K., Anandakrishnan, S., Alley, R. B., Nyblade, A. A., and Wiens, D. A.: Motion of an Antarctic glacier by repeated tidally modulated earthquakes, Nature Geoscience, 5, 623–626, doi: 10.1038/ngeo1555, 2012.

Zoet, L. K., Carpenter, B., Scuderi, M., Alley, R. B., Anandakrishnan, S., Marone, C., and Jackson, M.: The effects of entrained debris on the basal sliding stability of a glacier, Journal of Geophysical Research: Earth Surface, 118, 656–666, doi: 10.1002/jgrf.20052, 2013.

Zryd, A.: Conditions dans la couche basale des glaciers tempérés: contraintes, teneur en eau et frottement intérieur, Ph.D. thesis, 1991.